

# KINETICS ASSISTED DESIGN OF CATALYSTS FOR COAL LIQUEFACTION

DE-AC22-90PC90050

## Final Report

to the

U. S. Department of Energy

by

Michael T. Klein, Henry C. Foley, William H. Calkins, and Charles  
Scouten

Center for Catalytic Science and Technology  
Department of Chemical Engineering  
University of Delaware  
Newark, Delaware 19716

DISTRIBUTION OF THIS DOCUMENT IS UNLIMITED

# MASTER

### DISCLAIMER

This report was prepared as an account of work sponsored by an agency of the United States Government. Neither the United States Government nor any agency thereof, nor any of their employees, makes any warranty, express or implied, or assumes any legal liability or responsibility for the accuracy, completeness, or usefulness of any information, apparatus, product, or process disclosed, or represents that its use would not infringe privately owned rights. Reference herein to any specific commercial product, process, or service by trade name, trademark, manufacturer, or otherwise does not necessarily constitute or imply its endorsement, recommendation, or favoring by the United States Government or any agency thereof. The views and opinions of authors expressed herein do not necessarily state or reflect those of the United States Government or any agency thereof.

RECEIVED  
UCDOE/PETC  
35 DEC 11 AM 9:49  
MINISTRY OF ASSISTANCE NW

## **DISCLAIMER**

**Portions of this document may be illegible  
electronic image products. Images are  
produced from the best available original  
document.**

# **KINETICS ASSISTED DESIGN OF CATALYSTS FOR COAL LIQUEFACTION**

*DE-AC 22-90PC90050*

## **Final Report**

to the

**U. S. Department of Energy**

by

**Michael T. Klein, Henry C. Foley, William H. Calkins, and Charles  
Scouten**

**Center for Catalytic Science and Technology  
Department of Chemical Engineering  
University of Delaware  
Newark, Delaware 19716**

**CLEARED BY  
PATENT COUNSEL**

RECEIVED  
64-16 NOV 11 0300  
U.S. DEPARTMENT OF ENERGY  
WASHINGTON, D.C.

## TABLE OF CONTENTS

LIST OF TABLES .....	ix
LIST OF FIGURES .....	xii
ABSTRACT.....	xviii

### Chapter

1	INTRODUCTION.....	1
1.1	Direct Coal Liquefaction .....	1
1.2	Coal Liquefaction Catalysis.....	2
1.2.1	Supported Acid Catalysts.....	2
1.2.2	Superacid Catalysts.....	3
1.2.3	Unsupported Metal Catalysts .....	4
1.3	Model Compounds .....	7
1.4	Linear Free Energy Relationships (LFERs).....	9
1.5	Catalyst Design .....	10
1.5.1	Kinetics-Assisted Design of Catalysts.....	11
1.5.2	Model Compound Selection.....	20
1.6	Summary.....	21
	REFERENCES.....	22
2	PYROLYSIS OF 4-(1-NAPHTHYLMETHYL)BIBENZYL .....	28
2.1	Pyrolysis of 4-(Naphthylmethyl)bibenzyl.....	29
2.1.1	Experimental Method - NBBM Reactions .....	30
2.1.2	NBBM Pyrolysis Results .....	31
2.2	Thermal Background for Catalysis.....	40
2.3	Long Reaction Time NBBM Pyrolysis Data.....	42
2.4	Summary of NBBM Pyrolysis Results .....	46
	REFERENCES.....	48



3	A MECHANISTIC MODEL PROBING REACTION KINETICS AND PATHWAYS OF 4-(1-NAPHTHYLMETHYL)BIBENZYL.....	49
3.1	Guiding Experimental Results.....	53
3.1.1	Algorithm for Determining Model Reactions.....	56
3.1.2	Estimation of Rate Constants.....	61
3.2	Parameter Optimization.....	65
3.3	Mechanistic Modeling Results.....	66
3.4	Summary and Conclusions.....	77
	REFERENCES.....	79
4	MODEL COMPOUND REACTIONS OVER SOLID CATALYSTS.....	81
4.1	Experimental Plan.....	82
4.1.1	Experimental Methods.....	83
4.2	Reaction Results.....	85
4.2.1	NBBM Reaction in the Presence of $\text{Fe}(\text{CO})_3(\text{PPh}_3)_2$ at 420 °C under a Hydrogen or Nitrogen Atmosphere.....	88
4.2.2	NBBM Reaction in the Presence of $\text{Fe}(\text{CO})_4\text{PPh}_3$ , $\text{Fe}(\text{CO})_3(\text{PPh}_3)_2$ , and $\text{Fe}(\text{CO})_2(\text{PPh}_3)_2\text{CS}_2$ at 400 °C under a Hydrogen Atmosphere.....	92
4.2.3	NBBM Reaction in the Presence of $\text{Fe}(\text{CO})_5$ , $\text{Mo}(\text{CO})_6$ , $\text{Mn}_2(\text{CO})_{10}$ , $\text{Fe}_2\text{O}_3$ , and $\text{MoS}_2$ at 400 °C under a Hydrogen Atmosphere.....	99
4.3	Summary and Conclusions.....	105
	REFERENCES.....	107

5	MODELING OF THE CATALYTIC CHEMISTRY OF 4-(1-NAPHTHYLMETHYL)BIBENZYL .....	109
5.1	Guiding Experimental Results .....	111
5.1.1	Algorithm for Determining Model Reactions.....	114
5.2	Model Description.....	116
5.2.1	Estimation of Rate Constants .....	119
5.2.1.1	A Computational Quantum Chemical Method for Estimating Energetics of Transition Metal Species ...	121
5.2.1.2	Analysis of Metal Clusters .....	123
5.2.1.3	LFERs for Catalytic Reaction Families.....	129
5.3	Parameter Estimation .....	131
5.4	Mechanistic Modeling Results.....	135
5.5	Kinetics-Assisted Design of Catalysts .....	140
5.6	Summary and Conclusions .....	143
	REFERENCES.....	146
6	SUMMARY AND CONCLUSIONS.....	149
6.1	Summary.....	149
6.1.1	Pyrolysis of NBBM .....	150
6.1.2	Mechanistic Modeling of NBBM .....	151
6.1.3	Catalytic Reaction of NBBM .....	151
6.1.4	Mechanistic Modeling of NBBM Catalysis.....	153
6.2	Conclusions.....	154
	APPENDIX A: REACTIONS FOR THE MECHANISTIC MODEL DESCRIBING NBBM HYDROLYSIS.....	158
	APPENDIX B: EXPERIMENTAL DATA FOR NBBM REACTIONS .....	187

## LIST OF TABLES

Table 2.1	Summary of reaction products from NBBM hydrolysis at 420 °C...	34
Table 3.1	Summary of reaction products from NBBM hydrolysis at 420 °C...	54
Table 3.2	Reaction matrices used in constructing the NBBM mechanistic kinetics model. ....	57
Table 3.3	Reaction rules used in conjunction with the reaction matrices of Table 3.2 for constructing the NBBM mechanistic kinetics model. ....	58
Table 3.4	Energetics for benzyl and H• radical ipso substitution into naphthyl and phenyl rings. ....	60
Table 3.5	Summary of reaction families used to predict rate constants.....	64
Table 3.6	Observed products from NBBM hydrolysis at 420°C under 1000 psig hydrogen (cold). ....	69
Table 3.7	Optimal parameters for the mechanistic model describing NBBM hydrolysis at 420 °C.....	70
Table 4.1	Summary of experimental plan for reaction of NBBM with solid catalytic materials. ....	83
Table 4.2	Summary of reactant loadings for catalytic reactions of NBBM. ....	85
Table 4.3	Summary of the major reaction products from NBBM catalysis under hydrogen.....	86
Table 4.4	Regressed values for the first-order rate constants for the reaction network of Figure 4.2.....	96
Table 4.5	Regressed values for the first-order rate constants for the reaction network of Figure 4.2.....	104

Table 5.1	Summary of the major reaction products from NBBM catalysis under hydrogen.....	113
Table 5.2	Reaction matrices for the elementary step reaction families used in constructing the NBBM mechanistic kinetics model.....	115
Table 5.3	Catalytic reactions included in the mechanistic kinetics model. M- signifies surface bound species.....	117
Table 5.4	Summary of reaction families used to predict rate constants.....	120
Table 5.5	Atomic orbital parameters used for ASED-MO calculations. ....	122
Table 5.6	Structural parameters for the metal clusters modeled with the ASED-MO method. ....	124
Table 5.7	Summary of reaction families used to predict rate constants.....	128
Table 5.8	Adsorption energies for hydrogen and naphthalene on the (001) surface of catalytic metal clusters.....	129
Table 5.9	Optimal parameters for the mechanistic model describing NBBM catalysis at 400 °C with $\text{Fe}(\text{CO})_5$ , $\text{Mo}(\text{CO})_6$ , $\text{Mn}_2(\text{CO})_{10}$ , $\text{Fe}_2\text{O}_3$ and $\text{MoS}_2$ .....	132
Table 5.10	ASED-MO predicted naphthalene adsorption enthalpies for several materials commonly used as catalysts.....	143
Table A.1	Reaction listing for the mechanistic model describing NBBM thermal chemistry.....	159

Table B.1	Product Codes for the NBBM reactions' observed product spectra.....	188
Table B.2	NBBM pyrolysis results at 420 °C under a nitrogen atmosphere.....	189
Table B.3	NBBM pyrolysis results at 420 °C under a hydrogen atmosphere. ....	190
Table B.4	NBBM pyrolysis results at 420 °C under a hydrogen atmosphere.....	191
Table B.5	NBBM pyrolysis results at 400 °C under a hydrogen atmosphere.....	192
Table B.6	NBBM catalysis results at 420 °C with $\text{Fe}(\text{CO})_3(\text{PPh}_3)_2$ under a nitrogen atmosphere. ....	193
Table B.7	NBBM catalysis results at 420 °C with $\text{Fe}(\text{CO})_3(\text{PPh}_3)_2$ under a hydrogen atmosphere.....	194
Table B.8	NBBM catalysis results at 400 °C with $\text{Fe}(\text{CO})_4\text{PPh}_3$ under a hydrogen atmosphere.....	195
Table B.9	NBBM catalysis results at 400 °C with $\text{Fe}(\text{CO})_3(\text{PPh}_3)_2$ under a hydrogen atmosphere.....	196
Table B.10	NBBM catalysis results at 400 °C with $\text{Fe}(\text{CO})_2(\text{PPh}_3)_2\text{CS}_2$ under a hydrogen atmosphere.....	197
Table B.11	NBBM catalysis results at 400 °C with $\text{Fe}(\text{CO})_5$ under a hydrogen atmosphere. ....	198
Table B.12	NBBM catalysis results at 400 °C with $\text{Mo}(\text{CO})_6$ under a hydrogen atmosphere. ....	199
Table B.13	NBBM catalysis results at 400 °C with $\text{Mn}_2(\text{CO})_{10}$ under a hydrogen atmosphere. ....	200
Table B.14	NBBM catalysis results at 400 °C with $\text{Fe}_2\text{O}_3$ under a hydrogen atmosphere. ....	201
Table B.15	NBBM catalysis results at 400 °C with $\text{MoS}_2$ under a hydrogen atmosphere. ....	202

## LIST OF FIGURES

Figure 1.1	Coal liquefaction reaction families: (1) bond homolysis, (2) hydrogen abstraction, (3) $\beta$ -scission, (4) radical-induced hydrogen transfer, (5) radical recombination, and (6) radical disproportionation. ....	13
Figure 1.2	The Rice-Herzfeld pyrolysis mechanism consisting of bond homolysis, hydrogen abstraction, $\beta$ -scission and radical recombination steps. $\beta$ and $\mu$ represent radicals.....	14
Figure 1.3	The additional steps for the Rice-Herzfeld mechanism in the presence of an additive, $\mu_2\text{H}$ which can participate in hydrogen transfer steps. The additive is consumed and regenerated and thus can be considered to act as a catalyst.....	14
Figure 1.4	Calculated rate enhancement curve for dibenzyl ether ( $d_{\beta_1\text{-H}}^\circ = 85.0$ kcal/mole, $d_{\mu_1\text{-H}}^\circ = 78.9$ kcal/mole, $S_2 = 1000$ , $350^\circ\text{C}$ ), with the enhancements by hydrogen transfer additives placed by bond strength. ....	17
Figure 1.5	Effect of the presence of $\text{CS}_2$ on the reaction kinetics of dibenzylether at $345^\circ\text{C}$ in an excess of tetralin. ....	17
Figure 1.6	Rate enhancement (E) depends on the structure of the reactant ( $d_{\mu_1\text{-H}}^\circ$ ) as well as the structure of the additive ( $d_{\mu_2\text{-H}}^\circ$ ). This surface assumes a benzyl radical chain carrier ( $d_{\beta_1\text{-H}}^\circ = 85.0$ kcal/mole) at a temperature of $350^\circ\text{C}$ .....	18
Figure 1.7	Model mechanism for methylnaphthalene dealkylation over a metal catalyst (M).....	19
Figure 1.8	Estimated methylnaphthalene rate due to the reaction scheme shown in Figure 1.7. A priori first estimates for the LFER parameters: $\log_{10}A_1 = \log_{10}A_2 = 7.0$ , $\alpha_1 = \alpha_2 = 0.5$ , $E_1 = 11.0$ and $E_2 = 16.0$ . ....	19
Figure 1.9	The structure of the coal model compound 4-(1-naphthylmethyl)-bibenzyl (NBBM). The scissile bonds are labeled A through E. ....	20

Figure 2.1	The structure of the coal model compound 4-(1-naphthylmethyl)-bibenzyl (NBBM). The scissile bonds are labeled A through E. ....	29
Figure 2.2	Disappearance kinetics for NBBM pyrolysis at 420 °C under a pressure of 1000 psig (cold) of either hydrogen or nitrogen. Error bars are two standard deviations in each direction as calculated from repeated measurements. ....	32
Figure 2.3	Selectivity versus reactant conversion plot for NBBM Bond A scission products. Products with positive finite intercepts are primary and products with zero intercepts are of higher rank. Error bars are two standard deviations in each direction as calculated from repeated measurements. ....	35
Figure 2.4	Representative radical ipso-substitution pathway for cleavage of bond A by a benzyl radical. ....	36
Figure 2.5	Proposed mechanism for the pyrolysis of NBBM through radical pathways. ....	37
Figure 2.6	Plot of molar yields versus reactant conversion of NBBM Bond A products for pyrolysis under nitrogen. The stoichiometry is consistent with the benzyl radical attack mechanism. ....	38
Figure 2.7	Plot of molar yields versus reactant conversion of NBBM Bond A products for pyrolysis under hydrogen. The stoichiometry is consistent with the benzyl radical and hydrogen radical attack mechanisms. ....	39
Figure 2.8	Disappearance with time of NBBM at 400 °C under a hydrogen atmosphere. ....	41
Figure 2.9	Selectivity versus conversion for bond A scission products at 400 °C. ....	41
Figure 2.10	Product classes observed for NBBM pyrolysis at 400 °C under hydrogen. ....	42
Figure 2.11	Disappearance kinetics for NBBM hydropyrolysis at 420 °C. ....	43
Figure 2.12	Contributions of the major product families (bond A scission, bond B scission, bond D scission and NBBM hydrogenation) for NBBM hydropyrolysis at 420 °C. ....	44
Figure 2.13	Bond A scission products for NBBM hydropyrolysis at 420 °C. ....	45
Figure 2.14	Bond B scission products for NBBM hydropyrolysis at 420 °C. ....	45
Figure 2.15	Bond D scission products for NBBM hydropyrolysis at 420 °C. ....	46

Figure 3.1	The structure of the coal and resid model compound 4-(1-naphthylmethyl)bibenzyl (NBBM). The scissile bonds are labeled A through E.....	53
Figure 3.2	Non-free radical reaction families included in NBBM model: (A) naphthyl hydrogenation; (B) olefin hydrogenation.....	61
Figure 3.3	Results of parameter regression for the mechanistic model describing NBBM pyrolysis at 420 °C in a hydrogen atmosphere.....	68
Figure 3.4	Reaction paths for NBBM disappearance and their relative contributions for NBBM hydropyrolysis at 420 °C.....	71
Figure 3.5	NBBM reaction cycle which effects transformation of R• radicals to H• radicals. This cycle is predicted by the mechanistic kinetics model for NBBM hydropyrolysis at 420 °C.....	72
Figure 3.6	Rates of relevant elementary steps of naphthyltolylmethane as predicted by the mechanistic model.....	74
Figure 3.7	Rates of relevant elementary steps of p-xylene as seen through the actions of the p-xylene benzylic radical.....	75
Figure 3.8	Reactivities of naphthyltolylmethane as predicted by the mechanistic model.....	76
Figure 4.1	The structure of the coal model compound 4-(1-naphthylmethyl)-bibenzyl (NBBM). The scissile bonds are labeled A through E.....	87
Figure 4.2	Lumped reaction network describing NBBM catalysis at 400 °C.....	88
Figure 4.3	Effect of atmosphere on NBBM conversion for reaction in the presence of the iron carbonyl-based catalyst precursor $\text{Fe}(\text{CO})_3(\text{PPh}_3)_2$ at 420 °C. The error bars represent two standard deviations as obtained from repeated experiments.....	89
Figure 4.4	Selectivity versus Conversion for NBBM reaction in the presence of the iron carbonyl-based catalyst precursor $\text{Fe}(\text{CO})_3(\text{PPh}_3)_2$ at 420 °C. The error bars represent two standard deviations as obtained from repeated experiments.....	90
Figure 4.5	Yield versus NBBM conversion for bond A scission products produced during reaction in the presence of $\text{Fe}(\text{CO})_3(\text{PPh}_3)_2$ at 420 °C. The error bars represent two standard deviations as obtained from repeated experiments.....	91
Figure 4.6	Comparison of tetralin yields between NBBM catalysis and pyrolysis at 420 °C under a hydrogen atmosphere. The error bars	



	represent two standard deviations as obtained from repeated experiments.....	92
Figure 4.7	Disappearance kinetics for NBBM reaction at 400 °C in the presence of the iron carbonyl-based catalyst precursors: $\text{Fe}(\text{CO})_4\text{PPh}_3$ , $\text{Fe}(\text{CO})_3(\text{PPh}_3)_2$ , and $\text{Fe}(\text{CO})_2(\text{PPh}_3)_2\text{CS}_2$ . The error bars for the $\text{Fe}(\text{CO})_4\text{PPh}_3$ and $\text{Fe}(\text{CO})_3(\text{PPh}_3)_2$ data series represent two standard deviations as obtained from repeated experiments.....	93
Figure 4.8	Molar yields of NBBM product classes for reaction with $\text{Fe}(\text{CO})_4\text{PPh}_3$ at 400 °C.....	94
Figure 4.9	Molar yields of NBBM product classes for reaction with $\text{Fe}(\text{CO})_3(\text{PPh}_3)_2$ at 400 °C.....	95
Figure 4.10	Molar yields of NBBM product classes for reaction with $\text{Fe}(\text{CO})_2(\text{PPh}_3)_2\text{CS}_2$ at 400 °C.....	95
Figure 4.11	Model fits for the lumped network describing the reaction of NBBM at 400 °C under 1000 psig $\text{H}_2$ (cold) in the presence of iron carbonyl based catalyst precursors. The lines are the predicted curves and the points are the experimentally measured values.....	97
Figure 4.12	NBBM disappearance kinetics for reaction in the presence of the transition metal-based catalysts.....	100
Figure 4.13	Molar yield of bond A scission products (naphthalene + tetralin) as a function of NBBM conversion for NBBM reaction with $\text{Fe}(\text{CO})_5$ , $\text{Mo}(\text{CO})_6$ , $\text{Fe}_2\text{O}_3$ and $\text{MoS}_2$ catalytic materials. ....	102
Figure 4.14	Molar yield of bond B scission products (methylnaphthalene + methyltetralin) as a function of NBBM conversion for NBBM reaction with $\text{Fe}(\text{CO})_5$ , $\text{Mo}(\text{CO})_6$ , $\text{Fe}_2\text{O}_3$ and $\text{MoS}_2$ catalytic materials.....	102
Figure 4.15	Molar yield of naphthyl hydrogenation products (naphthalene + tetralin) as a function of NBBM conversion for NBBM reaction with $\text{Fe}(\text{CO})_5$ , $\text{Mo}(\text{CO})_6$ , $\text{Fe}_2\text{O}_3$ and $\text{MoS}_2$ catalytic materials. ....	103

Figure 5.1	The structure of the coal and resid model compound 4-(1-naphthylmethyl)bibenzyl (NBBM). The scissile bonds are labeled A through E.....	111
Figure 5.2	Cluster geometry used for the bcc metal structures of Fe and Mo. ....	125
Figure 5.3	Cluster geometry used for the distorted fcc structure of Mn.....	125
Figure 5.4	Cluster geometry used for the hexagonal structure of $\text{Fe}_2\text{O}_3$ . The darker shaded atoms are Fe and the lighter shaded atoms are O. ....	125
Figure 5.5	Cluster geometry used for the hexagonal structure of $\text{MoS}_2$ . The darker shaded atoms are Mo and the lighter shaded atoms are S.....	126
Figure 5.6	Alternate reaction paths leading to dissociative adsorption of $\text{H}_2$ on a metal surface.....	127
Figure 5.7	Chemical equation for an ipso insertion of a catalytically bound hydrogen atom to an aromatic ring. ....	130
Figure 5.8	Parity plot for the NBBM mechanistic model describing catalytic reaction of NBBM at 400 °C under hydrogen with $\text{Fe}(\text{CO})_5$ , $\text{Mo}(\text{CO})_6$ , $\text{Mn}_2(\text{CO})_{10}$ , $\text{Fe}_2\text{O}_3$ and $\text{MoS}_2$ on a logarithmic scale. ....	133
Figure 5.9	Parity plot for the NBBM mechanistic model describing catalytic reaction of NBBM at 400 °C under hydrogen with $\text{Fe}(\text{CO})_5$ , $\text{Mo}(\text{CO})_6$ , $\text{Mn}_2(\text{CO})_{10}$ , $\text{Fe}_2\text{O}_3$ and $\text{MoS}_2$ on a linear scale. ....	133
Figure 5.10	Model predictions and experimental data describing the catalytic disappearance of NBBM at 400 °C under hydrogen with $\text{Fe}(\text{CO})_5$ , $\text{Mo}(\text{CO})_6$ , $\text{Mn}_2(\text{CO})_{10}$ , $\text{Fe}_2\text{O}_3$ and $\text{MoS}_2$ . ....	134
Figure 5.11	Model predictions and experimental data for the bond A scission products methylbibenzyl and p-xylene from reaction of NBBM at 400 °C under hydrogen with $\text{Fe}(\text{CO})_5$ , $\text{Mo}(\text{CO})_6$ , $\text{Mn}_2(\text{CO})_{10}$ , $\text{Fe}_2\text{O}_3$ and $\text{MoS}_2$ .....	134
Figure 5.12	Model predictions and experimental data for NBBM hydrogenation products from reaction of NBBM at 400 °C under hydrogen with $\text{Fe}(\text{CO})_5$ , $\text{Mo}(\text{CO})_6$ , $\text{Mn}_2(\text{CO})_{10}$ , $\text{Fe}_2\text{O}_3$ and $\text{MoS}_2$ . ....	135
Figure 5.13	Plot of molar yield of unoccupied catalyst sites as a function of reaction time for Fe, Mo, $\text{Fe}_2\text{O}_3$ and $\text{MoS}_2$ clusters.....	137
Figure 5.14	Plot of molar yield of catalytically bound, naphthalene containing molecules as a function of reaction time for Fe, Mo, Mn, $\text{Fe}_2\text{O}_3$ and $\text{MoS}_2$ clusters.....	137

Figure 5.15	Plot of molar yield of catalytically bound H atoms as a function of reaction time for Fe, Mo, Fe <sub>2</sub> O <sub>3</sub> , and MoS <sub>2</sub> clusters.....	138
Figure 5.16	The product of the molar yields of catalytically bound hydrogen atoms and catalytically bound NBBM molecules as a function of reaction time.....	139
Figure 5.17	The product of the molar yields of catalytically bound hydrogen atoms to the fourth power and catalytically bound NBBM molecules as a function of reaction time.....	140
Figure 5.18	Plot of the half life for NBBM disappearance as a function of the ASED-MO estimated metal-naphthalene adsorption enthalpy. ....	141
Figure 5.19	Structure-function relationship for the relative contribution of the hydrogenation and bond scission reaction families to the reaction of NBBM at 400 °C in a hydrogen atmosphere.....	142
Figure 6.1	The structure of the coal model compound 4-(1-naphthylmethyl)-bibenzyl (NBBM). The scissile bonds are labeled A through E. ....	149
Figure 6.2	Structure-function relationship for the relative contribution of the hydrogenation and bond scission reaction families to the reaction of NBBM at 400 °C in a hydrogen atmosphere.....	155

## ABSTRACT

The thermal and catalytic reactions of 4-(1-naphthylmethyl)bibenzyl (NBBM), a resid and coal model compound, were examined. Hydropyrolysis at 420 °C gave tetrahydro-NBBM, 4-(1-naphthylmethyl)toluene, toluene, naphthalene, methylbibenzyl, 4-(1-naphthylmethyl)benzene, methylnaphthalene, bibenzyl, tetralin and p-xylene as products. These results can be explained by a set of free radical elementary steps involving bond fission, hydrogen abstraction,  $\beta$ -scission, radical addition, radical hydrogen transfer, radical disproportionation and radical recombination. Catalytic reaction of NBBM was carried out at 400 °C under hydrogen with a series of transition metal-based catalytic materials including  $\text{Fe}(\text{CO})_4\text{PPh}_3$ ,  $\text{Fe}(\text{CO})_3(\text{PPh}_3)_2$ ,  $\text{Fe}(\text{CO})_2(\text{PPh}_3)_2\text{CS}_2$ ,  $\text{Fe}(\text{CO})_5$ ,  $\text{Mo}(\text{CO})_6$ ,  $\text{Mn}_2(\text{CO})_{10}$ ,  $\text{Fe}_2\text{O}_3$  and  $\text{MoS}_2$ . Reaction in the presence of these catalysts and catalyst precursors gave the same products as observed during pyrolysis with the addition of the hydrogenation products 4-(1-tetrahydronaphthylmethyl)toluene and methyltetralin. These results are consistent with additional elementary steps involving hydrogen and naphthyl adsorption/desorption, ipso addition of catalytically bound H atoms, surface hydrogenation and surface recombination.

These experimental findings and derived mechanistic insights were organized into molecular-level reaction models for NBBM pyrolysis and catalysis. Hydropyrolysis and catalysis reaction families occurring during NBBM hydropyrolysis at 420 °C were summarized in the form of reaction matrices which, upon exhaustive application to the components of the reacting system, yielded the

mechanistic reaction model. Each reaction family also had an associated linear free energy relationship (LFER) which provided an estimate of the rate constant  $k_i$  given a structural property of species  $i$  or its reaction. Optimization of the LFER parameters to provide the best fit between the hydrolysis model and the experimental data provided fundamental kinetic parameters as well as insight into the controlling reaction mechanisms contributing to the product spectra.

Including the catalytic reaction matrices with those for the pyrolysis model provided a comprehensive NBBM catalytic reaction model and allowed regression of fundamental LFER parameters for the catalytic reaction families. Results from the catalytic reaction model suggest that the energetics of the naphthalene-metal interaction determine the relative surface concentrations of hydrogen and naphthyl-containing molecules, which ultimately determine the activity and selectivity of a catalyst in the NBBM system. The model also allowed specification of the property of an optimal catalyst. Iron, molybdenum and palladium were predicted to be most effective for model compound consumption. Due to the low costs associated with iron and its disposal, it is a good choice for coal liquefaction catalysis and the challenge remains to synthesize small particles able to access the full surface area of the coal macromolecule.

## Chapter 1

### INTRODUCTION

The potential for the cost of crude petroleum feeds to rise and the volatile politics of the Middle East to affect supply continue to drive the search for different sources of hydrocarbon-based fuels. Due to its large domestic supply in the United States, coal is an attractive energy source to meet present and future needs. The direct liquefaction of coal to petroleum-like liquid fuels is one application which can take advantage of this coal stockpile. However, in order to commercialize direct coal liquefaction economically, a fundamental understanding of the chemical and physical processes which occur during liquefaction must be understood.

#### 1.1 Direct Coal Liquefaction

The goal of coal liquefaction is to fragment the macromolecular coal structure into lower molecular weight materials which may then undergo upgrading to usable liquid fuel products. Liquefaction conditions involve the thermal treatment of solid coal (350-450 °C), usually in the presence of a hydrogen donating solvent and/or in the presence of a pressurized hydrogen atmosphere. Liquefaction is commonly believed to proceed through a free radical mechanism consisting of bond cleavage followed by the capping of the resulting radicals with hydrogen obtained from either the coal itself, the solvent or the gaseous hydrogen atmosphere. However, inherent with free radical reactions are retrogressive reactions which involve recombination or

addition of radical species to form higher molecular weight products. This is counter to the desired result.

In order to reduce the effects of retrogressive reactions and also increase the rate of solids dissolution, a catalyst is often used in coal liquefaction. The choice of a catalyst for the coal liquefaction system involves physical as well as chemical effects. Broadly, the two desirable catalytic reactions in coal liquefaction are bond scission and aromatic hydrogenation. An optimal selectivity to lower molecular weight liquid products requires both bond breaking activity, and the ability to cap free radicals before they participate in retrogressive reactions. In addition, fine particle catalysts are desirable because they can access the microporous structure of the coal to catalyze reaction on a larger surface area. Also, a cheap and environmentally benign material is beneficial so that the used catalyst may be disposed of with the unreacted coal char following liquefaction. All of these factors should be considered when choosing a catalyst for coal liquefaction.

## **1.2 Coal Liquefaction Catalysis**

Three broad categories of coal liquefaction catalysts which have been reported in the literature are supported acid cracking catalysts, superacid catalysts and unsupported fine-particle transition metal catalysts. All three categories of catalysts have been used with coal and coal-related reactants as well as with model compounds.

### **1.2.1 Supported Acid Catalysts**

Acid cracking catalysts are known to catalyze depolymerization reactions during coal liquefaction. To probe their possible application to coal liquefaction, Ouchi et al. (1973) examined a series of solid and homogeneous acid catalysts in a coal liquefaction system. They found a general correlation between acid strength of

catalysts and activity for coal depolymerization to liquid products. In a similar vein, McCormick et al. (1989) examined a series of supported catalysts varying support materials and acid site densities for coal liquefaction. They also observed the acidity-activity correlation for isomerization and cracking reactions, and suggested the benefits of acid catalysts for coal liquefaction.

Additional work with supported acid catalysts has also been performed using coal model compounds (Patzner et al., 1979; Groot et al., 1986; Lemberon et al., 1988; Afifi et al., 1989; and Hattori et al., 1985). This work has shown the facility of acid functions for breaking the carbon-carbon and carbon-oxygen bonds in coal. However, work by Larsen and Lee (1983) shows that very strong acid strengths also increase the rates of condensation reactions within coal. This will compete with the depolymerization reactions and lead to low overall activities. Overall, acid catalysts have been shown to aid in coal depolymerization through their isomerization and cracking activity, but they also catalyze retrogressive reactions at high acid strengths.

### **1.2.2 Superacid Catalysts**

Superacid catalysts (very high acid strength) have been examined for coal liquefaction with the goal of being able to carry out liquefaction at low temperatures (less than 250 °C). Olah et al. (1984a and 1984b) reported a series of papers in which they examined several superacid catalytic systems which showed coal liquefaction activity at low temperatures (100 °C - 200 °C). They found the catalytic combination of hydrogen fluoride, borontrifluoride and molecular hydrogen to be most effective of the systems they examined. In addition, the superacid activity for destruction of specific bonds was probed through reaction with model compounds. Complete destruction of model compounds which contain relatively weak bonds (bibenzyl and



diphenylmethane) was effected at room temperature, whereas compounds with stronger bonds (biphenyl, diphenyl ether and quinoline) required elevated temperatures (greater than 100 °C) and the presence of molecular hydrogen for reaction. Further work by Farcasiu (1986) examined model compound reactions in the presence of the superacid catalyst trifluoromethanesulfonic acid. This work reinforced the findings of Olah in that the superacid catalyst was observed to have activity for breaking the strong bonds between an aromatic and an aliphatic carbon. However, the practical implementation of these superacid systems suffers from the costs of dealing with highly corrosive environments.

### 1.2.3 Unsupported Metal Catalysts

Unsupported fine-particle metal catalysts are advantageous for use during coal liquefaction due to their small particle size. Moreover, many of these catalysts can be synthesized *in situ* from homogeneous catalyst precursors. This method of catalyst formation allows the catalyst to access a much larger fraction of the coal's surface area than is possible with traditional supported catalysts. In addition, the hydrogenation ability of metals, in addition to cracking activity, make these metal catalysts more effective for a wide range of reactions than the acid catalysts discussed earlier. Due to the beneficial aspects of a metal fine-particle catalytic system, many examples of these catalysts appear in the recent literature.

Several transition metals have shown activity for increasing the rate and selectivity of coal liquefaction. The metals which have shown the highest activity and have been used in most of the reported studies are iron, molybdenum and, to a lesser extent, nickel. These three metals have been examined in their reduced and sulfided

states with the reduced metals providing more hydrogenation activity and, in most cases, the sulfides providing more hydrogenolysis activity.

Iron-based catalysts have been shown to exhibit activity for coal liquefaction in several forms including oxide, sulfide and reduced metal (Andrés et al., 1983; Watanabe et al., 1984; Herrick et al., 1990; Prégermain, 1985; Takemura et al., 1985; Pradhan et al., 1991, 1992; Huffman et al., 1993; and Zhang et al., 1994). Coal liquefaction reactions were performed either in the presence of a hydrogen donor solvent, atmospheric hydrogen or both. The iron catalysts take the form of pyrrhotite in the presence of an external sulfur source or the sulfur present in coal (Herrick, 1990). In the absence of sufficient sulfur, iron oxides are formed, and in reducing atmospheres the metal may be reduced.

In-depth analyses of the iron structure during coal liquefaction have also been reported. Cook and Cashion (1987) and Yamashita et al. (1989) used Mössbauer spectroscopy to examine the state of iron *in situ* during coal liquefaction. Yamashita observed initial degradation of their iron nitrate catalyst precursor to ferric oxyhydroxide (FeOOH), whereas Cook and Cashion started with FeOOH. Both workers observed that in the presence of a hydrogen atmosphere the FeOOH was reduced to Fe<sub>2</sub>O<sub>3</sub>, and then further reduced to  $\alpha$ -Fe metal. Both workers propose that the reduced  $\alpha$ -Fe is primarily responsible for increases in liquefaction yields in their systems.

In addition to coal liquefaction experiments, fine-particle iron catalysts have been reacted with model compounds in order to examine the specific reactivities catalyzed by the metal. Specifically, Zhan and Guin (1994) have observed hydrogenation activity of metal catalysts with reduced iron phases having the highest hydrogenation activity, iron oxide phases with intermediate hydrogenation activity and

iron sulfide phases having very little hydrogenation activity. Additionally, Farcasiu et al. (1994a and 1994b) examined the reactivity of iron oxide and iron sulfide catalysts with polyfunctional model compounds and have observed activity for cleavage of bonds between an aromatic and an aliphatic carbon as well as dehydroxylation, demethoxylation, isomerization and hydrogenation.

Linehan et al. (1994) investigated the relationship between the structure of iron-oxygen catalyst precursors and the ability of the ultimate catalytic material to carry out carbon-carbon bond scission in model compounds. Furthermore, Tang and Curtis (1994) observed hydrogenation ability as well as carbon-carbon bond scission ability with slurry-phase iron-based catalysts in model compound systems. This body of evidence suggests that the iron catalysts can perform both the hydrogenolysis and hydrogenation functions required for efficient coal liquefaction.

The general message of the literature is that the role of the iron catalysts is that of hydrogen transfer. Hydrogen transfer has been observed from the gas phase to coal, from the gas phase to the donor solvent and from the donor solvent to the coal. All of these mechanisms contribute to the activity of iron-based catalysts for coal liquefaction.

In addition to iron, molybdenum has commonly been used as an unsupported catalyst for coal liquefaction. Burgess et al. (1992), Bockrath et al. (1992) and Swanson (1992) describe illustrations of molybdenum-catalyzed coal liquefaction. All three of these examples describe results under conditions at which the active catalytic species is molybdenum sulfide. As with iron, the molybdenum will become sulfided in the presence of sulfur and in a reducing atmosphere will reduce to molybdenum metal.

Model compound reactions with molybdenum-based catalysts have also been performed. The results of these reactions show similar functionality as was observed by the iron catalysts. Hydrogen-transfer from the gas phase to the model compounds was observed (Ikenaga et al., 1994) as well as hydrogenolysis, hydrogenation (Suzuki et al., 1989) and hydrodenitrogenation (Curtis and Cahela, 1989). The role of the molybdenum catalysts seems to be the same as their iron counterparts, however, in general the molybdenum-based catalysts are more active than the iron-based catalysts.

### 1.3 Model Compounds

In order to gain a fundamental understanding of coal liquefaction, the specific chemical reactions which occur during liquefaction must be quantified. Due to the complex nature of coal, it is impossible to observe specific reactions during a coal experiment. To this end, many coal researchers have employed model compounds, simple molecules which mimic some feature of coal, to examine the reactivities of the chemical structures found in coal.

The types of model compounds which are employed were inspired by the coal structure models which have been developed. These structure models (Given, 1960; Wiser, 1975; Shinn, 1984; and Provine, 1992b) have represented the analytical chemistry data available in the form of the functional groups found in coal. Coal structures are then constructed with the functional groups so that the structure formed has the same properties which have been observed for real coals. The aggregate structures include aromatic clusters connected by short alkyl chains with both rings and connecting groups containing carbon, sulfur, oxygen and nitrogen. These models have led to the examination of many model compounds mimicking these features.

Poutsma (1987 and 1990) has written comprehensive reviews of the coal model compound literature including rate and pathways information for free-radical hydrocarbon chemistries. Stein (1981) showed that application of thermochemical analyses to the reactions of the model compounds provides valuable insight into the reaction pathways and mechanism which occur during coal liquefaction.

In addition, a series of papers (McMillen et al., 1987a, 1987b; Malhotra et al., 1989; and McMillen and Malhotra, 1990, 1992) have appeared in which kinetic and thermochemical principles are applied to recombination and hydrogenolysis reactions of coal model compounds. Their analyses lead to the suggestion of a novel free-radical elementary step (radical hydrogen transfer), which leads to the cleavage of strong carbon-carbon bonds between alkyl and aromatic structures. In addition, McMillen et al. (1990) constructed a mechanistic-based kinetics model for the reaction of coal model compounds employing radical hydrogen transfer, reverse radical disproportionation, ipso-substitution and other free-radical elementary steps to describe the reaction of coal model compounds. Thermochemical relations (linear free energy relationships or LFERs) were used to estimate the values of the rate constants for each step from its heat of reaction. The model effectively described experimental results obtained from the reactions of phenanthrene and anthracene.

Recently, polyfunctional model compounds which contain several functionalities found in coal have also been examined (Farcasiu et al., 1991, 1994b). These compounds have the advantage of allowing the interactions between functional groups, both thermally and catalytically, to be examined which better mimic the actual chemistries occurring during coal liquefaction. In addition, the catalytic reactivity of the polyfunctional model compound 4-(1-naphthylmethyl)bibenzyl (Farcasiu and

Smith, 1991) has been shown to correlate with the rate of catalytic coal liquefaction (Linehan et al., 1993; and Guin et al., 1993).

#### 1.4 Linear Free Energy Relationships (LFERs)

LFERs can be a powerful tool for summarizing and predicting rate constants in mechanistic based kinetics models. Neurock and Klein (1993) have demonstrated the applicability of LFERs as used for correlation of rate constants to a property of the reacting molecules for a wide range of chemistries. This method allows, once the correlation parameters for the reaction family have been established, the prediction of rate constant values from computational quantum chemistry calculations only; additional experimentation is not required.

The original LFER is Hammett's (Lowry and Richardson, 1987) organization of substituent effects for homogeneous reactions of substituted benzenes. In addition, Evans and Polanyi (1938) and Dewar (1969) have examined the correlation between heat of reaction and rate constant, a commonly used form of the LFER. The Evans-Polanyi relation for activation energies has been employed (LaMarca et al., 1993) to investigate the thermochemistry of a model coal system. Their analysis is the basis upon which the work described in this document is built.

In order to examine chemistries which occur on a solid catalyst, LFERs such as the Evans-Polanyi relation must be applicable to heterogeneous kinetic systems. Catalytic heterogeneous systems are more difficult to consider than their homogeneous counterparts due to uncertainty of the chemical mechanism and of the structures of possible intermediates. However, several examples in the literature suggest the validity of LFERs for heterogeneous catalytic reactions (Mochida and Yoneda, 1967; Yoneda, 1967; Matsumoto et al., 1968; Dunn, 1968; Dumesic et al.,

1987; and Landau et al., 1992). Thus, if a good estimate of the rate determining step (RDS) is available, then an LFER relating the overall rate of the reaction to a property relevant to the RDS is accessible. Additionally, an LFER describing each individual step of a model reaction path should be valid as long as the model sufficiently describes the real reaction path.

### 1.5 Catalyst Design

Given the ability to model thermal and catalytic reactions which occur in coal, the next logical step is to use these tools to specify an active catalyst for coal liquefaction. Catalyst design is still at a stage where it depends on art and personal experience as well as science. However, this reality is changing. Specifically, knowledge-based computer models have recently been explored for the purpose of cataloguing and aiding in catalyst design.

Hu, Foley and Stiles (1991) have used a knowledge-based, expert system approach to aid in the specification of an optimal catalyst formulation for alcohol synthesis. Their approach integrates information on catalyst performance, reaction mechanism and the active sites gained from many years of experimental trial and error and implements design rules which attempt to mimic the thought process of an experienced catalyst designer. Dumesic et al. (1987) have also designed a similar system for heterogeneous catalyst design for very specific reactions on a solid. The disadvantages of these types of catalyst design programs is that a great deal of experimental data is needed to fill out the databases for each specific chemistry and as

a result, each new chemistry or reactant requires a large database of new experimental data. A more desirable system would be flexible so that the reactant could be varied and few experiments would be required to determine the properties of an optimal catalyst.

The work of both Hu, Foley and Stiles and that of Dumesic recognized the reaction mechanism as a significant attribute necessary to determine the action of the catalyst. In a similar mode, LaMarca et al. (1990, 1993) performed extensive kinetic modeling of free-radical chain reactions of coal model compounds. As a result of this modeling, a formalism was proposed which, through LFERs, related the rate of disappearance of the reactant to a property of a homogeneous catalytic additive. This formalism allows specification of a property of an optimal additive given the reaction mechanism of the reactant (neat and catalytically) and the LFER parameters to specify relevant rate constants. LaMarca's formalism applies to any reactant which proceeds through the specified free-radical chemistries. The next section will discuss the work of LaMarca and its application to the work presented in this document.

### 1.5.1 Kinetics-Assisted Design of Catalysts

The guiding formalism throughout this work is the concept of reaction cycles for both pyrolysis and catalysis. Reaction cycles in free radical reactions have long been represented by the Rice-Herzfeld pyrolysis mechanism (LaMarca et al., 1990). Catalytic cycles have similarities to Rice-Herzfeld and may be represented in a similar manner.

There are two roles a coal liquefaction catalyst may assume which result in an increased selectivity to liquid products. The first is that of an additive which will increase the rate of the thermal bond breaking reactions relative to the bond making



reactions, and the second is to create new bond breaking reactions in addition to those which occur thermally. Both of these types of catalytic actions are addressed in the following analysis.

Thermal coal liquefaction reaction families include bond homolysis, hydrogen abstraction,  $\beta$ -scission, radical-induced hydrogen transfer, radical recombination and radical addition as shown in Figure 1.1. The bond breaking reactions (bond homolysis,  $\beta$ -scission and radical-induced hydrogen transfer) are desirable in coal liquefaction, and the bond forming reactions (radical recombination and radical addition) are undesirable. These reaction families can be represented by the Rice-Herzfeld formalism.

Figure 1.2 shows the Rice-Herzfeld pyrolysis mechanism including bond thermolysis, hydrogen abstraction,  $\beta$ -scission and radical recombination.  $\beta$  and  $\mu$  radical species. A  $\beta$  radical is formed from a bond breaking sequence of the reactant,  $A_1$ , by either bond homolysis or  $\beta$ -scission, and a  $\mu$  radical is formed by hydrogen abstraction from the reactant. The rate law for neat pyrolysis, in terms of observables (LaMarca, 1992), is shown as Equation 1.1.

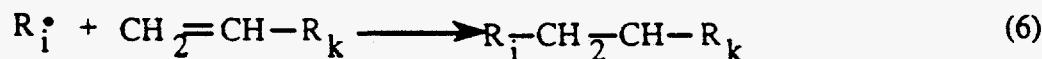
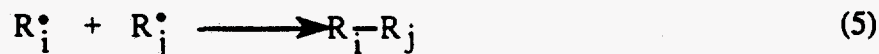
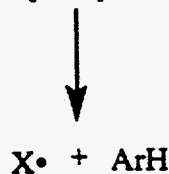
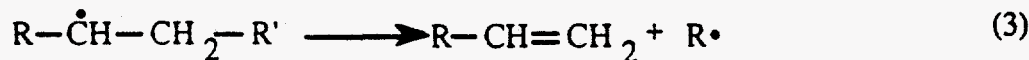
$$r_{A_1}([A_1]) = \left( \frac{\alpha_1[A_1]}{k_t} \right)^{\frac{1}{2}} k_{11}[A_1] \quad (1.1)$$

The steps for the addition of a solvent,  $\mu_2H$ , which can undergo hydrogen transfer but not  $\beta$ -scission, are shown in Figure 1.3. Moreover, the rate law considering the addition of the hydrogen transfer solvent (LaMarca, 1992) (incorporating the all the steps shown in Figures 1.2 and 1.3) is shown as Equation 1.2.

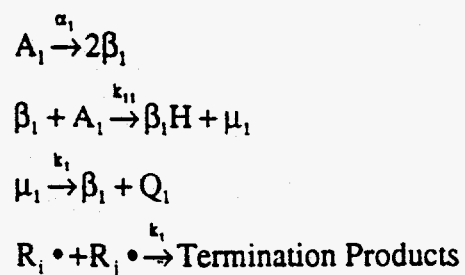
$$r_{A_1}([A_1], [\mu_2H]) = \left( \frac{\alpha_1[A_1]}{k_t} \right)^{\frac{1}{2}} \frac{k_{11}A_1(1 + \hat{k}'\Theta'S_2)}{(1 + \hat{k}'S_2)}; \quad \hat{k}' = \frac{k_{12}}{k'_{21}}, \Theta' = \frac{k'_{21}}{k_{11}}, S_2 = \frac{[\mu_2H]}{[A_1]} \quad (1.2)$$

The rate enhancement due to the solvent,  $E$ , is defined as the rate of disappearance of the reactant in the presence of the solvent divided by the rate of disappearance of the reactant without the solvent. The simple expression of Equation 1.3 describes the effectiveness of the solvent in terms of the ratios of rate constants within a reaction family and the amount of solvent added.

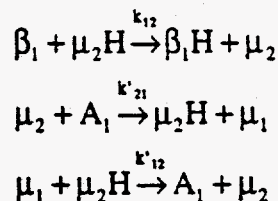
$$E = \frac{r_{A_1}([A_1], [\mu_2 H])}{r_{A_1}([A_1])} = \frac{(1 + \hat{k}' \Theta S_2)}{(1 + \hat{k}' S_2)} \quad (1.3)$$



**Figure 1.1** Coal liquefaction reaction families: (1) bond homolysis, (2) hydrogen abstraction, (3)  $\beta$ -scission, (4) radical-induced hydrogen transfer, (5) radical recombination, and (6) radical disproportionation.



**Figure 1.2** The Rice-Herzfeld pyrolysis mechanism consisting of bond homolysis, hydrogen abstraction,  $\beta$ -scission and radical recombination steps.  $\beta$  and  $\mu$  represent radicals.



**Figure 1.3** The additional steps for the Rice-Herzfeld mechanism in the presence of an additive,  $\mu_2 H$  which can participate in hydrogen transfer steps. The additive is consumed and regenerated and thus can be considered to act as a catalyst.

Figure 1.4 depicts the enhancement,  $E$ , as a function of  $\mu_2$ -H bond strength ( $d^{\circ}_{\mu_2-H}$ ) for the model compound dibenzyl ether ( $DBE \equiv A_1 \equiv \mu_1 H$ ). Several common hydrogen donor solvents have been placed on the calculated curve according to their  $\mu_2$ -H bond strength. Note that  $H_2S$  falls near the peak of this curve. Sulfur compounds have been shown to accelerate the rate of DBE consumption (Provine et al., 1992a), and  $H_2S$  is known to accelerate the rates for other coal model compounds (Hei et al., 1986; and Rebick, 1980), coal/oil coprocessing (Rahimi et al., 1987; and Cugini and Lett, 1989) and coal liquefaction (Hirschon and Laine, 1989; and Lambert, 1982). This point is

illustrated in Figure 1.5 which shows that for the model compound dibenzylether (DBE), reaction at 345 °C in an excess of tetralin shows no reaction after 8 minutes, while addition of 5 wt.% CS<sub>2</sub> to the reaction mixture, which will decompose to H<sub>2</sub>S upon heat-up shows a significant rise in the disappearance rate of DBE.

The optimal hydrogen transfer solvent depends on bond strengths of the reactant as well as that of the additive. Figure 1.6 shows the enhancement surface as a function of the thermochemistry of the reactant ( $d^{\circ}_{\mu 1-H}$ ) and that of the additive ( $d^{\circ}_{\mu 2-H}$ ). This figure clearly shows that the height and location of the maximum along the  $d^{\circ}_{\mu 2-H}$  axis depends on the bond strengths of the reactant.

The previous analysis describes a method for specifying a property of an optimal catalyst which increases the rate of existing reaction cycles in a system which follows long-chain Rice-Herzfeld kinetics. However, coal liquefaction and the reaction of coal liquefaction model compounds cannot be expected to follow only long-chain Rice-Herzfeld kinetics. For this kinetics-assisted design method to be applicable to coal liquefaction, it must be able to describe non-Rice-Herzfeld kinetics in which the role of the catalyst is to create new reaction cycles. The following example tests the kinetics-assisted design formalism for a non-Rice-Herzfeld system.

For this example, let us assume that the catalytic dealkylation of methylnaphthalene over a metal catalyst follows the mechanism illustrated in Figure 1.7. The mechanism involves dissociation of molecular hydrogen by the metal, insertion of a H• radical into the naphthalene ring, dealkylation of the radical intermediate and hydrogen abstraction by the methyl radical. Equation 1.4 shows the closed form solution describing the rate of methylnaphthalene disappearance, assuming a steady-state concentration of the ipso-substituted methylnaphthalene intermediate, for this mechanism. The rate depends only on the reactant concentration

([A]), the total metal concentration in the system ([M]), the concentration of molecular hydrogen and the rate constants  $k_1$  and  $k_2$ . Applying LFERs of the form found in Equation 1.5 to relate the activation energies to bond strengths, the rate is plotted as a function of the M-H bond strength in Figure 1.8. The rate versus bond strength plot shown in Figure 1.8 displays the characteristic maximum seen in the Rice-Herzfeld kinetics-assisted design analysis. This suggests that the kinetics-assisted design formalism may be applied to chemistries other than those that follow long-chain Rice-Herzfeld kinetics.

$$\text{rate} = \frac{k_2[A] \left( 2M + \frac{k_2[A]}{k_1[H_2]} \right)}{2} \left( 1 - \sqrt{\frac{4M^2}{\left( 2X + \frac{k_2[A]}{k_1[H_2]} \right)^2}} \right) \quad (1.4)$$

$$E_{\text{activation}} = E + \alpha \Delta H_{\text{reaction}} \quad (1.5)$$

The work presented here employs the kinetics-assisted design formalism and extends it to account for reaction cycles on solid catalysts. In addition, we will model the results from catalytic reactions of a model compound to develop a catalyst structure-function relationship for use in specifying properties of an optimally effective catalyst. This analysis may be effected by constructing experimental plots similar to Figure 1.8 for varying values of a physical property (i.e.,  $d_{\text{M-H}}^{\circ}$ ) within a family of additives, and then specifying the value of the additive which falls at the maximum of the curve. One would then be able to specify a physical property of an "optimal" additive for the increase in reaction rate of a compound. The kinetics-assisted design approach may also be extended to examine an overall reaction rate of complex mixtures such as coal. This has been demonstrated by Fake et al. (1994) for long-chain Rice-Herzfeld kinetics.

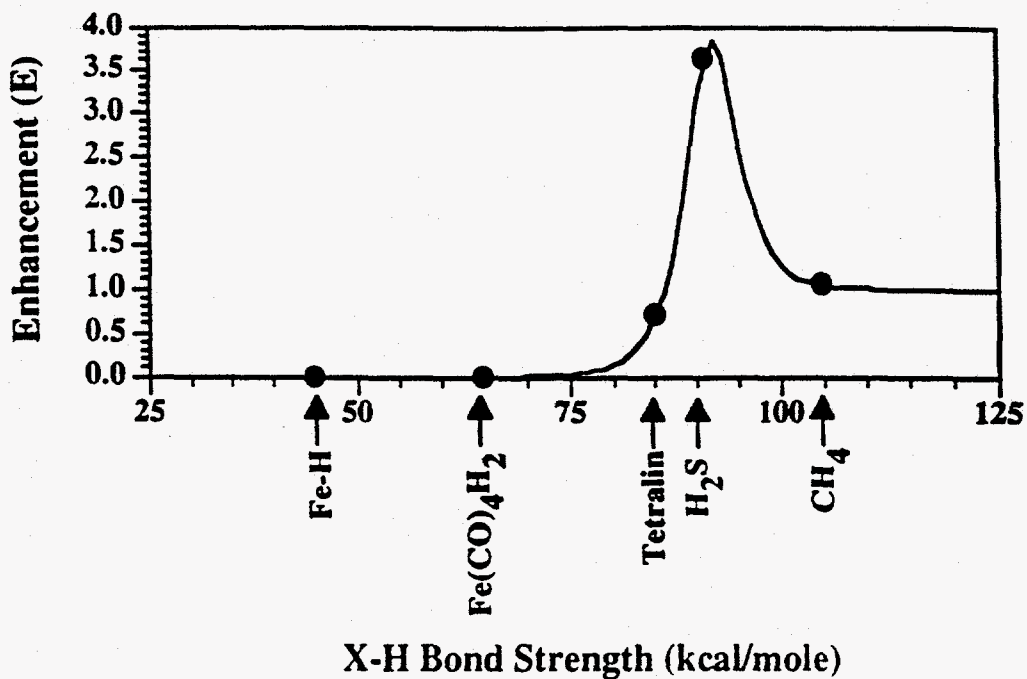


Figure 1.4 Calculated rate enhancement curve for dibenzyl ether ( $d_{\text{Bi,H}}^{\circ} = 85.0$  kcal/mole,  $d_{\text{Bi,H}}^{\circ} = 78.9$  kcal/mole,  $S_2 = 1000$ ,  $350^{\circ}\text{C}$ ), with the enhancements by hydrogen transfer additives placed by bond strength.

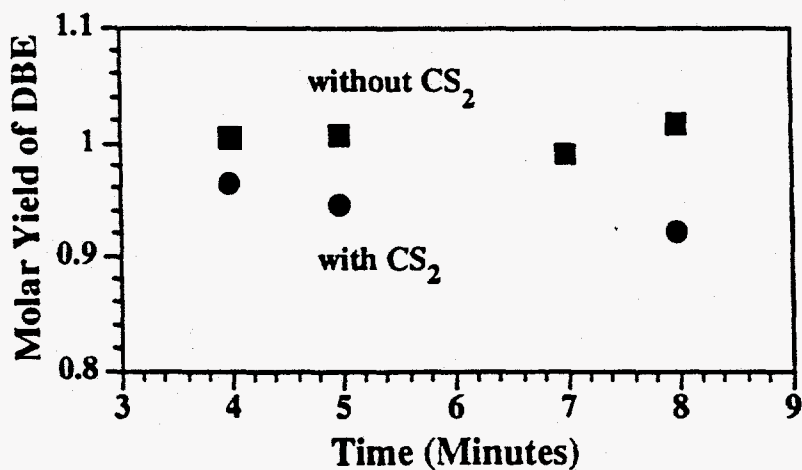
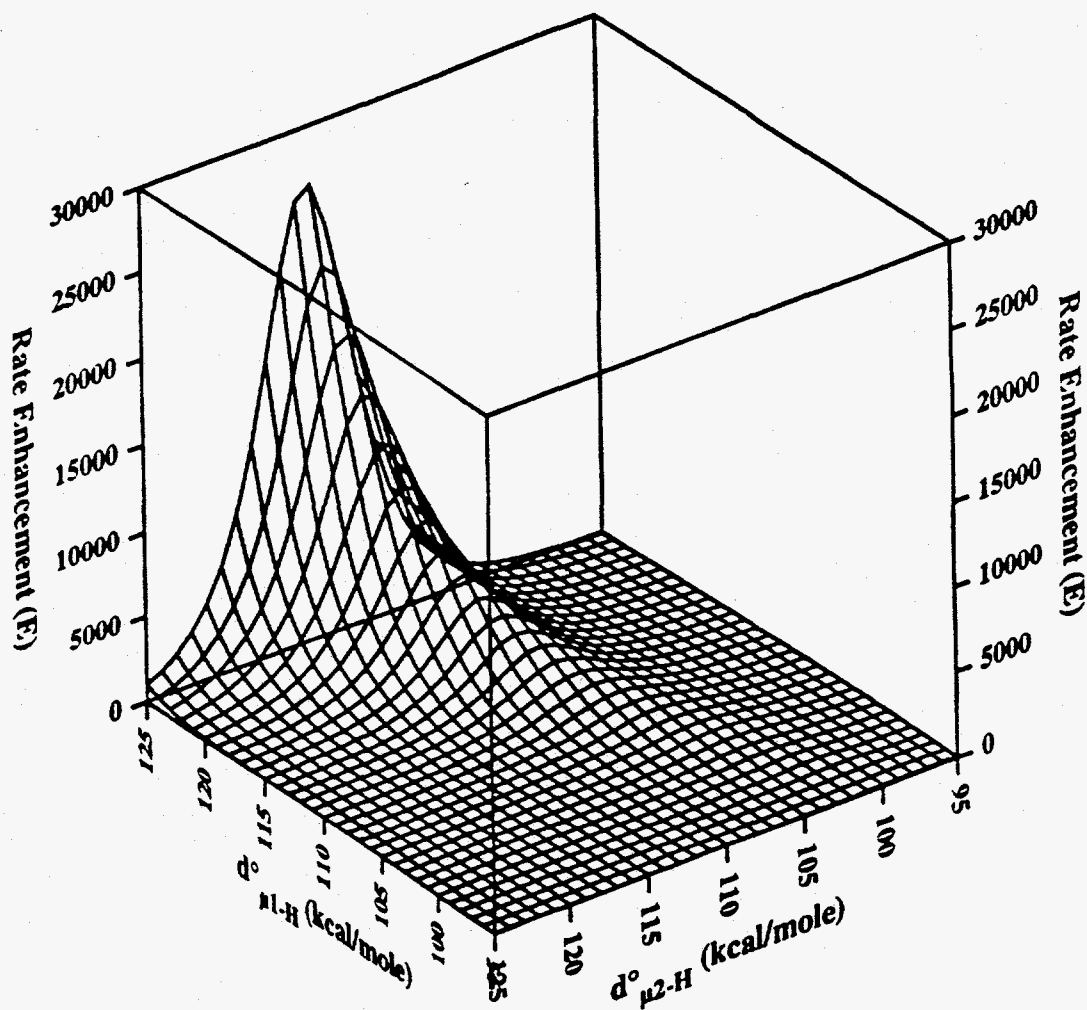
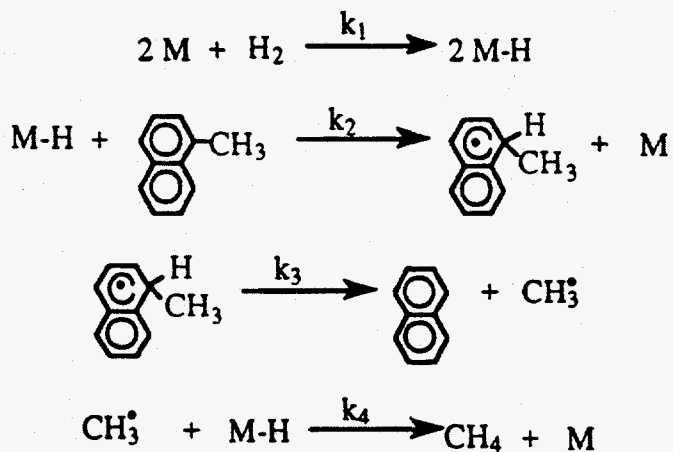


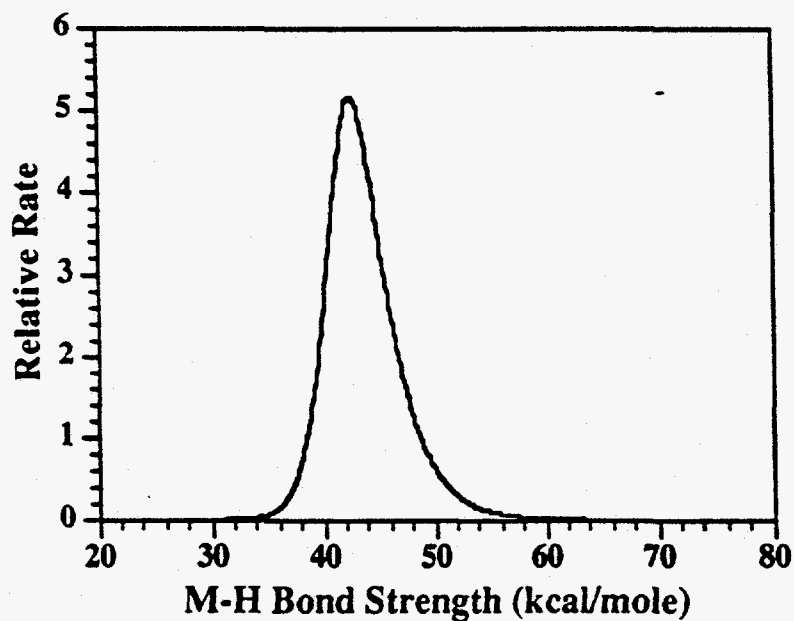
Figure 1.5 Effect of the presence of CS<sub>2</sub> on the reaction kinetics of dibenzylether at  $345^{\circ}\text{C}$  in an excess of tetralin.



**Figure 1.6** Rate enhancement ( $E$ ) depends on the structure of the reactant ( $d^{\circ}_{\mu 1-H}$ ) as well as the structure of the additive ( $d^{\circ}_{\mu 2-H}$ ). This surface assumes a benzyl radical chain carrier ( $d^{\circ}_{\mu 1-H} = 85.0$  kcal/mole) at a temperature of  $350^{\circ}\text{C}$ .



**Figure 1.7** Model mechanism for methylnaphthalene dealkylation over a metal catalyst (M).



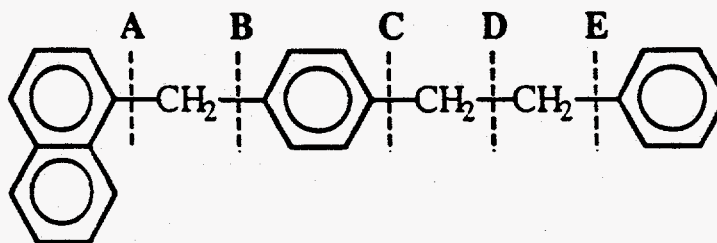
**Figure 1.8** Estimated methylnaphthalene rate due to the reaction scheme shown in Figure 1.7. A priori first estimates for the LFER parameters:  $\log_{10}A_1 = \log_{10}A_2 = 7.0$ ,  $\alpha_1 = \alpha_2 = 0.5$ ,  $E_1 = 11.0$  and  $E_2 = 16.0$ .



### 1.5.2 Model Compound Selection

The use of simple model systems that mimic important coal structure features enables the examination of specific reactivities. In addition, analysis of well defined hydrocarbon systems allows the focus to be placed on the catalyst and its role. Due to these advantages model compounds are useful in studying coal liquefaction catalysis.

The present report focuses on the model compound 4-(naphthylmethyl)-bibenzyl (NBBM) (Farcasiu and Smith, 1991), shown in Figure 1.9. NBBM is similar to coal in that it is a multifunctional, low-volatility material. Its structure mimics some of the important attributes of coal, e.g., a fused aromatic moiety connected to other aromatics by short alkyl chains. However, the structure is simple enough that the reaction products can be identified and the reactions occurring quantified. Since NBBM contains no alkyl chains of three units or more, we do not expect NBBM to decompose through a long-chain Rice-Herzfeld pathway and new reaction cycles must be created by the presence of a catalyst. Thus, NBBM is a good candidate for the application of the kinetics-assisted design formalism to specify the attributes of a catalyst which will be effective for coal liquefaction.



**Figure 1.9** The structure of the coal model compound 4-(1-naphthylmethyl)bibenzyl (NBBM). The scissile bonds are labeled A through E.

## 1.6 Summary

The presence of retrogressive reactions during coal liquefaction limit the rate and ultimate yield of coal liquefaction and motivate the use of a catalyst. Fine-particle metal catalysts have been shown to be effective due to their ability to access the coal pore structure as well as their ability to effect hydrogenolysis, hydrogenation and hydrogen-transfer within the coal structure. Moreover, model compound studies have aided in elucidation of the specific reactivities of catalysts with the functionalities found in coal and allow quantitative modeling of these reactions using LFERs to predict rate constants.

Knowledge-based, expert systems run on computers have been used to aid in the design of optimal formulations of heterogeneous catalysts. However, these models require extensive experimental databases and are limited by the experiments which have been performed. A mechanism-based catalyst design formalism has been developed for free-radical long chain reactions and provides a basis for heterogeneous catalyst design.

Quantitative kinetics can assist in the understanding and selection of coal liquefaction catalysts. Knowledge of a reactant's pyrolysis and catalysis mechanisms leads to, through the use of LFERs, an ability to predict properties of an optimal catalytic material. In order to carry out a kinetics-assisted design of an effective catalyst for direct coal liquefaction, the present research includes: (1) model compound selection and pyrolysis, (2) specification of initial catalytic materials and model compound tests, (3) assessment of the effectiveness for catalysis of different reaction families, (4) use of thermochemical and structure-function relationships to guide catalyst selection and (5) specification of properties of an optimal catalyst for coal liquefaction.

## REFERENCES

- Afifi, A.I., Hindermann, J.P., Chornet, E., Overend, R.P. (1989) "The Cleavage of the Aryl-O-CH<sub>3</sub> Bond Using Anisole as a Model Compound," *Fuel*, **68**, 498.
- Andrés, M., Charcosset, H., Chiche, P., Davignon, L., Djega-Mariadassou, G., Joly, J., Prégermain, S. (1983) "Catalysis of Coal Hydroliquefaction by Synthetic Iron Catalysts." *Fuel*, **62**, 69.
- Bockrath, B.C., Illig, E.G., Keller, M.J. (1992) "Catalysis of Low Temperature Liquefaction by Molybdenum Sulfides." *Prepr. Paper: Am. Chem. Soc., Div. Fuel Chem.*, **37**, 133.
- Burgess, C.E., Artok, L., Schobert, H.H. (1992) "Relationships of Coal Structure to Molybdenum Catalyst Action in Liquefaction." *Prepr. Paper: Am. Chem. Soc., Div. Fuel Chem.*, **37**, 200.
- Cook, P.S., Cashion, J.D. (1987) "Mössbauer Study of Iron Catalysts in Victorian Brown Coal Liquefaction." *Fuel*, **66**, 669.
- Cugini, A.V., Lett, R.G. (1989) "Coal/Oil Coprocessing Mechanism Studies," *Energy & Fuels*, **3**, 120.
- Curtis, C.W., Cahela, D.R. (1989) "Hydrodenitrogenation of Quinoline and Coal Using Precipitated Transition-Metal Sulfides." *Energy & Fuels*, **3**, 168.
- Dewar, M.J.S. (1969) *The Molecular Orbital Theory of Organic Chemistry*. (McGraw Hill, New York.)
- Dumesic, J., Milligan, B.A., Greppi, L.A., Balse, V.R., Sarnowski, K.T., Beall, C.E., Kataoka, T., Rudd, D.E., Trevino, A.A. (1987) "A Kinetic Modeling Approach to the Design of Catalysts: Formulation of a Catalyst Design Advisory Program." *Ind. Eng. Chem.*, **26**, 1399.
- Dunn, I.J. (1968) "Linear Free Energy Relations in Modeling Heterogeneous Catalytic Reactions." *J. Catal.*, **12**, 335.
- Evans, M.G., Polanyi, M. (1938) "Inertia and Driving Force of Chemical Reactions," *Trans. Faraday Soc.*, **34**, 11.
- Fake, D.M., Klein, M.T., LaMarca, C. (1994) "Enhancement of Coal Liquefaction Kinetics: Effect of a Multicomponent Mixture on the Attributes of an Optimal Chain-Transfer Solvent," *Energy & Fuels*, **6**, 1223.

- Farcasiu, M. (1986) "Reactions of Coals and Coal Liquids with a Liquid Superacid," *Fuel Processing Technology*, **14**, 161.
- Farcasiu, M., Smith, C. (1991) "Modeling Coal Liquefaction. 1. Decomposition of 4-(1-Naphthylmethyl)biphenyl Catalyzed by Carbon Black." *Energy & Fuels*, **5**, 83.
- Farcasiu, M., Eldredge, P.A., Petrosius, S.C. (1994a) "Complex Iron Catalytic Systems: Relative Catalytic Activity of Various Components," *Energy & Fuels*, **8**, 53.
- Farcasiu, M., Petrosius, S.C., Eldredge, P.A., Anderson, R.R., Ladner, E.P. (1994b) "Modeling Coal Liquefaction. 3. Catalytic Reactions of Polyfunctional Compounds," *Energy & Fuels*, **8**, 920.
- Given, P.H. (1960) "The Distribution of Hydrogen in Coals and its Relation to Coal Structure." *Fuel*, **39**, 147.
- Groot, C.K., de Beer, V.H.J., Prins, R., Stolarski, M., Niedzwiedz (1986) "Comparative Study of Alumina- and Carbon-Supported Catalysts for Hydrogenolysis and Hydrogenation of Model Compounds and Coal-Derived Liquids." *W.S., Ind. Eng. Chem. Prod. Res. Dev.*, **25**, 522.
- Guin, J., Zhan, X., Singh, R. (1993) "Activity and Selectivity of Dispersed Iron Catalysts in Coal Liquefaction and Model Compound Reactions," *Prepr. Paper: Am. Chem. Soc., Div. Fuel Chem.*, **38**, 86.
- Hattori, H., Matsushashi, H., Kimura, A., Tanabe, K. (1985) "Catalytic Functions of Iron Catalysts for Hydrocracking of C-C and C-O Bonds," *Proceedings: International Conference on Coal Science*, 165.
- Hei, R.D., Sweeny, P.G., Stenberg, V.I. (1986) "Mechanism of the Hydrogen-Sulfide-Promoted Cleavage of the Coal Model Compounds: Diphenyl Ether, Diphenylmethane and Biphenyl," *Fuel*, **65**, 577.
- Herrick, D.E., Tierney, J.W., Wender, I., Huffman, G.P., Huggins, F.E. (1990) "Activity and Characterization of Coprocessing Catalysts Produced from an Iron Pentacarbonyl Precursor," *Energy & Fuels*, **4**, 231.
- Hirschon, A.S., Laine, R.M. (1989) "Catalytic Hydrodenitrogenation of an SRC-II Coal Liquid: Effect of Nucleophiles and Acids," *Fuel*, **68**, 1416.
- Hu, X.-D., Foley, H.C., Stiles, A.B. (1991) "Design of Alcohol Synthesis Catalysts Assisted by a Knowledge-Based Expert System," *Ind. Eng. Chem. Res.*, **30**, 1419.

- Huffman, G.P., Ganguly, B., Zhao, J., Rao, K.R.P.M., Shah, N., Feng, Z., Huggins, F.E., Taghiei, M.M., Lu, F., Wender, I., Pradhan, V.R., Tierney, J.W., Seehra, M.S., Ibrahim, M.M., Shabtai, J., Eyring, E.M. (1993) "Structure and Dispersion of Iron-Based Catalysts for Direct Coal Liquefaction." *Energy & Fuels*, **7**, 285.
- Ikenaga, N., Kobayashi, Y., Saeki, S., Sakota, T., Watanabe, Y., Yamada, H., Suzuki, T. (1994) "Hydrogen-Transfer Reactions of Coal Model Compounds in Tetralin with Dispersed Catalysts." *Energy & Fuels*, **8**, 947.
- LaMarca, C., Libanati, C., Klein, M.T. (1990) "Design of Kinetically Coupled Complex Reaction Systems." *Chem. Eng. Sci.*, **45**, 2059.
- LaMarca, C. (1992) *Kinetic Coupling in Multicomponent Pyrolysis Systems*. (Ph.D. Dissertation, University of Delaware.)
- LaMarca, C., Libanati, C., Klein, M.T., Cronauer, D.C. (1993) "Enhancing Chain Transfer during Coal Liquefaction: A Model System Analysis." *Energy & Fuels*, **7**, 473.
- Lambert, J.M. (1982) "Alternative Interpretation of Coal Liquefaction Catalysis by Pyrite." *Fuel*, **61**, 777.
- Landau, R.N., Korré, S.C., Neurock, M., Klein, M.T., Quann, R.J. (1992) "Hydrocracking of Heavy Oils: Development of Structure/Reactivity Correlations for Kinetics." *Prepr. Paper: Am. Chem. Soc., Div. Fuel Chem.*, **37**, 1871.
- Larsen, J.W., Lee, D. (1983) "Reactions of Coal in Acidic Phenol. Model Compound Studies." *Fuel*, **62**, 463.
- Lemberton, J.L., Touzeyidio, M., Guismet, M. (1989) "Catalytic Hydroprocessing of Simulated Coal Tars II. Effect of Acid Catalysts on the Hydroconversion of Model Compounds on a Sulphided Ni-Mo/Al<sub>2</sub>O<sub>3</sub> Catalyst." *Appl., Catal.*, **54**, 101.
- Linehan, J.C., Darab, J.G., Matson, D.W. (1993) "Results of Catalyst Testing Using Iron-based Catalysts." *Prepr. Paper: Am. Chem. Soc., Div. Fuel Chem.*, **38**, 66.
- Linehan, J.C., Matson, D.W., Darab, J.G. (1994) "Effects of Iron-Oxygen Precursor Phase on Carbon-Carbon Bond Scission in Benzyl(naphthylbenzyl)methane." *Energy & Fuels*, **8**, 56.
- Lowry, T.H., Richardson, K.S. (1987) *Mechanism and Theory in Organic Chemistry*, 3rd ed. (Harper & Row, New York.)
- Matsumoto, H., Take, J., Yoneda, Y. (1968) "Linear Free Energy Relationships in Heterogeneous Catalysis VIII. Isomerization of Alkylbenzenes over Solid Acid Catalysts." *J. Catal.*, **11**, 211.

- McCormick, R.L., Haynes, H.W., Netzel, D.A. (1989) "Effect of Catalyst Acidity on the Hydrogen-Donor Content of a Hydrotreated Coal Liquid." *Ind. Eng. Chem. Res.*, **28**, 1156.
- McMillen, D.F., Malhotra, R., Chang, S., Ogier, W.C., Nigenda, S.E., Fleming, R.H. (1987a) "Mechanisms of Hydrogen Transfer and Bond Scission of Strongly Bonded Coal Structures in Donor-Solvent Systems." *Fuel*, **66**, 1611.
- McMillen, D.F., Malhotra, R., Hum, G.P., Chang, S. (1987b) "Hydrogen-Transfer-Promoted Bond Scission Initiated by Coal Fragments." *Energy & Fuels*, **7**, 193.
- McMillen, D.F., Malhotra, R., Tse, D.S., St. John, G.A. (1989) "Relative Importance of Thermolysis and Hydrogenolysis Processes: 'Liquefaction' of a Bibenzyl Polymer." *Energy & Fuels*, **4**, 465.
- McMillen, D.F., Malhotra, R. (1990) "A Mechanistic Numerical Model for Coal Liquefaction Involving Hydrogenolysis of Strong Bonds. Rationalization of Interactive Effects of Solvent Aromaticity and Hydrogen Pressure." *Energy & Fuels*, **4**, 184.
- McMillen, D.F., Malhotra, R. (1992) "Hydrogen-Transfer in Retrograde Reaction -- The Hero and the Villain." *Prepr. Paper: Am. Chem. Soc., Div. Fuel Chem.*, **37**, 385.
- Mochida, I., Yoneda, Y. (1967) "Linear Free Energy Relationships in Heterogeneous Catalysis. V. An Application of Quantum Chemical Reactivity Indexes to Heterogeneous Catalysis." *J. Catal.*, **9**, 57.
- Neurock, M., Klein, M.T. (1993) "When You Can't Measure - Model." *Chemtech*, September, 26.
- Olah, G.A., Bruce, M.R., Edelson, E.H., Husain, A. (1984a) "Superacid Coal Chemistry. 1. HF:BF<sub>3</sub> Catalyzed Depolymerization - Ionic Hydroliquefaction of Coals Under Milder Conditions." *Fuel*, **63**, 1130.
- Olah, G.A., Husain, A. (1984b) "Superacid Coal Chemistry. 2. Model Compound Studies under Conditions of HF:BF<sub>3</sub>:H<sub>2</sub> Catalyzed Mild Coal Liquefaction." *Fuel*, **63**, 1427.
- Ouchi, K., Imuta, K., Yamashita, Y. (1973) "Catalysts for the Depolymerization of Mature Coals." *Fuel*, **52**, 156.
- Patzer, J.F., Farrauto, R.J., Montagna, A.A. (1979) "Characterization of Coal Liquefaction Catalysts Using 1-Methylnaphthalene as a Model Compound." *Ind. Eng. Chem. Proc. Des. Dev.*, **18**, 625.
- Poutsma, M.L. (1987) *A Review of Thermolysis Studies of Model Compounds Relevant to Processing of Coal*, Report ORNL/TM-10637.

- Poutsma, M.L. (1990) "Free-Radical Thermolysis and Hydrogenolysis of Model Hydrocarbons Relevant to Processing of Coal," *Energy & Fuels*, 4, 113.
- Pradhan, V.R., Tierney, J.W., Wender, I. (1991) "Catalysis in Direct Coal Liquefaction by Sulfated Metal Oxides," *Energy & Fuels*, 5, 497.
- Pradhan, V.R., Holder, G.D., Wender, I., Tierney, J.W. (1992) "Kinetic Modeling of Direct Liquefaction of Wyodak Coal Catalyzed by Sulfated Iron Oxides," *Ind. Eng. Chem. Res.*, 31, 2051.
- Prégermain, S. (1985) "Disposable Catalysts in One-Stage Coal Liquefaction." *Proceedings: International Conference on Coal Science*, 189.
- Provine, W.D., Porro, N.D., LaMarca, C., Klein, M.T., Foley, H.C., Bischoff, K.B., Scouten, C.G., Cronauer, D.C., Tait, A.M. (1992a) "Development of a Pulse-Injection Short Contact Time Coal Liquefaction Flow Reactor," *Ind. Eng. Chem. Res.*, 31, 1170.
- Provine, W.D. (1992b) *An Initial Reaction Pathway Analysis of Thermal Direct Coal Liquefaction*. (Ph.D. Dissertation, University of Delaware.)
- Rahimi, P.M., Fouda, S.A., Kelly, J.F. (1987) "Coproprocessing Using H<sub>2</sub>S as a Promoter," *Fuel*, 66, 1215.
- Rebick, C. (1980) *Frontiers of Free Radical Chemistry*, ed. (William A. Pryor ed., Academic Press.)
- Shinn, J.H. (1984) "From Coal to Single-Stage and Two-Stage Products: A Reactive Model of Coal Structure," *Fuel*, 63, 1187.
- Stein, S.E. (1981) *New Approaches in Coal Chemistry*. (Based on a symposium sponsored by the Pittsburgh Section of the American Chemical Society at the 12th central regional meeting, Pittsburgh, PA, November 12-14, 1980.)
- Suzuki, T., Yamada, H., Sears, P.L., Watanabe, Y. (1989) "Hydrogenation and Hydrogenolysis of Coal Model Compounds by Using Finely Dispersed Catalysts," *Energy & Fuels*, 3, 707.
- Swanson, A.J. (1992) "Dispersed Molybdenum Catalysts for Liquefaction of Illinois No. 6 Coal," *Prepr. Paper: Am. Chem. Soc., Div. Fuel Chem.*, 37, 149.
- Takemura, Y., Shibaoka, M., Yamada, T. (1985) "Behavior of Iron Catalysts During Coal Hydrogenation," *Proceedings: International Conference on Coal Science*, 185.
- Tang, Y., Curtis, C.W. (1994) "Activity and Selectivity of Slurry-Phase Iron-Based Catalysts for Model Systems," *Energy & Fuels*, 8, 63.

- Wiser, W. (1975) "Batch Autoclave Hydrogenation of Solvent Refined Lignite." *Prepr. Paper: Am. Chem. Soc., Div. Fuel Chem.*, **20**, 122.
- Watanabe, Y., Yamada, O., Fujita, K., Takegami, Y., Suzuki, T. (1984) "Coal Liquefaction Using Iron Complexes as Catalysts." *Fuel*, **63**, 752.
- Yamashita, H., Ohtsuka, Y., Yoshida, S., Tomita, A. (1989) "Local Structures of Metals Dispersed on Coal. 1. Change of Local Structure of Iron Species on Brown Coal during Heat Treatment." *Energy & Fuels*, **3**, 686.
- Yoneda, Y. (1967) "Linear Free Energy Relationships in Heterogeneous Catalysis. IV. Regional Analysis for Solid Acid Catalysis." *J. Catal.*, **9**, 51.
- Zhan, X., Guin, J.A. (1994a) "High-Pressure Hydrogenation of Naphthalene Using a Reduced Iron Catalyst." *Energy & Fuels*, **8**, 1384.
- Zhang, Z.-G., Scott, D.S., Silveston, P.L. (1994b) "Successive Pulsing of an Iron-Loaded Canadian Subbituminous Coal Char." *Energy & Fuels*, **8**, 943.



## Chapter 2

### PYROLYSIS OF 4-(1-NAPHTHYLMETHYL)BIBENZYL

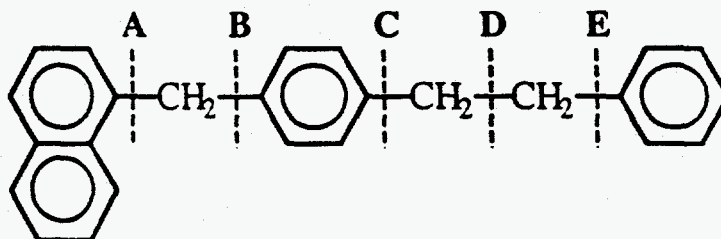
Model compound reactions can be an effective probe of related reactions during the upgrading of complex feedstocks, such as coal. The use of simple mimics of important coal structure features enables the examination of specific reactivities and elementary steps without the complications attendant in a complex mixture. Model compound results thus provide mechanistic insight and quantitative kinetic parameters for elementary steps of fundamental value. That is, the kinetics of elementary steps are independent of the source of a feed stock and can thus be used to model essentially any complex system.

Catalytic upgrading strategies provide an additional motivation for the study of pyrolysis. Application of the kinetics-assisted catalyst design formalism for coal liquefaction requires a firm understanding of the thermal background reactions. Fortunately, the Rice-Herzfeld kinetics formalism summarizes the likely mechanism for reaction neat and in the presence of a hydrogen donor additive. The Rice-Herzfeld elementary steps of bond fission, hydrogen abstraction,  $\beta$ -scission and radical recombination, as well as the extra steps of radical hydrogen transfer and radical addition, organize the kinetics of hydrocarbon pure compounds well.

## 2.1 Pyrolysis of 4-(Naphthylmethyl)bibenzyl

A useful coal model compound must be similar to coal in structure and, as a result, display its important reactivities. The coal macromolecule has a predominantly hydrocarbon composition. Its structure consists mainly of aromatic and hydroaromatic clusters connected by relatively short alkyl chains.

4-(naphthylmethyl)-bibenzyl (NBBM) possesses these desired features. NBBM, shown in Figure 2.1, is similar to coal in that it is a multifunctional, low-volatility material. Its structure mimics some of the important attributes of coal, e.g., a fused aromatic moiety connected to other aromatics by short alkyl chains. However, the structure is simple enough that the reaction products can be identified and the reactions occurring quantified.



**Figure 2.1** The structure of the coal model compound 4-(1-naphthylmethyl)-bibenzyl (NBBM). The scissile bonds are labeled A through E.

The thermal and catalytic reactivity of NBBM have been initially characterized by Farcasiu and Smith (1991). Furthermore, several studies have shown that the reaction of NBBM in the presence of hydrogen donor solvents and catalytic reaction of NBBM with iron-based catalysts correlate directly to coal liquefaction

results in analogous systems (Farcasiu and Smith, 1991; Linehan et al., 1993; and Guin et al., 1993). This correlation implies that the reactions which control destruction of NBBM are similar to those which are important during coal liquefaction.

The pyrolysis of NBBM was carried out at 420 °C in both nitrogen and hydrogen atmospheres to assess the effect of molecular hydrogen on NBBM reaction. Additional NBBM hydrolysis reactions were carried out at 420 °C at long times to observe the full range of NBBM conversion. This data revealed the important secondary reactions occurring in the NBBM hydrolysis system. In addition to the need for an in depth understanding of NBBM reaction families, NBBM pyrolysis will also be used as the thermal background for catalytic reactions. The thermal background will provide a baseline to which the effects of different catalytic materials on NBBM reaction will be compared. However, since the focus of the catalytic reactions will be on the action of the catalyst, these reactions should be performed under conditions which minimize the effects of thermal reaction. To accomplish this goal, the catalytic reactions will be performed at a temperature lower than the 420 °C employed for studying NBBM pyrolysis. A temperature of 400 °C has been identified as a condition at which the characteristic time for thermal reaction of NBBM is much larger than that for catalytic reaction of NBBM with the materials that will be employed.

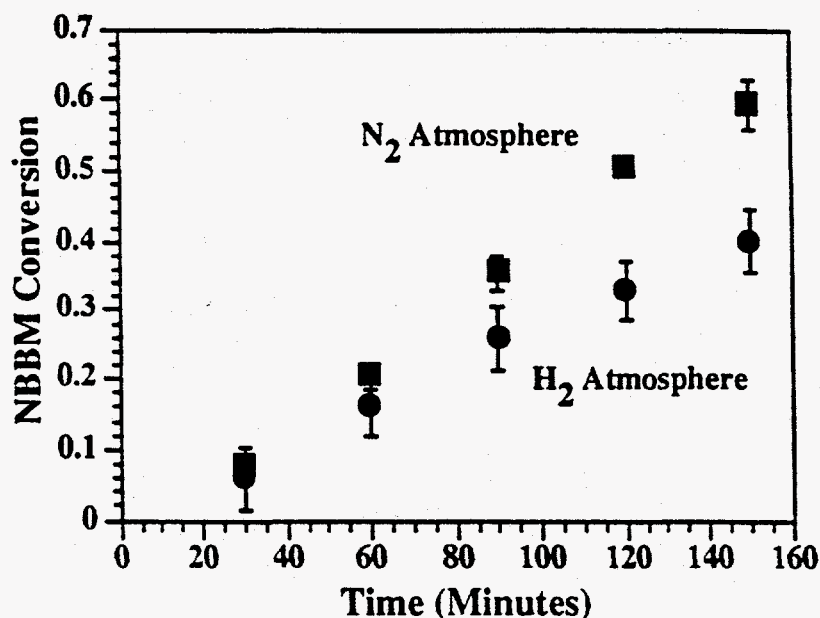
### **2.1.1 Experimental Method - NBBM Reactions**

NBBM (TCI Americas), dichloromethane (Fisher Scientific) and all other chemicals (Aldrich Chemical Company) were used as received. The reactions were carried out in 7 ml stainless steel microbatch reactors. The reactant was placed in an open 10 x 75 mm glass tube, which was in turn placed within the reactor. This

minimized interaction with the reactor wall. In general, the loading of NBBM was 50 mg, and all reactions took place under 1000 psig (cold) pressure. However, for the long time NBBM hydrolysis reactions at 420 °C the loading was increased to 100 mg to minimize the effect of material loss. The reactor was pressurized to 1000 psig with either nitrogen or hydrogen and then discharged three times prior to heat up. This ensured reaction in the absence of air. The reactor was then plunged into a fluidized sand bath at either 400 °C or 420 °C and, after the passage of the reaction time, removed from the sandbath for cooling in an ice bath for a minimum of 30 minutes. A known amount of biphenyl was then added to the contents of the glass tube, which was subsequently diluted with dichloromethane. The mixture was then separated and quantified in a Hewlett-Packard 5890 Gas Chromatograph with Flame Ionization Detector and a Hewlett-Packard 5890 Gas Chromatograph with a Hewlett-Packard 5970 Mass Selective Detector. Both Gas Chromatographs used Hewlett-Packard Ultra 2 columns (crosslinked 5% Ph Me Silicone) with dimensions 50 m x 0.2 mm and 0.33  $\mu\text{m}$  film thickness.

### 2.1.2 NBBM Pyrolysis Results

The kinetics of NBBM disappearance in either hydrogen or nitrogen at 420 °C are shown in Figure 2.2. Reaction under hydrogen showed an inhibited rate relative to reaction under nitrogen. This suggests capping by  $\text{H}_2$  or hydroaromatics of the active centers in a free radical reaction pathway, preventing further attack on the reactant molecules.



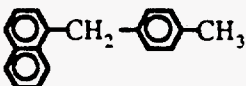
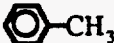
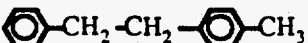

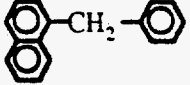
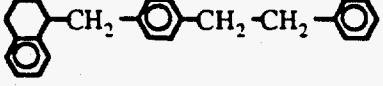
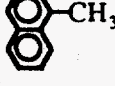

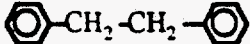



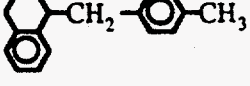
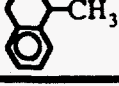
**Figure 2.2** Disappearance kinetics for NBBM pyrolysis at 420 °C under a pressure of 1000 psig (cold) of either hydrogen or nitrogen. Error bars are two standard deviations in each direction as calculated from repeated measurements.

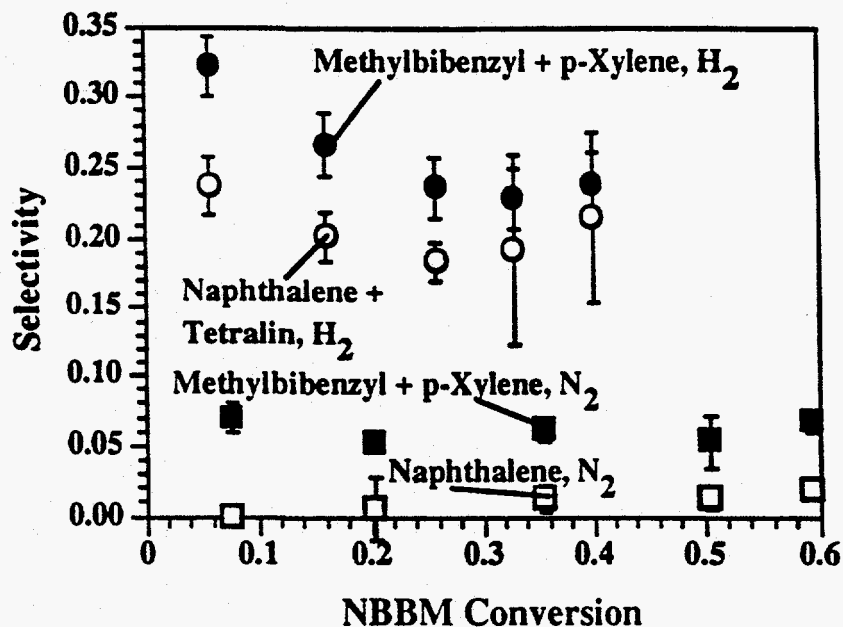
The observed products of NBBM pyrolysis and their structures are listed in Table 2.1. These products can be organized into "lumps" associated with the net NBBM bond breaking action required for its formation. For example, toluene and naphthyltolylmethane are classified as bond D scission products. For hydrolysis, the hydrogenation product tetrahydronaphthyltolylmethane is also included in bond D scission products lump. Similarly, naphthalene (and its hydrogenation product tetralin) and methylbibenzyl and its fission product p-xylene are considered bond A scission products. Methylnaphthalene and its hydrogenation product methyltetralin and bibenzyl are bond B scission products, whereas ethylbenzene is a bond C scission product. Benzene is a bond D scission product. Naphthylphenylmethane is a special case to be discussed in the ensuing analysis.

The major products, toluene and naphthyltolylmethane, were derived from the thermolysis of bond D. This is the weakest bond in the molecule, which suggests a free radical view of NBBM pyrolysis. The products associated with the breaking of bond A, naphthalene and methylbibenzyl, and methylbibenzyl's derivative, p-xylene, were observed to a lesser extent.

The selectivities to the products associated with cleavage of bond A are shown as a function of NBBM conversion in Figure 2.3. Products with positive finite intercepts are primary products, and species with zero intercepts are secondary or higher-rank products (Bhore et al., 1990a, 1990b). Figure 2.3 shows that pyrolysis under nitrogen led to methylbibenzyl as a primary product and naphthalene as a higher-rank product. This suggests that the formation of methylbibenzyl is not from the direct fission of bond A, but through some other pathway. However, in the presence of hydrogen, the selectivity versus conversion curves for the bond A products (including tetralin from naphthalene hydrogenation) both have positive finite intercepts; and they converge at higher conversions. Thus, in the presence of hydrogen, the bond A cleavage products were both primary. This trend suggests that the presence of hydrogen in the reaction mixture opens a new pathway for the breaking of bond A to form naphthalene and methylbibenzyl.

**Table 2.1** Summary of reaction products from NBBM hydrolysis at 420 °C.

Reaction Products from NBBM Hydrolysis (420 °C)	
Major Products	
Naphthyltolylmethane	
Toluene	
Methylbibenzyl	
Naphthaléne	
Minor Products	
Naphthylphenylmethane	
Tetrahydro-NBBM	
Methylnaphthalene	
Tetralin	
Bibenzyl	
Benzene	
Ethylbenzene	
p-Xylene	
Tetrahydronaphthyltolylmethane	
Methyltetralin	

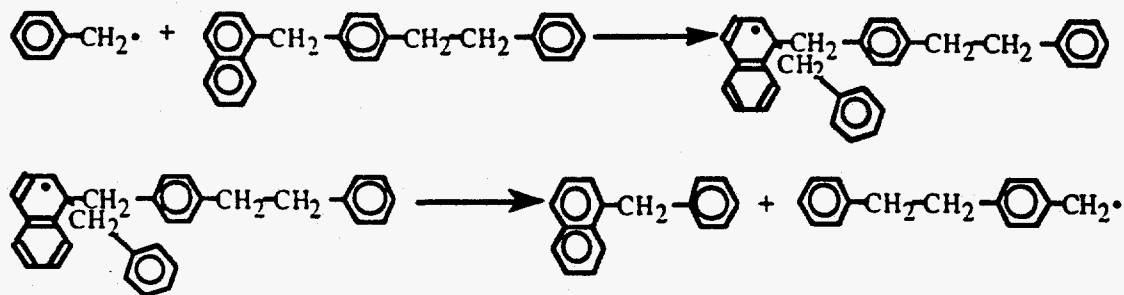


**Figure 2.3** Selectivity versus reactant conversion plot for NBBM Bond A scission products. Products with positive finite intercepts are primary and products with zero intercepts are of higher rank. Error bars are two standard deviations in each direction as calculated from repeated measurements.

The fate of the naphthalene function from bond A scission in a nitrogen atmosphere is still unclear. To this end, it is informative to note that only one of the expected products from the breaking of bond C, naphthylphenylmethane, was observed. The other expected product, ethyl benzene, was not. This suggests that the reaction mixture contained a radical that in some way was involved in the breaking of bond A such that methylbibenzyl but not naphthalene would form. A radical ipso-substitution scheme for the breaking of bond A is thus quite likely. The formation of a benzyl radical by thermolysis at the weak bond D could initiate such a scheme. Subsequently, benzyl radical attack on an NBBM molecule by substitution at the ipso position of the naphthalene ring would yield an intermediate radical which, upon

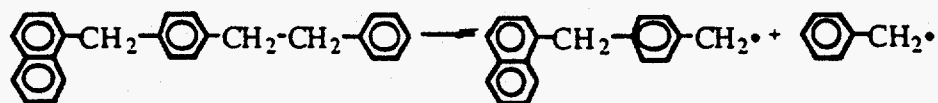
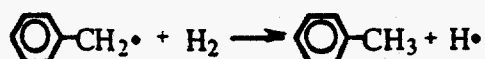
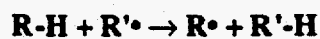
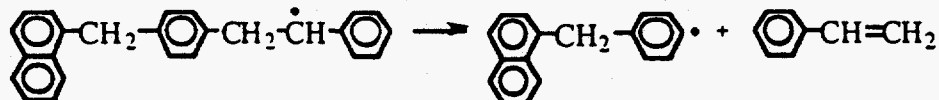
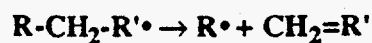
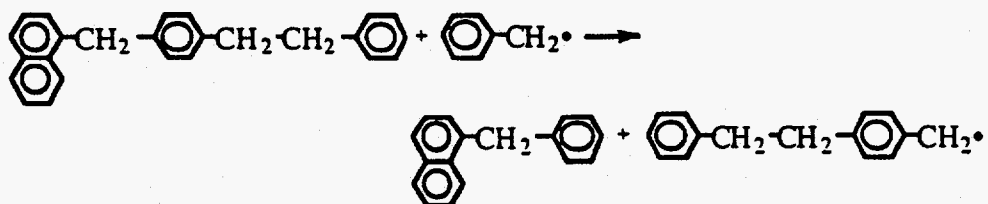
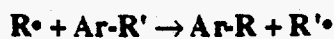
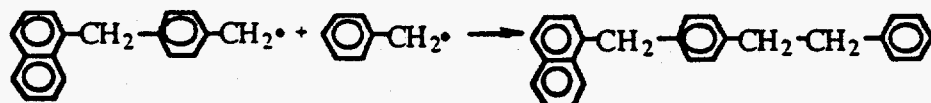
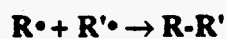


undergoing  $\beta$ -scission, would release a methylbibenzyl radical and afford naphthylphenylmethane. This is illustrated in Figure 2.4. Note that ethylbenzene would not be formed in this scheme, and the direct "bond C" cleavage could thus still be a minor reaction.

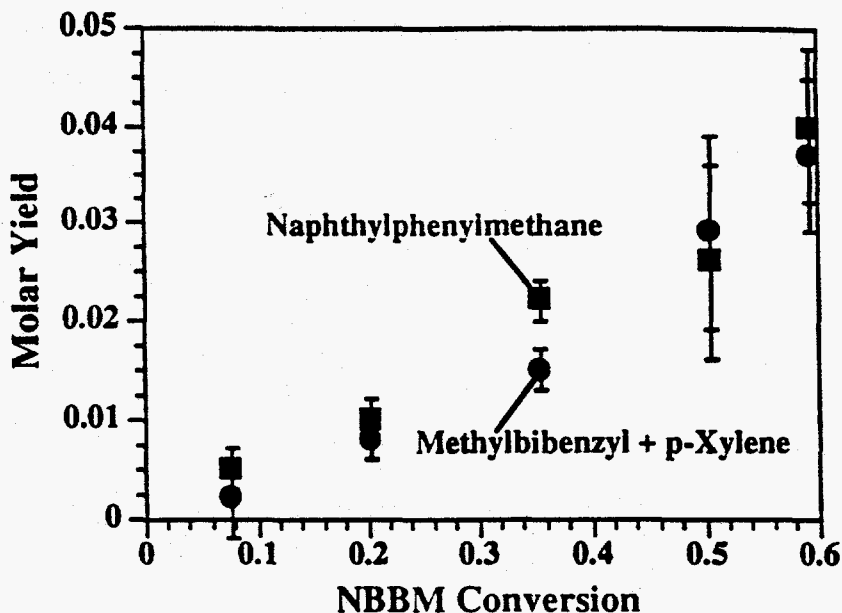


**Figure 2.4** Representative radical ipso-substitution pathway for cleavage of bond A by a benzyl radical.

The overall pyrolysis chemistry can thus be represented in terms of five reaction families: bond thermolysis, hydrogen abstraction, radical ipso-substitution,  $\beta$ -scission and radical recombination. General representations for these reaction families, as well as specific important examples from the NBBM system, are shown in Figure 2.5.

**Bond Thermolysis****Hydrogen Abstraction** **$\beta$ -Scission****Radical Ipso-Substitution****Radical Recombination**

**Figure 2.5** Proposed mechanism for the pyrolysis of NBBM through radical pathways.

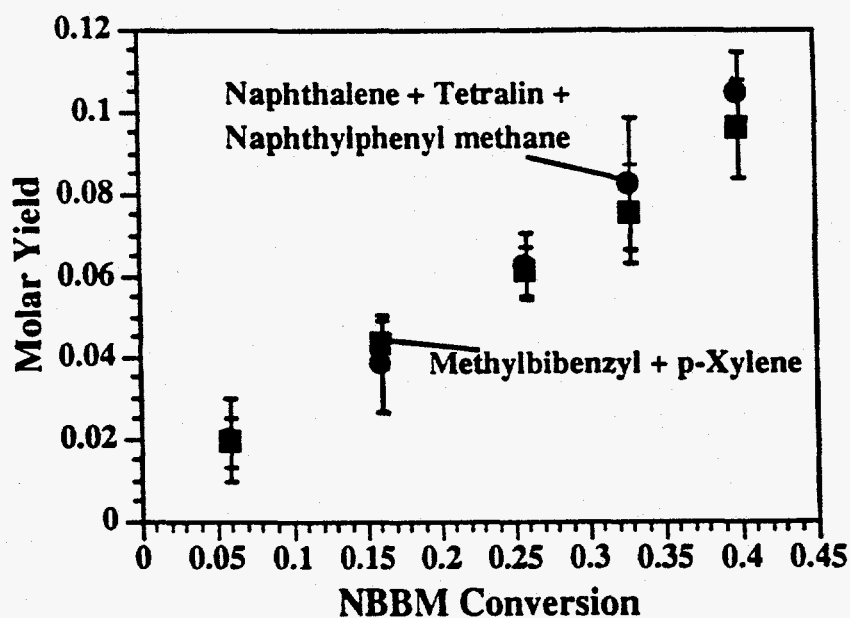


**Figure 2.6** Plot of molar yields versus reactant conversion of NBBM Bond A products for pyrolysis under nitrogen. The stoichiometry is consistent with the benzyl radical attack mechanism.

This proposed reaction scheme reproduces the observed stoichiometry of NBBM pyrolysis. For example, ipso-substitution of a benzyl radical at the naphthalene ring of NBBM with subsequent ejection of a methylbibenzyl radical would effect bond A scission with the observable products as naphthylphenylmethane and methylbibenzyl. As shown in Figure 2.6, the summed molar yield of methylbibenzyl plus its derivative, p-xylene, was identical, within experimental error, to the molar yield of naphthylphenylmethane, thus supporting the notion of a radical ipso-substitution scheme.

The addition of hydrogen gas to the reaction mixture would provide, for the most energetic of the NBBM derived radicals, an additional pathway for hydrogen abstraction. This could cap the energetic NBBM-derived radicals and lead to a free H• radical. The H• radical could in turn either abstract another hydrogen, to regenerate

$H_2$ , or ipso-substitute at one of the aromatic systems present in the NBBM molecule or its products. These alternatives explain the primary stoichiometric formation of naphthalene and methylbibenzyl for pyrolysis under hydrogen at high conversions; naphthalene was a secondary product for reaction in nitrogen. These  $H\cdot$  mediated pathways are also consistent with the observed stoichiometry for bond A products. As shown in Figure 2.7, the summed molar yield for methylbibenzyl plus its derivative, p-xylene, was identical, within experimental error, to the molar yield of naphthylphenyl methane and naphthalene plus its hydrogenation product, tetralin.



**Figure 2.7** Plot of molar yields versus reactant conversion of NBBM Bond A products for pyrolysis under hydrogen. The stoichiometry is consistent with the benzyl radical and hydrogen radical attack mechanisms.

## 2.2 Thermal Background for Catalysis

NBBM pyrolysis reactions at 400 °C under a hydrogen atmosphere established a thermal background for catalytic reactions. Figure 2.8 shows the conversion versus time behavior of NBBM under these conditions. The conversion was less than 20% over the time range examined, suggesting that thermal reactions will be a small interference in the study of catalytic chemistry.

The reaction network at 400 °C was the same as that for 420 °C. Figure 2.9 summarizes the selectivity versus conversion behavior for the products resulting from the scission of bond A (naphthalene, tetralin, naphthylphenyl methane, methylbibenzyl, and p-xylene). This shows that products from bond A scission were primary, and that they accounted for approximately one quarter to one third of the NBBM disappearance. In addition, products that could be attributed to bond B scission (methylnaphthalene and bibenzyl), bond D scission (naphthyltolylmethane and toluene) and NBBM hydrogenation (tetrahydro-NBBM) were observed. Figure 2.10 shows the relative contributions of these product classes.

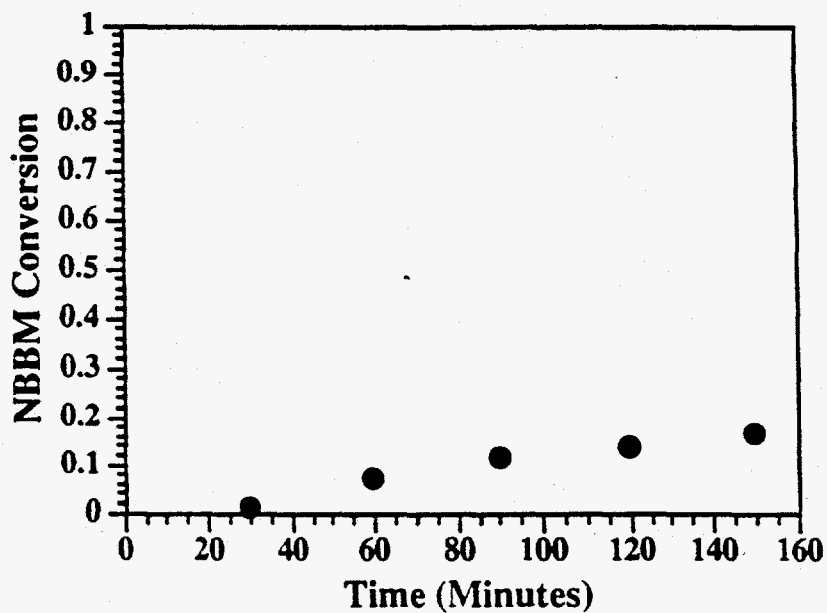


Figure 2.8 Disappearance with time of NBBM at 400 °C under a hydrogen atmosphere.

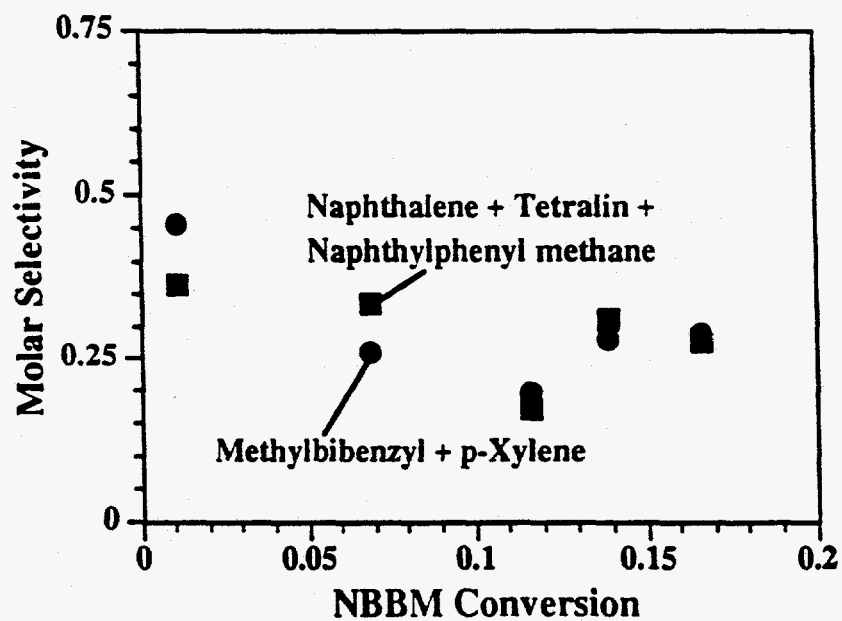


Figure 2.9 Selectivity versus conversion for bond A scission products at 400 °C.

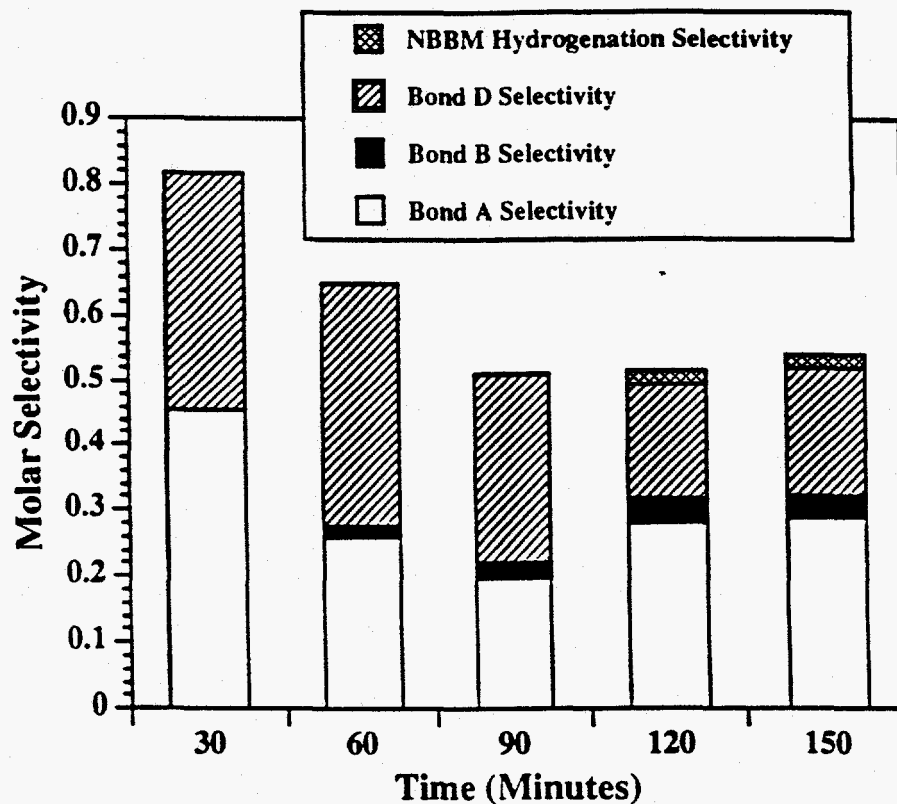


Figure 2.10 Product classes observed for NBBM pyrolysis at 400 °C under hydrogen.

### 2.3 Long Reaction Time NBBM Pyrolysis Data

NBBM pyrolysis kinetic data spanning the full range of NBBM conversion allows elucidation of the important secondary reaction paths. To this end, a series of NBBM hydrolysis reactions was performed at 420 °C spanning longer reaction times so that the full range of NBBM conversion was achieved.

The disappearance kinetics for this set of reactions are shown in Figure 2.11. NBBM conversions ranging from zero to 80% conversion were observed. The operative reaction paths were formal scission of bond A, bond B and bond D and NBBM hydrogenation. The relative selectivities of each of these major product

families are summarized in Figure 2.12. Figures 2.13-2.15 detail the observed stoichiometry for each product lump. Figure 2.13 shows that the sum of the naphthyl containing products derived from bond A scission (naphthalene, tetralin and naphthylphenyl methane) had consistently higher molar yields than did the methylbibenzyl derived products (methylbibenzyl and p-xylene). This suggests that the methylbibenzyl derived products were consumed by secondary reactions. Figure 2.14 shows good stoichiometric balance between the naphthyl containing products derived from bond B scission (methylnaphthalene and methyltetralin) and bibenzyl. Moreover, Figure 2.15 shows that, at higher conversions, the molar yield of naphthyl-containing products derived from bond D scission (naphthyltolyl methane and tetrahydronaphthyltolyl methane) leveled off, while the molar yield of toluene continues to rise. This suggests that the naphthyl containing products were consumed by secondary reactions, while toluene was not.

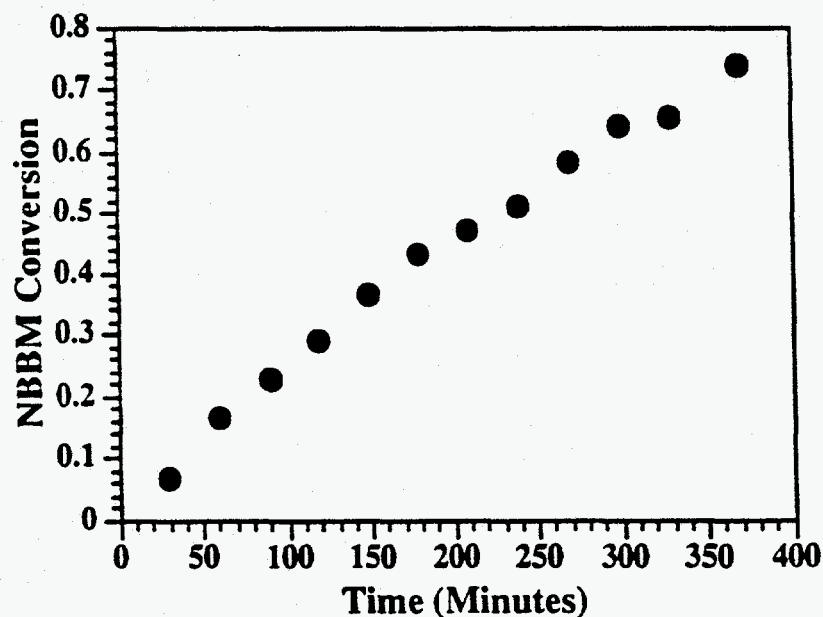
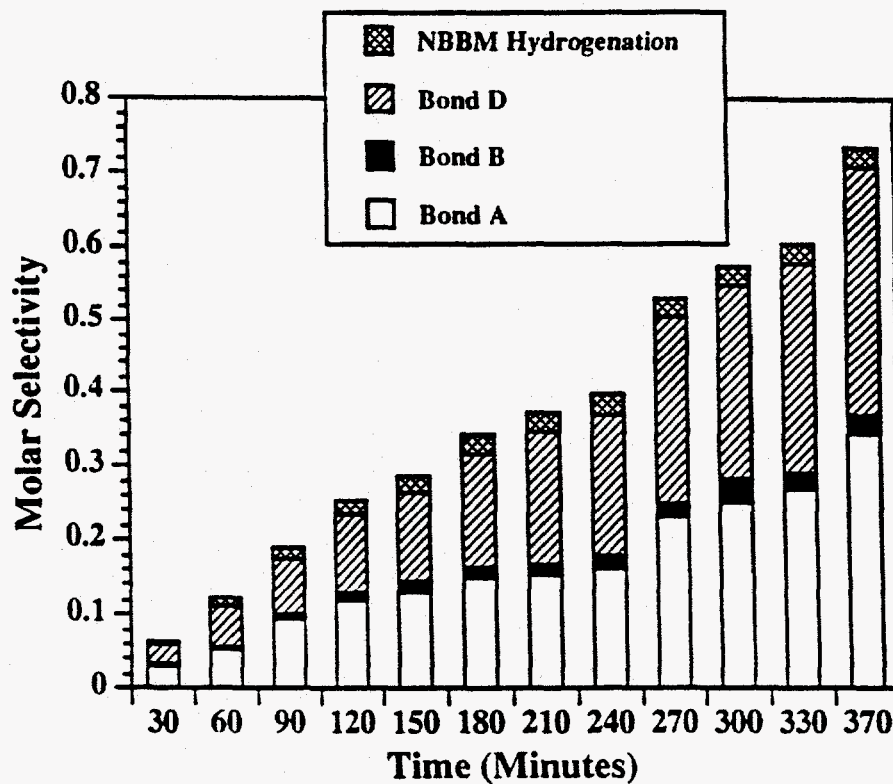


Figure 2.11 Disappearance kinetics for NBBM hydrolysis at 420 °C.





**Figure 2.12** Contributions of the major product families (bond A scission, bond B scission, bond D scission and NBBM hydrogenation) for NBBM hydropyrolysis at 420 °C.

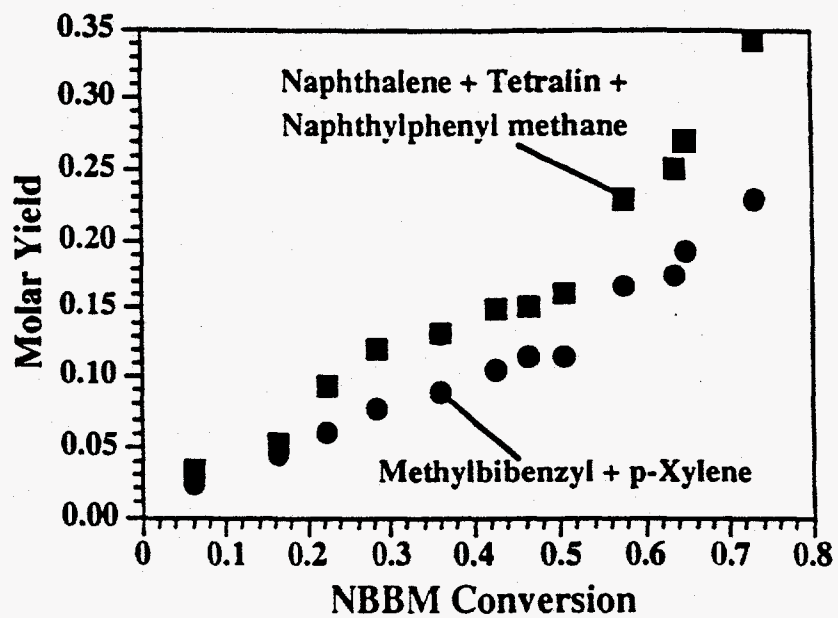


Figure 2.13 Bond A scission products for NBBM hydrolysis at 420 °C.

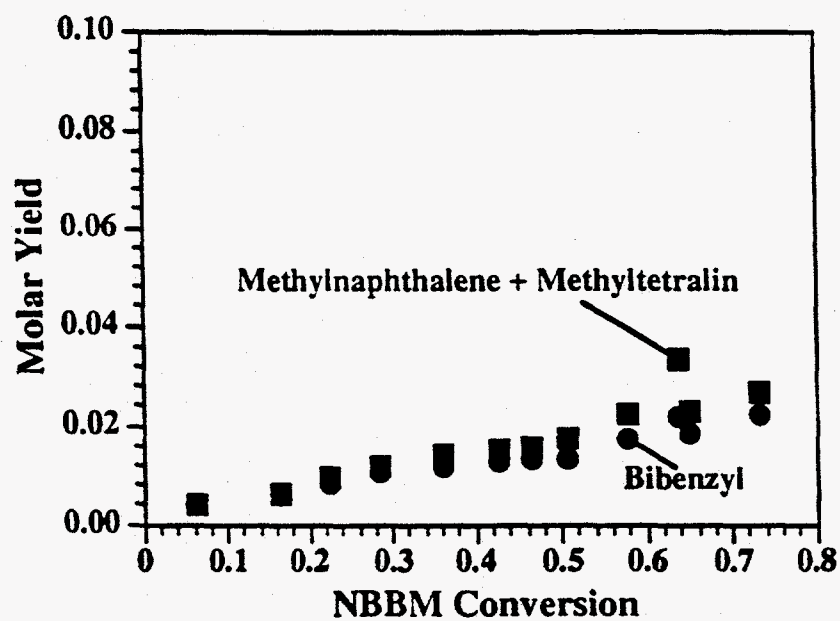


Figure 2.14 Bond B scission products for NBBM hydrolysis at 420 °C.

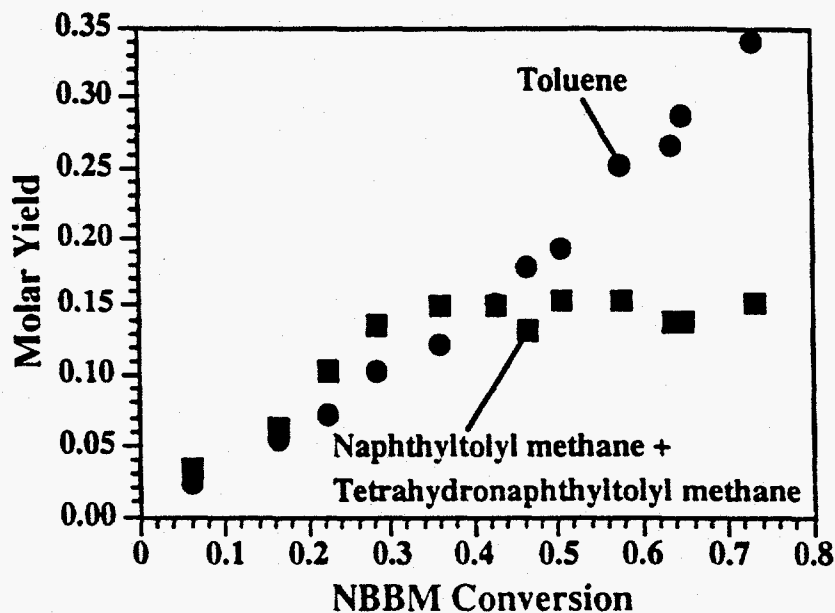


Figure 2.15 Bond D scission products for NBBM hydrolysis at 420 °C.

#### 2.4 Summary of NBBM Pyrolysis Results

The thermal chemistry of NBBM at 400 and 420 °C in hydrogen and nitrogen atmospheres was studied. Pyrolysis results are consistent with a free radical reaction scheme with bond thermolysis and radical ipso-substitution steps being most significant. Bond fission reactions, followed by hydrogen abstraction and radical ipso-substitution reactions, which are in turn followed by  $\beta$ -scission reactions, constitute the likely sequence for the formation of the major products. Reaction in a hydrogen atmosphere showed ipso-substitution by benzyl and  $H\cdot$  radicals, which allowed cleavage of both bond A and bond B, whereas, reaction in a nitrogen atmosphere yielded ipso-substitution reactions by benzyl radicals only, effecting bond A scission only.

NBBM pyrolysis at conditions representative of the thermal background for catalytic reactions was also studied. This lower temperature (400 °C) hydrolysis of NBBM was similar to that observed at 420 °C. The pyrolysis products may be grouped as resulting from bond A scission, bond B scission, bond D scission and NBBM hydrogenation. The rate of NBBM consumption at 400 °C was half that at 420 °C suggesting an apparent activation energy of approximately 32 kcal/mole.

## REFERENCES

- Bhore, N.A., Klein, M.T., Bischoff, K.B. (1990a) "The Delplot Technique: A New Method for Reaction Pathway Analysis," *Ind. Eng. Chem. Res.*, **29**, 313.
- Bhore, N.A., Klein, M.T., Bischoff, K.B. (1990b) "Species Rank in Reaction Pathways: Application of the Delplot Analysis," *Chem. Eng. Sci.*, **45**, 2109.
- Farcasiu, M., Smith, C. (1991) "Modeling Coal Liquefaction. 1. Decomposition of 4-(1-Naphthylmethyl)bibenzyl Catalyzed by Carbon Black," *Energy & Fuels*, **5**, 83.
- Guin, J., Zhan, X., Singh, R. (1993) "Activity and Selectivity of Dispersed Iron Catalysts in Coal Liquefaction and Model Compound Reactions," *Prepr. Paper: Am. Chem. Soc., Div. Fuel Chem.*, **38**, 86.
- Linehan, J.C., Darab, J.G., Matson, D.W. (1993) "Results of Catalyst Testing Using Iron-based Catalysts," *Prepr. Paper: Am. Chem. Soc., Div. Fuel Chem.*, **38**, 66.

### Chapter 3

#### A MECHANISTIC MODEL PROBING REACTION KINETICS AND PATHWAYS OF 4-(1-NAPHTHYLMETHYL)BIBENZYL

The driving force of specifying hydrocarbon mixture properties, and the enabling technologies of analytical chemistry and computational hardware, have resulted in considerable activity in the formulation of detailed, molecular hydrocarbon conversion process models, even for heavy materials such as coal and resids. This is because molecule-based modeling offers the most compelling opportunity for the rigorous development of structure/property relationships. Reactivity is an especially significant property that can be discerned given a molecule's (and its reaction environment's) structure. Other properties fall into performance and environmental classes. Performance properties, such as octane number, smoke point, cetane number, and the like, and environmental properties, such as RVP, aromatics content,  $T_{90}$ , *etc.*, are increasingly sought as output of reaction models. Thus, the potential advantages of molecule-based modeling are clear. Less readily apparent, however, is that the development and operation of molecular models comes with an apparently insurmountable requirement for reactivity information. This conflict needs to be resolved before molecular models can become a useful tool for process analysis.

The challenge is due to the staggering complexity of petroleum hydrocarbon mixtures. Modern analytical methods indicate the existence of at least  $O(10^5)$  different molecules in these mixtures; heavy-end feeds contain oligomeric species of unique molecular connectivities. The sheer size of the thus-implied

modeling problem engenders a conflict between the need for molecular detail and the formulation and solution of the model. Traditional deterministic models can comprise an extremely large number of species and therefore differential equations. Thus, the formulation, let alone solution, of the model would be formidable. Moreover, the required database of reaction pathways and kinetics is enormous. This can be obtained, in principle, through chemically significant model compound experiments or through parameter estimation where model parameters are fit to experiments with real feeds. The former approach suffers from the practically impossible number of direct experiments required. Parameter estimation approaches suffer because simultaneous regression of many parameters often leaves them individually devoid of chemical significance. Clearly, approaches aimed at reducing the complexity and number of model parameters, i.e., identification of the irreducible complexity level, would be of use.

More careful scrutiny of the composition and reactions of complex petroleum feed stocks suggests much of the complexity is statistical. Each of the  $10^5$ - $10^6$  species falls into one of a handful of compound classes (e.g., paraffins, olefins, naphthenes, aromatics, alkylaromatics, etc.). Thus, the essential complexity is constrained to be the reactions of sets of many similar compounds, where, within each set, compounds differ only in substituents. Differences in rate constants, then, can be traced to substituent effects. This has both qualitative and quantitative implications. Regarding the former, it implies that many chemical reactions will involve only a handful of irreducibly different atomic rearrangements, with substituents affecting the rate but not otherwise participating in the reaction. Thus, a handful (5-12) of atomic reaction matrices could be used to generate the thousands of reactions that differ, largely, in the details of substituents. The quantitative implication is that, to a first-

order approximation, the substituent effects can be handled semi-theoretically. That is, the existence of widely spanning homologous series suggests that the use of linear free energy relationships (LFERs) as an organizational technique and correlational tool for assembling a substantial kinetic data base would be of great utility in quantitative modeling.

The Hammett  $\rho$ - $\sigma$  organization of homogeneous reaction families and substituent effects is the classic LFER (Lowry and Richardson, 1987). Other related structure/activity relationships include the Brönstead (Salem, 1982) and Evans-Polanyi (1938) formalisms. Ultimately, LFER-like structure/reactivity correlations will take the form of a correlation of  $\log k_i$  (or  $\log K_i$ ) versus a reactivity index,  $RI_i$ , for a molecule  $i$  in the reaction family  $j$ . In a strict sense, a LFER is a semiempirical correlation of kinetic data with species' properties. However, transition state theory reveals the basis for this correlation, as shown in Equation 3.1. The parameters  $k_b$ ,  $h$  and  $R$  refer to the Boltzmann, Planck and ideal gas constants, whereas  $T$  specifies the reaction temperature. The free-energy change of activation,  $\Delta G^\ddagger$ , comprises enthalpic ( $\Delta H^\ddagger$ ) and entropic ( $\Delta S^\ddagger$ ) contributions. The nature of a reaction family constrains the problem to one in which the difference in the change of entropy between the transition-state and

$$\log k_i = \log \left[ \frac{k_b T}{h} \right] - \frac{\Delta G_i^\ddagger}{RT} = \log \left[ \frac{k_b T}{h} \right] - \frac{\Delta H_i^\ddagger}{RT} + \frac{\Delta S_i^\ddagger}{R} \quad (3.1)$$

reactants for members of a family is either negligible ( $\Delta(\Delta S_i^\ddagger) = 0$ ) or directly correlated with the differences in the enthalpy ( $\Delta(\Delta S_i^\ddagger) \propto \Delta(\Delta H_i^\ddagger)$ ). In either case, Equation 3.1 can be reduced to the simple relationship between the kinetic rate constant and the enthalpy change of activation, as in Equation 3.2.  $\Delta H_i^\ddagger$  can often be

$$\log k_i = A + B \Delta H_i^\ddagger \quad (3.2)$$



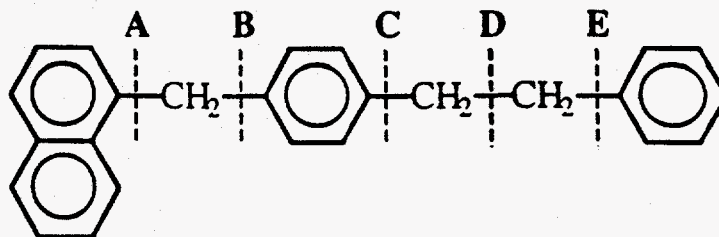
directly or indirectly determined from structural properties of the reactants, intermediates or products. These properties are defined here as reactivity indices, and for a specific reaction path,  $i$ , allow Equation 3.2 to be rewritten as shown in Equation 3.3. The constants  $a$  and  $b$  are determined from a basis set of model compound data and provide valuable information about the reaction-families. From the perspective of

$$\log k_i = a + b RI_i \quad (3.3)$$

modeling of complex feed stocks, however, this provides a basis for estimating  $k_i$  for other molecules  $i$  where no experimental data exist. This would greatly reduce the array of experimental information required to describe the kinetics for the many components in a reaction family into a single slope and intercept.

This exposes the thesis of the present work. The notion is that model compound experiments can be used to obtain the parameters of Equation 3.3 ( $a$  and  $b$ ) for the reaction families in complex mixtures of like chemical moieties. Essentially, this defines intrinsic chemistry as that shared by model compounds and like moieties in the mixture. The goal is to accumulate an LFER data base of fundamental value for the modeling of complex mixtures.

The foregoing motivated the present development of a mechanistic model for the coal and resid model compound 4-(1-naphthylmethyl)bibenzyl (Farcasiu and Smith, 1991) (NBBM), the structure of which being shown in Figure 3.1. NBBM is similar to coal and resids in that it is a multifunctional, low-volatility compound that mimics some of the important attributes of coal and resid, e.g., a fused aromatic moiety connected to other aromatics by short alkyl chains. The structure is also simple enough, however, that the reaction products can be identified and quantified. It is noteworthy that the reaction of NBBM has been shown to be similar to coal in that



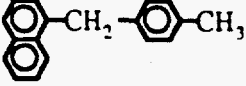
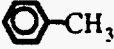
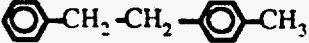

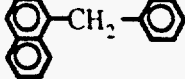
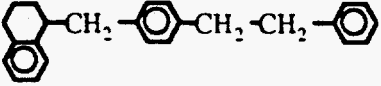
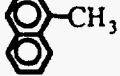

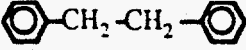

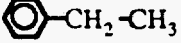

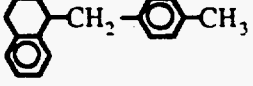
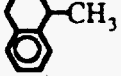
**Figure 3.1** The structure of the coal and resid model compound 4-(1-naphthylmethyl)biphenyl (NBBM). The scissile bonds are labeled A through E.

catalysts which increase the rate of disappearance of NBBM also increase the rate of coal liquefaction (Linehan et al., 1993; and Guin et al., 1993).

### 3.1 Guiding Experimental Results

The experimental findings from the reaction of NBBM in a hydrogen atmosphere will be used to guide the model development, since these conditions are relevant to the hydrotreating and hydrocracking conditions under which coal liquefaction usually occurs. The major products of NBBM hydropyrolysis at 420 °C are listed in Table 3.1. Of these, naphthyltolylmethane and toluene are a result of the fission of NBBM's weak biphenyl linkage (bond D). The formation of naphthalene and methylbiphenyl from the formal cleavage of the A bond is more subtle. Direct fission is unlikely because of the higher bond strengths of the naphthylphenylmethane links. More likely, these products are the result of H• addition at the ipso position of NBBM's naphthyl ring, followed by radical elimination of a methylbiphenyl radical. Thermochemistry drives the elimination of the methylbiphenyl radical fragment over the H• radical strongly. The less prevalent naphthylphenylmethane product likely formed from an analogous benzyl radical ipso addition followed by elimination of the

**Table 3.1** Summary of reaction products from NBBM hydrolysis at 420 °C.

Reaction Products from NBBM Hydrolysis (420 °C)	
Major Products	
Naphthyltolylmethane	
Toluene	
Methylbibenzyl	
Naphthalene	
Minor Products	
Naphthylphenylmethane	
Tetrahydro-NBBM	
Methylnaphthalene	
Tetralin	
Bibenzyl	
Benzene	
Ethylbenzene	
p-Xylene	
Tetrahydronaphthyltolylmethane	
Methyltetralin	

methylbibenzyl radical. Similarly, methylnaphthalene and bibenzyl evolve from H• addition at the "B" ipso position of NBBM's phenyl ring, followed by radical elimination. Benzene and ethylbenzene likely form through  $\beta$ -scission of NBBM radicals on the bibenzyl link. It should be noted that thermochemically improbable ipso substitution of benzyl radicals into phenyl rings does not appear to be kinetically significant at the present conditions, as the absence of diphenylmethane from the observed product spectra attests. The role of molecular hydrogen is thus evidently to help cap energetic free radicals, which both forms stable products and generates the H• radicals necessary for ipso substitution.

The foregoing reactions are key but not exclusive reactions leading to the observed products. Other elementary steps contribute to initiate, propagate and terminate cycles. For example, radical reactions such as hydrogen abstraction, radical hydrogen transfer, radical disproportionation and radical recombination will also occur. Radical hydrogen transfer (RHT) has been elucidated by McMillen et al. (1987a, 1987b, 1990) to involve collision between a hydroaromatic molecule and an aromatic molecule, effecting transfer of a hydrogen atom from the hydroaromatic to the aromatic. This pathway creates radicals and a net radical ipso substitution in one step. Radical hydrogen transfer is most important when the reaction system contains a large concentration of hydroaromatic molecules, which were notably absent in the initial NBBM/H<sub>2</sub> reaction mixture. The slow thermal hydrogenation rates suggest that RHT would not be a prevalent pathway but is included for completeness.

Formally, the reaction products can be generated through the application of the following free radical reaction families: 1) bond fission, 2) hydrogen abstraction, 3)  $\beta$ -scission, 4) radical addition, 5) radical elimination, 6) radical hydrogen transfer, 7) radical disproportionation and 8) radical recombination. In

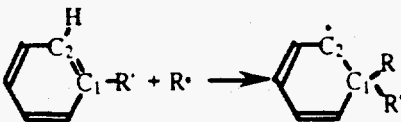
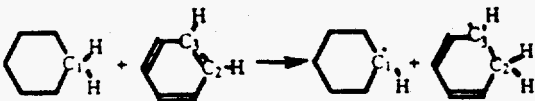
addition, reaction families for 9) hydrogenation of olefins and 10) aromatics are considered. The bond breaking and bond making results of each of these ten reaction families can be summarized concisely in terms of the formal reaction matrix (Broadbelt, 1994) for each. Mathematically, addition of the reaction matrix to the reactant matrix yields the product matrix, as illustrated in Table 3.2 for a representative reaction of each of the ten free radical reaction families.

Table 3.2 thus exposes the reaction matrix to be a mathematical representation of the changes in bonding which occur in molecules as they undergo reaction. Each of the rows and columns of the matrix correspond to an atom which participates in the reaction. The off-diagonal elements of the matrix represent the change in bond order of the associated atoms as a result of the reaction. The diagonal elements represent the change in number of non-bonded electrons (e.g., the formation (+1) or capping (-1) of a free radical center) associated with that atom.

### 3.1.1 Algorithm for Determining Model Reactions

The full mechanistic model was generated through exhaustive application of these reaction families to the NBBM/H<sub>2</sub> starting mixture as well as to all products formed in the NBBM system. Several chemically reasonable rules were invoked to keep the model finite, as, for example, sequential radical recombination/formation could create an infinite carbon number species if uncontrolled. The bond fission rule allowed for only carbon-carbon bonds with dissociation energies less than 75 kcal/mole to react. At the (420 °C) reaction temperature considered, bond fission of stronger bonds was judged to be kinetically insignificant in the time scales of interest (30-60 minutes). The complete set of reaction rules is listed in Table 3.3.

**Table 3.2** Reaction matrices used in constructing the NBBM mechanistic kinetics model.

Reaction Family	Reaction Matrix
Bond Fission $R-R' \longrightarrow R\cdot + R'\cdot$	$\begin{matrix} & R & R' \\ R & \begin{bmatrix} 1 & -1 \end{bmatrix} \\ R' & \begin{bmatrix} -1 & 1 \end{bmatrix} \end{matrix}$
Hydrogen Abstraction $R\cdot + R'H \longrightarrow RH + R'\cdot$	$\begin{matrix} & R & R' & H \\ R & \begin{bmatrix} -1 & 0 & 1 \end{bmatrix} \\ R' & \begin{bmatrix} 0 & 1 & -1 \end{bmatrix} \\ H & \begin{bmatrix} 1 & -1 & 0 \end{bmatrix} \end{matrix}$
$\beta$ -Scission $R-R'-R''\cdot \longrightarrow R\cdot + R'=R''$	$\begin{matrix} & R & R' & R'' \\ R & \begin{bmatrix} 1 & -1 & 0 \end{bmatrix} \\ R' & \begin{bmatrix} -1 & 0 & 1 \end{bmatrix} \\ R'' & \begin{bmatrix} 0 & 1 & -1 \end{bmatrix} \end{matrix}$
Radical Ipso Substitution 	$\begin{matrix} & R & C_1 & C_2 \\ R & \begin{bmatrix} -1 & 1 & 0 \end{bmatrix} \\ C_1 & \begin{bmatrix} 1 & 0 & -1 \end{bmatrix} \\ C_2 & \begin{bmatrix} 0 & -1 & 1 \end{bmatrix} \end{matrix}$
Radical Elimination (Reverse of Radical Ipso Substitution)	$\begin{matrix} & R & C_1 & C_2 \\ R & \begin{bmatrix} 1 & -1 & 0 \end{bmatrix} \\ C_1 & \begin{bmatrix} -1 & 0 & 1 \end{bmatrix} \\ C_2 & \begin{bmatrix} 0 & 1 & -1 \end{bmatrix} \end{matrix}$
Radical Hydrogen Transfer 	$\begin{matrix} & H & C_1 & C_2 & C_3 \\ H & \begin{bmatrix} 0 & -1 & 1 & 0 \end{bmatrix} \\ C_1 & \begin{bmatrix} -1 & 1 & 0 & 0 \end{bmatrix} \\ C_2 & \begin{bmatrix} 1 & 0 & 0 & -1 \end{bmatrix} \\ C_3 & \begin{bmatrix} 0 & 0 & -1 & 1 \end{bmatrix} \end{matrix}$
Radical Disproportionation $R\cdot + R'H-R''\cdot \longrightarrow RH + R'=R''$	$\begin{matrix} & H & R & R' & R'' \\ H & \begin{bmatrix} 0 & 1 & -1 & 0 \end{bmatrix} \\ R & \begin{bmatrix} 1 & -1 & 0 & 0 \end{bmatrix} \\ R' & \begin{bmatrix} -1 & 0 & 0 & 1 \end{bmatrix} \\ R'' & \begin{bmatrix} 0 & 0 & 1 & -1 \end{bmatrix} \end{matrix}$
Radical Recombination (Reverse of Bond Fission)	$\begin{matrix} & R & R' \\ R & \begin{bmatrix} -1 & 1 \end{bmatrix} \\ R' & \begin{bmatrix} 1 & -1 \end{bmatrix} \end{matrix}$

**Table 3.3** Reaction rules used in conjunction with the reaction matrices of Table 3.2 for constructing the NBBM mechanistic kinetics model.

Reaction Family	Reaction Rules
Bond Fission	<p>Allowed for bibenzyl linkages in reactant and primary products.</p> <p>Allow reverse reaction of radical recombination involving an NBBM derived radical and a benzylic radical.</p>
Hydrogen Abstraction	<p>Prohibit abstraction from aromatic rings.</p> <p>Prohibit abstraction by radicals formed from radical ipso substitution.</p> <p>Allow abstraction from reactant and primary products only.</p> <p>Prohibit abstraction from primary products formed solely from radical recombination.</p>
$\beta$ -Scission	<p>Require two consecutive alkyl carbons.</p>
Radical Ipso Substitution	<p>Allow benzyl radical substitution at ipso and nonipso positions of naphthyl rings.</p> <p>Prohibit benzyl radical substitution at phenyl rings.</p> <p>Allow H• radical substitution at ipso position only of naphthyl and phenyl rings.</p>
Radical Elimination	<p>Allow elimination of radicals formed from radical ipso substitution only.</p>
Radical Hydrogen Transfer	<p>Allow radical hydrogen transfer from alkylaromatics to the ipso position of substituted naphthyl rings only.</p>
Radical Disproportionation	<p>Radical disproportionation must lead to olefin formation between two alkyl carbons.</p>
Radical Recombination	<p>Prohibit radical disproportionation with radicals formed from radical ipso substitution.</p> <p>Prohibit radical recombination with radicals formed from radical ipso substitution.</p>

The initial conditions or reactants were NBBM and H<sub>2</sub> gas. Bond fission is the main pathway for creation of radicals in this scheme. In particular, the fission of the weak bibenzyl linkage (bond D) in NBBM was most important at early times. In addition, as is indicated in Table 3.3, selected second-rank products that also contain the bibenzyl linkage were allowed to undergo bond fission to form two relatively stable benzylic radicals.

All radicals except those intermediates formed by radical ipso substitution were allowed to abstract hydrogen from other molecules. The ipso substitution radicals intermediates were considered to undergo very fast radical elimination reactions, so that hydrogen abstraction was essentially not possible. Hydrogen abstraction from aromatic carbons was also prohibited.

Few kinetically significant  $\beta$ -scission pathways were available. The rule for  $\beta$ -scission reactions listed in Table 3.3 required the radical site to be adjacent to an alkyl carbon. This ensured that the bond broken was between an alkyl carbon and either another alkyl carbon, an aromatic carbon or a hydrogen atom. Because NBBM has only short (less than three linkages) alkyl chains, only  $\beta$ -scission of radicals on a bibenzyl linkage was permitted. The required  $\beta$ -scission configuration is found in NBBM, methylbibenzyl and bibenzyl only.

The remaining main pathway for bond breaking is through a radical ipso substitution followed by radical elimination scheme. This effects dealkylation of the original substituted ring. Observed product yields suggest that ipso-substitution by benzyl-type radicals occurs mainly at the naphthalene ring and that ipso-substitution by H• radicals can occur at all ipso-positions. This can be rationalized by the ipso substitution energetics summarized in Table 3.4. Addition of the relatively stable benzyl radical to the ipso position of a naphthalene ring is energetically more



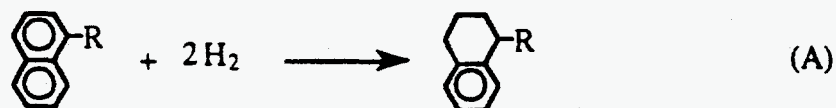
favorable than benzyl addition to a phenyl ring. The highly energetic H• radical is able to access either ring with relative ease. As a result of the lack of measured products from benzyl radical addition to phenyl rings, and its less favorable energetics, the reaction rules for radical ipso substitution were constructed so as to prevent benzyl radical addition to phenyl rings.

**Table 3.4** Energetics for benzyl and H• radical ipso substitution into naphthyl and phenyl rings.

Radical	Model Ring Structure	$\Delta H_{\text{reaction}}$ (kcal/mole)
H•	Methylnaphthalene	-36.11
Benzyl	Methylnaphthalene	-20.73
H•	p-Xylene	-32.13
Benzyl	p-Xylene	-17.11
H•	Toluene	-31.02
Benzyl	Toluene	-12.60

The radical hydrogen transfer reaction family was included because of the small concentration of product hydroaromatic molecules. Radical hydrogen transfer from hydroaromatic compounds was applied to the ipso position of substituted naphthyl groups.

In addition to the elementary steps noted above, several global hydrogenation reactions were included. They involve the saturation of naphthyl condensed rings to tetrahydronaphthyl species and olefins to alkanes, as shown in Figure 3.2. The inclusion of these reactions enables all of the observed products to be predicted by the model.



**Figure 3.2** Non-free radical reaction families included in NBBM model:  
(A) naphthyl hydrogenation; (B) olefin hydrogenation.

Application of the reaction matrices and the associated rules of Tables 3.2 and 3.3 generated a mechanistic model totaling 1,374 reactions, which can be organized into reaction families as follows: 21 bond fission reactions, 416 hydrogen abstraction reactions, 14  $\beta$ -scission reactions, 35 radical hydrogen transfer reactions, 66 radical addition reactions, 71 radical elimination reactions, 359 radical disproportionation reactions, 377 radical recombination reactions, 8 olefin hydrogenation reactions and 7 naphthyl hydrogenation reactions. The molecularity provided the rate expression for not only the elementary steps but also the global hydrogenation rates. Thus, solution of the 401 ordinary differential equations comprising this model required only estimates of the associated rate constants.

### 3.1.2 Estimation of Rate Constants

The reaction family concept was exploited to estimate the rate constant for each reaction step also. This is based on the use of a linear free energy relationship (LFER) for each family. Semenov (1958), McMillen and Malhotra (1990) and LaMarca (1992) have demonstrated the validity of LFERs (e.g., a Polanyi relation) for correlating rate constants to heats of reaction for free radical reaction families. This

helped motivate the present lumping scheme, where the rate constant ( $k$ ) for each reaction is constrained by the reaction enthalpy ( $\Delta H_{\text{reaction}}$ ) according to the relationship of Equation 3.4. In this lumping scheme, each reaction family is characterized by the

$$\log_{10} k = A - \frac{\alpha \Delta H_{\text{reaction}}}{2.303RT} \quad (3.4)$$

two parameters,  $A$  and  $\alpha$ . In the present application, the value of  $\alpha$  was fixed at 0.5 for all reaction families except bond fission and radical recombination. For the former, the value was 1.0, and for the latter the value was 0.0. The value of the parameter  $A$  for each reaction family was determined by regression of the mechanistic model predictions to experimental reaction data.

A form for the LFER similar to that shown in Equation 3.4 is also commonly employed which explicitly exposes the value of the Arrhenius pre-exponential factor and a linear dependence of the activation energy on the enthalpy of reaction. Equation 3.5 shows such an LFER where  $E_0$  and  $\alpha$  represent the intercept and slope of this linear dependence. Thus, once the parameter  $A$  from Equation 3.4 is determined, then specification of the Arrhenius pre-exponential factor allows specification of the parameter  $E_0$ .

$$\log_{10} k = \log_{10} A_{\text{Arrhenius}} - \frac{E_0 + \alpha \Delta H_{\text{reaction}}}{2.303RT} \quad (3.5)$$

Table 3.4 summarizes the kinetically independent reaction families. The list contains all the reaction families listed previously with additional subdivisions. For example, it is reasonable to expect that the transition state for addition of an H• radical and that for addition of a benzyl radical to be sufficiently different as to require a separate set of LFER parameters for each. Similarly, the topological differences between a naphthalene ring versus a phenyl ring and, to a lesser extent, a naphthalene

ring versus a substituted naphthalene ring, suggest different A factors would be expected for radical addition and hydrogenation reactions. Finally, the presence of bulky substituent groups can also affect the transition state sterics, and this has been accounted for in the radical addition and radical recombination families.

Prediction of the rate constants thus amounted to obtaining the reaction enthalpies. This was calculated as the difference between the enthalpy of formation ( $\Delta H^\circ_f$ ) of the products from the reactants. Because many model components, especially fleeting intermediates such as radicals, were without experimental values,

Table 3.5 Summary of reaction families used to predict rate constants.

Reaction Family	$\log_{10} k$
Bond Fission	$14.2 + \frac{\Delta H_{\text{reaction}}}{2.303 RT}$
Hydrogen Abstraction	$6.31 + \frac{\Delta H_{\text{reaction}}}{4.606 RT}$
$\beta$ -Scission	$8.25 + \frac{\Delta H_{\text{reaction}}}{4.606 RT}$
Ipsso-Radical Addition of a Benzyl Radical to a Naphthalene Ring	$2.00 + \frac{\Delta H_{\text{reaction}}}{4.606 RT}$
Nonipso- Radical Addition of a Benzyl Radical to a Naphthalene Ring	$1.00 + \frac{\Delta H_{\text{reaction}}}{4.606 RT}$
Ipsso-Radical Addition of an H $\cdot$ Radical to a Naphthalene Ring of NBBM	$-0.40 + \frac{\Delta H_{\text{reaction}}}{4.606 RT}$
Ipsso-Radical Addition of an H $\cdot$ Radical to a Substituted Naphthalene Ring	$0.10 + \frac{\Delta H_{\text{reaction}}}{4.606 RT}$
Ipsso-Radical Addition of an H $\cdot$ Radical to a Phenyl Ring	$0.00 + \frac{\Delta H_{\text{reaction}}}{4.606 RT}$
Radical Elimination	$7.56 + \frac{\Delta H_{\text{reaction}}}{4.606 RT}$
Radical Hydrogen Transfer	$1.60 + \frac{\Delta H_{\text{reaction}}}{4.606 RT}$
Radical Disproportionation	$5.39 + \frac{\Delta H_{\text{reaction}}}{4.606 RT}$
Radical Recombination	9.00
Radical Recombination of Sterically Hindered Radicals	4.00
Hydrogenation of an Olefin	$-2.82 + \frac{\Delta H_{\text{reaction}}}{4.606 RT}$
Hydrogenation of Naphthalene	$-1.47 + \frac{\Delta H_{\text{reaction}}}{4.606 RT}$
Hydrogenation of Substituted Naphthalene	$-1.54 + \frac{\Delta H_{\text{reaction}}}{4.606 RT}$

estimation techniques were examined. For this purpose, computational quantum chemistry served as the tool for estimating species properties (e.g.,  $\Delta H_f^\circ$ ) from structure.

Computational quantum chemistry has been demonstrated by Neurock (1992) to be a reliable method for estimating LFER reaction indices. Specifically, semiempirical methods such as the MOPAC program (Stewart, 1989), which utilizes an MNDO method for solving the Schrödinger equation (Dewar et al., 1977a, 1977b, 1978a, 1978b), are both useful and relatively easy to use. Herein, MOPAC calculations with the AM1 parameter set and using the CAChe<sup>®</sup> graphical interface, were employed to estimate enthalpies of formation.

### 3.2 Parameter Optimization

Optimization of the model parameters was achieved through the use of the multilevel single linkage (MLSL) algorithm, as coded by Stark (1993), on an IBM RS/6000 Model 530H workstation. Briefly, the MLSL program randomly chooses points within the parameter space at which the objective function is evaluated. Subsequently, a local minimization procedure is started at 10% of the randomly chosen points which have the lowest objective function value. The identified local minima are reported, and the local minima with the smallest objective function value is taken as the global minimum.

The objective function (F) used for the regression was a variation of the sum of square errors shown in Equation 3.6, where  $y_{ij}^{\text{pred}}$  and  $y_{ij}^{\text{exp}}$  are the predicted and

$$F = \sum_{j=1}^{\text{\#times}} \sum_{i=1}^{\text{\#comp}} w_i (y_{ij}^{\text{pred}} - y_{ij}^{\text{exp}})^2 \quad (3.6)$$

measured molar yields for product  $i$  at time  $j$ , respectively. The weighting factor ( $w_i$ ) enables the contribution of each species to the objective function to be manipulated.

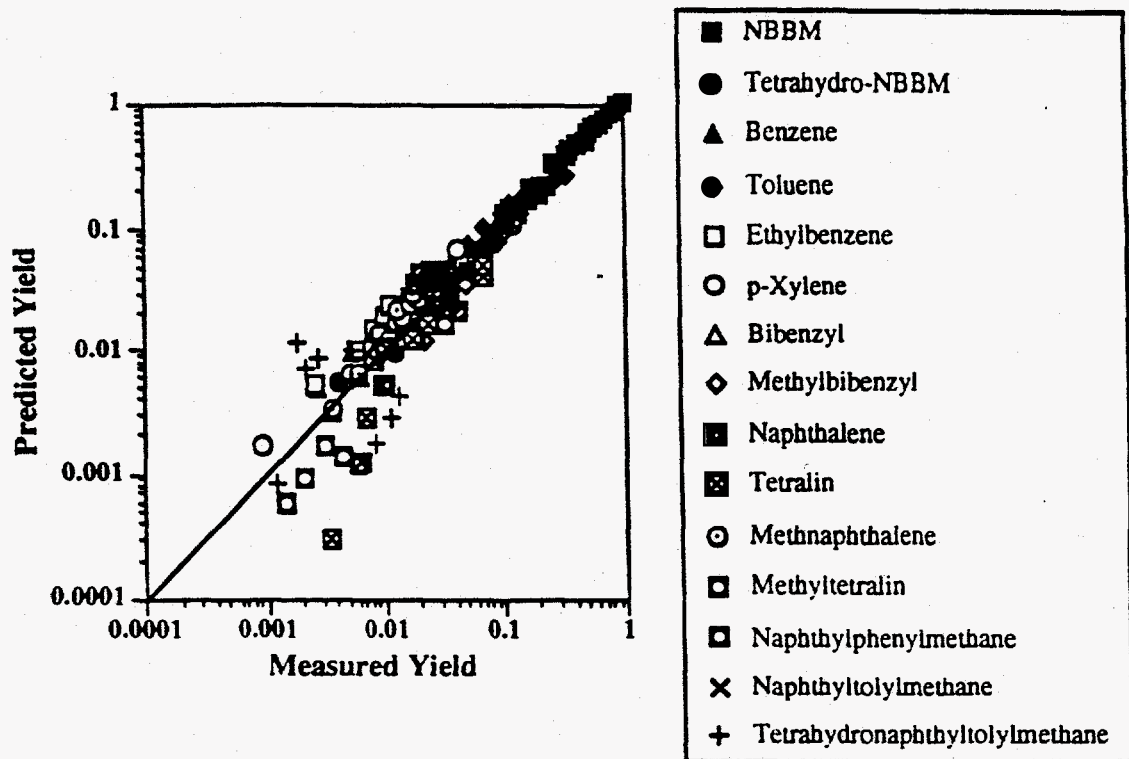
Model predictions of the main hydrolysis products were compared to the associated experimental hydrolysis data at 420 °C under 1000 psig H<sub>2</sub> (cold). Regression of the A parameters for each of the reaction families of Table 3.5 employing the weighting factors listed in Table 3.6 enabled balanced contributions to the objective function from each of the products. The results of the regression are summarized in the form of the parity plot of Figure 3.3, and the values of the optimal parameters (A) are listed in Table 3.7. The regressed A parameters and typical values for the Arrhenius pre-exponential factors found in the literature (LaMarca, 1992; and McMillen and Malhotra, 1990) allow the specification of the E<sub>o</sub> values shown in Table 3.7. Figure 3.3 shows that the model predictions agree well with the experimental results except for a few low-yield products, which constitute less than 1% of the mixture. Thus, the mechanistic model is validated in its ability to describe NBBM hydrolysis at 420 °C.

### 3.3 Mechanistic Modeling Results

The now validated model can be used to probe the important NBBM reaction pathways and underlying reaction mechanisms. This in turn may provide insight into the important reaction pathways occurring during coal liquefaction. The NBBM pyrolysis model was thus examined in terms of the contributions to the overall rate of formation of key products by each individual reaction path.

The time dependence of the rates of the NBBM disappearance reaction paths are summarized in Figure 3.4. The normalizations of the rates shown in Figures 3.4, 3.6-3.8 were performed by scaling all of the contributing rates in each figure by the maximum value of the figure's largest contributing rate. For example, all the rates shown in Figure 3.4 are scaled by the value of the rate of olefin hydrogenation at 30 minutes. This scaling provides a different normalization for each figure, and ensures that the values of the relative rates fall between 1 and -1 for each figure. In Figure 3.4, a positive value for the normalized rate signifies net NBBM formation and a negative value signifies net NBBM destruction. NBBM was consumed from fission of the bibenzyl bond, hydrogen atom abstraction, radical addition to any of its ipso positions, radical hydrogen transfer and naphthyl hydrogenation. NBBM was formed from radical elimination reactions, recombination of two radicals (such as a methylnaphthyl radical with a bibenzyl radical) and olefin hydrogenation of the 4-(1-naphthylmethyl)-stilbene molecule.





**Figure 3.3** Results of parameter regression for the mechanistic model describing NBBM pyrolysis at 420 °C in a hydrogen atmosphere.

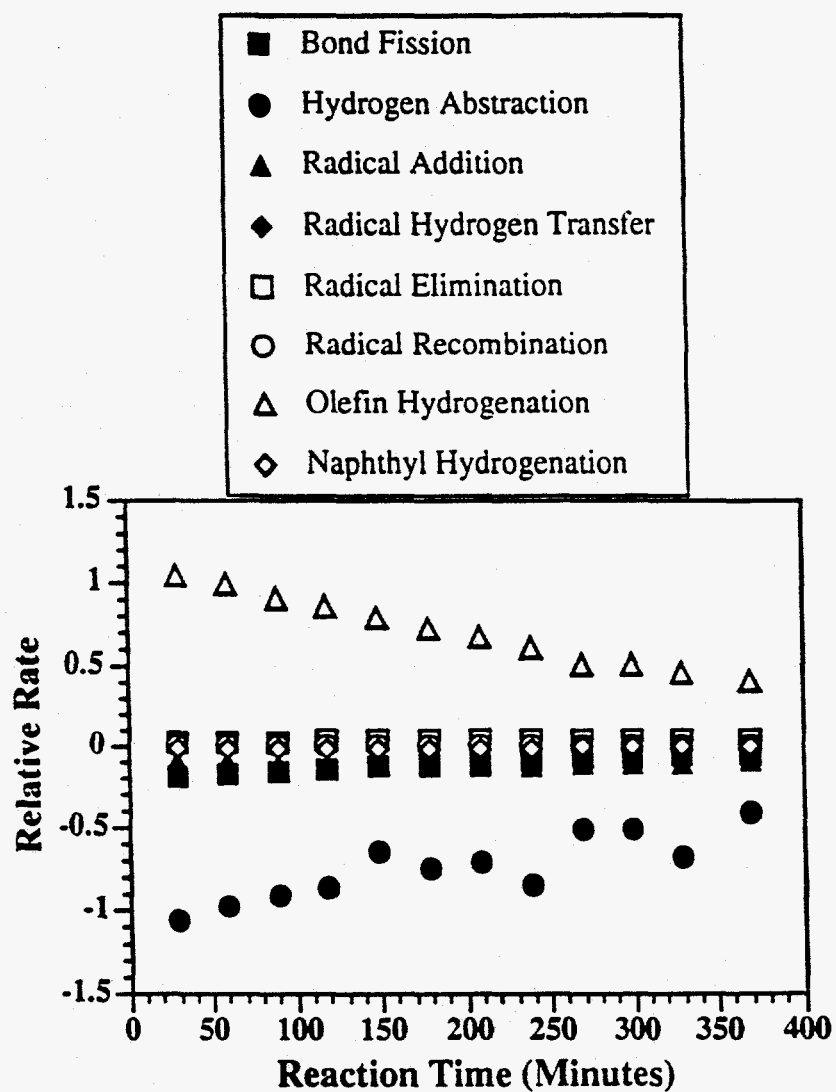
**Table 3.6** Observed products from NBBM hydrolysis at 420°C under 1000 psig hydrogen (cold).

$w_1$	Reaction Products from NBBM Hydrolysis (420 °C)	
1	NBBM	
40	Tetrahydro-NBBM	
1	Benzene	
1	Toluene	
1	Ethylbenzene	
1	p-Xylene	
1	Bibenzyl	
1	Methylbibenzyl	
1	Naphthalene	
12	Tetralin	
1	Methylnaphthalene	
100	Methyltetralin	
1	Naphthylphenylmethane	
10	Naphthyltolylmethane	
100	Tetrahydronaphthyltolylmethane	

**Table 3.7** Optimal parameters for the mechanistic model describing NBBM hydrolysis at 420 °C.

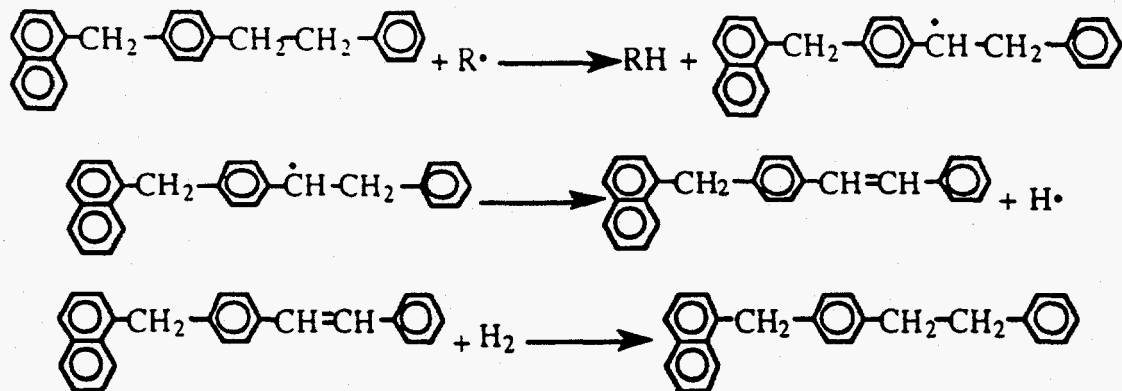
Reaction Family	A	E <sub>o</sub>	log <sub>10</sub> A <sub>Arrhenius</sub>
Bond Fission	14.2	0.0	14.2
Hydrogen Abstraction	6.31	6.9	8.5
β-Scission	8.25	15.1	13.0
Ipsso-Radical Addition of a Benzyl Radical to a Naphthalene Ring	2.00	19.0	8.0
Nonipso-Radical Addition of a Benzyl Radical to a Naphthalene Ring	1.00	22.2	8.0
Ipsso-Radical Addition of an H• Radical to a Naphthalene Ring of NBBM	-0.40	26.6	8.0
Ipsso-Radical Addition of an H• Radical to a Substituted Naphthalene Ring	0.10	25.1	8.0
Ipsso-Radical Addition of an H• Radical to a Phenyl Ring	0.00	25.4	8.0
Radical Elimination	7.56	17.3	13.0
Radical Hydrogen Transfer	1.60	20.3	8.0
Radical Disproportionation	5.39	11.4	9.0
Radical Recombination	9.00	0.0	9.0
Radical Recombination of Sterically Hindered Radicals	4.00	15.9	9.0
Hydrogenation of an Olefin	-2.82		
Hydrogenation of Naphthalene	-1.47		
Hydrogenation of Substituted Naphthalene	-1.54		

Figure 3.4 shows that most of the activity of NBBM involves its consumption through hydrogen abstraction and formation through olefin hydrogenation, whose rates are nearly balanced. Since the experimental findings



**Figure 3.4** Reaction paths for NBBM disappearance and their relative contributions for NBBM hydrolysis at 420 °C.

indicate that net destruction of NBBM is effected mainly through bond fission and radical addition reactions (bond D scission and bond A scission), a reaction cycle such as that shown in Figure 3.5 seems likely. This cycle involves hydrogen abstraction from NBBM, followed by  $\beta$ -scission yielding an  $H\cdot$  radical and 4-(1-naphthylmethyl)stilbene, which is subsequently hydrogenated to return NBBM. The net effect of this reaction cycle is the transformation of alkyl radicals into  $H\cdot$  radicals with no net loss of NBBM. The  $H\cdot$  radicals can then carry out the observed ipso substitution chemistry.



**Figure 3.5** NBBM reaction cycle which effects transformation of  $R\cdot$  radicals to  $H\cdot$  radicals. This cycle is predicted by the mechanistic kinetics model for NBBM hydroperolysis at 420 °C.

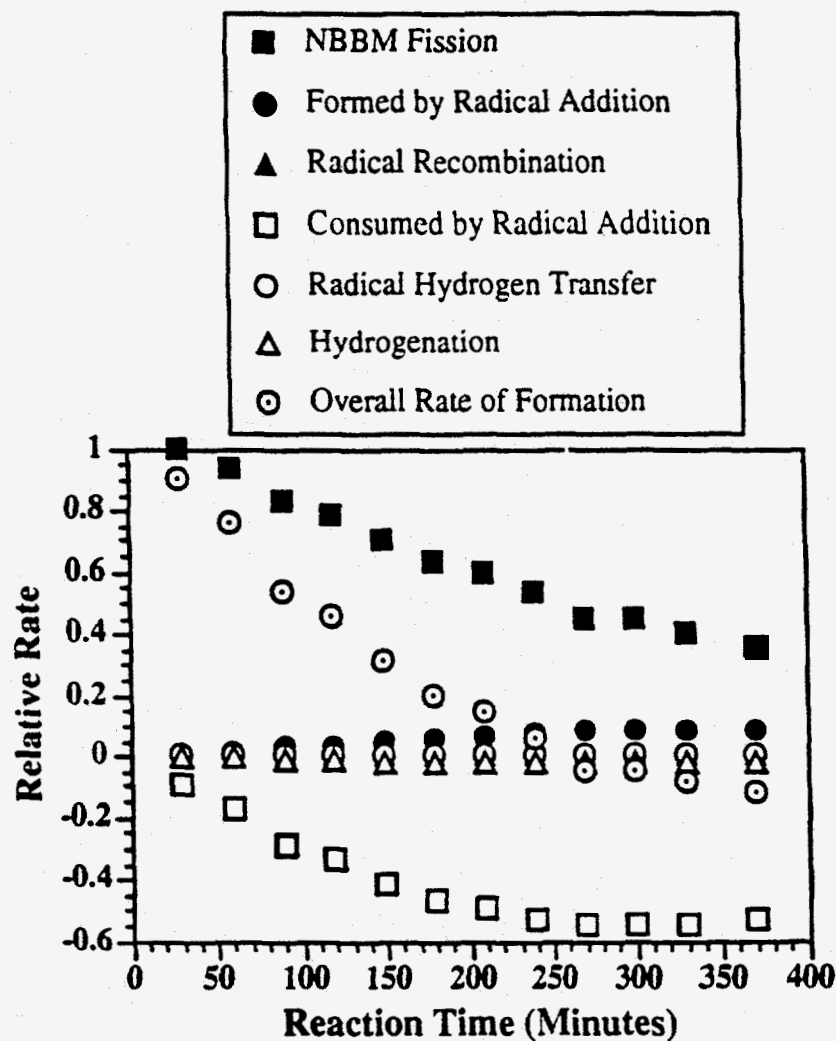
The products of NBBM hydroperolysis were analyzed in a similar manner. Figure 3.6 summarizes the rate information for the reactions involving naphthyltolylmethane, whose main formation route was attributed to fission of NBBM followed by hydrogen abstraction by the naphthyltolylmethyl radical. The mechanistic model accounts for several additional pathways for the formation of naphthyltolylmethane, including ipso substitution of a p-xylene radical at a

naphthalene ring followed by radical elimination, and recombination of two radicals such as a naphthyl radical and a p-xylene radical. In addition, naphthyltolylmethane can be consumed by secondary reactions, such as radical addition, radical hydrogen transfer and naphthyl hydrogenation. Figure 3.6 shows that fission of NBBM is the dominant pathway for naphthyltolylmethane formation, with a small contribution from ipso substitution of a p-xylene radical at a naphthalene ring and subsequent radical elimination. Radical hydrogen transfer, radical recombination and naphthyl hydrogenation have virtually no effect on the yield of naphthyltolylmethane. As the reaction time increases, however, consumption of naphthyltolylmethane by ipso radical addition becomes more significant, and causes the overall rate of formation of naphthyltolylmethane to drop below zero.

The analysis for the reactions of p-xylene is summarized in Figure 3.7. These modeling results indicate that the dominant pathway for formation of p-xylene is through ipso substitution at the naphthalene ring of naphthyltolylmethane, followed by elimination of the p-xylene radical and subsequent hydrogen abstraction. Bond fission of methylbibenzyl also contributes to p-xylene formation. The major pathway for p-xylene consumption is through hydrogen abstraction from a benzylic carbon, followed by ipso substitution of the resulting radical.

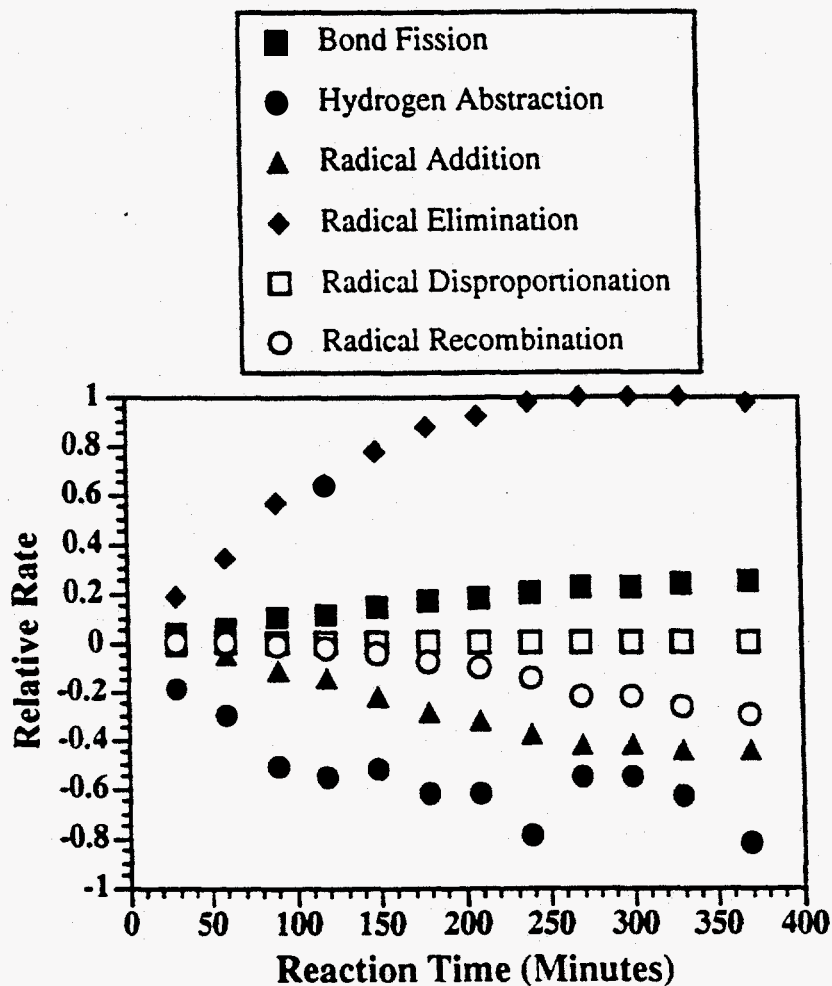
The model results shown in Figure 3.8 confirm ipso substitution of a benzyl radical to a substituted naphthalene followed by radical elimination as the controlling naphthylphenylmethane chemistry at longer reaction times. However, at shorter times, formation of naphthylphenylmethane from  $\beta$ -scission of an NBBM bibenzyl radical followed by hydrogen abstraction of the resulting radical is dominant. At longer reaction times naphthylphenylmethane is consumed by ipso substitution of alkyl and H• radicals. There was no net gain or loss after 360 minutes.

The NBBM hydrolysis products bibenzyl and methylbibenzyl undergo similar reactions. Both are formed primarily through radical ipso substitution. Bibenzyl evolves from H• addition to a phenyl ring of NBBM, whereas methylbibenzyl forms from radical addition to the naphthyl ring of NBBM. Both are



**Figure 3.6** Rates of relevant elementary steps of naphthyltolylmethane as predicted by the mechanistic model.

also involved in the reaction cycle of Figure 3.5 that effects the transformation of alkyl radicals to  $H\cdot$  radicals. Both species also form significantly from recombination of two relatively stable benzylic radicals. As a result, the "reverse" bond fission is also energetically favorable.



**Figure 3.7** Rates of relevant elementary steps of p-xylene as seen through the actions of the p-xylene benzylic radical.



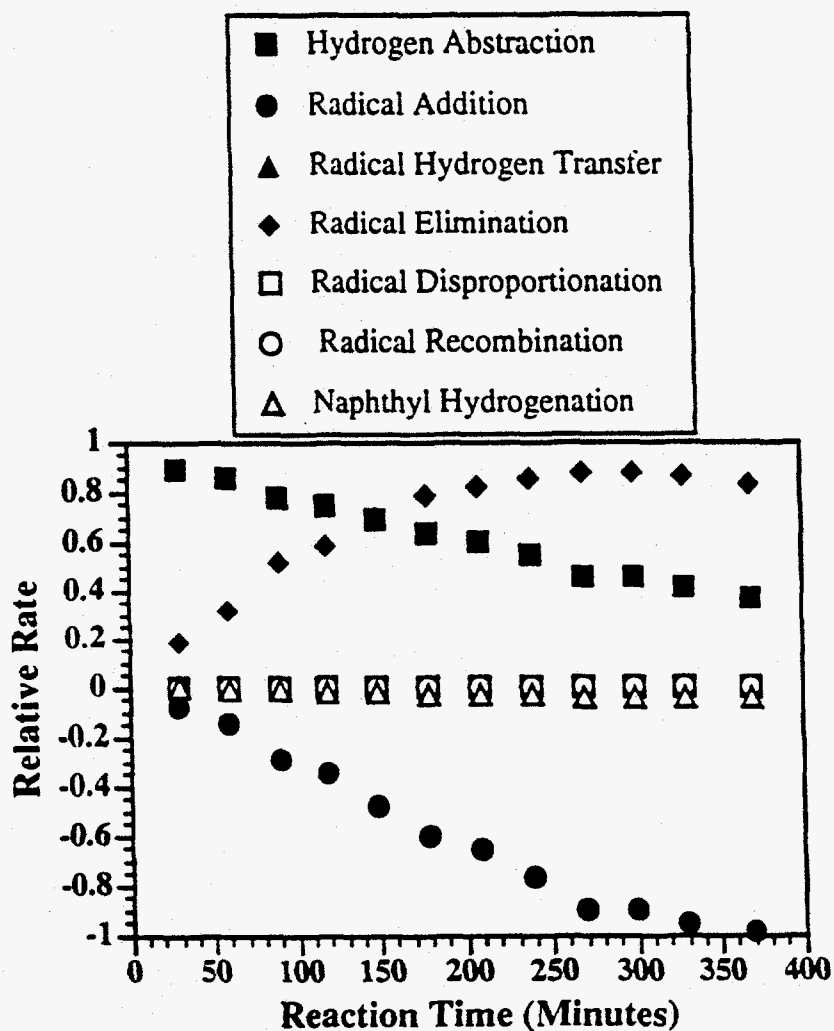


Figure 3.8 Reactivities of naphthyltolylmethane as predicted by the mechanistic model.

The reaction options of naphthalene, methylnaphthalene, benzene, ethylbenzene and toluene are relatively few. Naphthalene and methylnaphthalene form from radical ipso substitution followed by radical elimination. Methylnaphthalene also forms via hydrogen abstraction. Benzene and ethylbenzene form mainly from the  $\beta$ -scission reactions of NBBM derived bibenzyl radicals, with subsequent hydrogen abstraction by the phenyl radical or olefin hydrogenation of the

styrene. A small contribution to these two products from H• ipso substitution at phenyl rings is also predicted. Likewise, toluene is formed mainly from a bibenzyl bond fission hydrogen abstraction sequence, but a small contribution from ipso substitution at naphthylphenylmethane is also predicted.

The naphthyl hydrogenation products, tetralin, methyltetralin, tetrahydronaphthyltolylmethane and tetrahydro-NBBM, are predicted as well. Naphthyl hydrogenation is the sole pathway for the formation of methyltetralin and tetrahydro-NBBM. However, tetralin and tetrahydronaphthyltolylmethane also have small contributions from bond fission.

### 3.4 Summary and Conclusions

To resolve the conflict between the desire for molecular-level detail in kinetic modeling of complex mixtures and the overwhelming number of reactions and rate constants this entails, a mechanistic modeling approach employing the concept of reaction families and LFERs for rate constant evaluation was followed. The model compound, NBBM, revealed the intrinsic chemistry that is also followed by like moieties in coals. NBBM hydrolysis reaction families were summarized in the form of reaction matrices, each with a set of associated rules. A mechanistic model for its pyrolysis was constructed through the exhaustive application of the matrices and rules to the components of the reacting system.

LFER parameters were regressed to fit the model predictions with observed experimental yields for NBBM hydrolysis at 420 °C. Because of the fundamental nature of this model, the quantitative LFER parameters obtained from kinetics analysis can be used to estimate rate constants in a model of several heavy hydrocarbon complex systems. The model was validated by the close agreement

between experimental findings and model predictions. The mechanistic model was then used to probe the controlling mechanisms of NBBM pyrolysis. This identified a reaction cycle that effected the transformation of alkyl radicals into H• radicals through a series of hydrogen abstraction,  $\beta$ -scission and hydrogenation steps. In addition, the major reaction families contributing to NBBM consumption were found to be bond fission, radical ipso substitution by H• and benzyl radicals with subsequent elimination and  $\beta$ -scission. In summary, the mechanistic model provided two major contributions: 1) fundamental kinetic parameters of broad significance, and 2) insight into the specific pathways and mechanisms occurring during NBBM hydrolysis and thus, occurring during coal liquefaction.

## REFERENCES

- Allen, D.T., Gavalas, G. R. (1984) "Reactions of Methylene and Ether Bridges," *Fuel*, **63**, 586.
- Broadbelt, L.J. (1994) *The Thermal Stability of High Performance Polymeric Materials: A Chemical Modeling Analysis*. (Ph.D. Dissertation, University of Delaware.)
- Dewar, M.J.S., Thiel, W. (1977a) "Ground States of Molecules. 38. The MNDO Method Approximations and Parameters," *J. Am. Chem. Soc.*, **99**, 4899.
- Dewar, M.J.S., Thiel, W. (1977b) "Ground States of Molecules. 39. MNDO Method Results for Molecules Containing Hydrogen, Carbon, Nitrogen and Oxygen," *J. Am. Chem. Soc.*, **99**, 4907.
- Dewar, M.J.S., Ford, G.P., McKee, M.L., Rzepa, H.S., Thiel, W., Yamaguchi, Y. (1978a) "Semiempirical Calculations of Molecular Vibrational Frequencies: The MNDO Method," *J. Molec. Struct.*, **43**, 135.
- Dewar, M.J.S., Rzepa, H.S. (1978b) "Calculations of Electron Affinities Using the MNDO Semiempirical SCF-MO Method," *J. Am. Chem. Soc.*, **100**, 784.
- Evans, M.G., Polanyi, M. (1938) "Inertia and Driving Force of Chemical Reactions," *Trans. Faraday Soc.*, **34**, 11.
- Farcasiu, M., Smith, C. (1991) "Modeling Coal Liquefaction. 1. Decomposition of 4-(1-Naphthylmethyl)bibenzyl Catalyzed by Carbon Black," *Energy & Fuels*, **5**, 83.
- Guin, J., Zhan, X., Singh, R. (1993) "Activity and Selectivity of Dispersed Iron Catalysts in Coal Liquefaction and Model Compound Reactions," *Prepr. Paper: Am. Chem. Soc., Div. Fuel Chem.*, **38**, 86.
- LaMarca, C. (1992) *Kinetic Coupling in Multicomponent Pyrolysis Systems*. (Ph.D. Dissertation, University of Delaware.)
- Linehan, J.C., Darab, J.G., Matson, D.W. (1993) "Results of Catalyst Testing Using Iron-based Catalysts," *Prepr. Paper: Am. Chem. Soc., Div. Fuel Chem.*, **38**, 66.
- Lowry, T.H., Richardson, K.S. (1987) *Mechanism and Theory in Organic Chemistry*, 3rd ed. (Harper & Row, New York.)

- McMillen, D.F., Malhotra, R., Hum, G.P., Chang, S. (1987a) "Hydrogen-Transfer-Promoted Bond Scission Initiated by Coal Fragments." *Energy & Fuels*, **7**, 193.
- McMillen, D.F., Malhotra, R., Chang, S., Ogier, W.C., Nigenda, S.E., Fleming, R.H. (1987b) "Mechanisms of Hydrogen Transfer and Bond Scission of Strongly Bonded Coal Structures in Donor-Solvent Systems." *Fuel*, **66**, 1611.
- McMillen, D.F., Malhotra, R. (1990) "A Mechanistic Numerical-Model for Coal Liquefaction Involving Hydrogenolysis of Strong Bonds. Rationalization of Interactive Effects of Solvent Aromaticity and Hydrogen Pressure." *Energy & Fuels*, **4**, 184.
- Neurock, M. (1992) *A Computational Chemical Reaction Engineering Analysis of Complex Heavy Hydrocarbon Reaction Systems*. (Ph.D. Dissertation, University of Delaware.)
- Neurock, M., Klein, M.T. (1993) "When You Can't Measure - Model." *Chemtech*, September, 26.
- Noor, N.S., Gaines, A.F., Abbott, J.M. (1985) "Effect of Pressure on the Hydrolysis of Manvers Coal." *Fuel*, **64**, 1274.
- Salem, L. (1982) *Electrons in Chemical Reactions: First Principles*. (John Wiley and Sons, New York.)
- Semenov, N.N. (1958) *Some Problems in Chemical Kinetics and Reactivity Volume II*. (Princeton University Press, Princeton, NJ.)
- Stark, S.M. (1993) *An Investigation of the Applicability of Parallel Computation to Demanding Chemical Engineering Problems*. (Ph.D. Dissertation, University of Delaware.)
- Stewart, J.J.P. (1989) "Semiempirical Molecular Orbital Methods," in *Reviews in Computational Chemistry*. (K.B. Lipkowitz and D.B. Boyd, eds., VCH Publishers Inc.)

## Chapter 4

### MODEL COMPOUND REACTIONS OVER SOLID CATALYSTS

Coal liquefaction can be viewed as a competition between bond breaking and bond-making, retrogressive reactions. The latter work counter to the main goal of molecular weight reduction, and are caused by condensation, radical addition and radical recombination reactions. This has motivated the search for coal liquefaction catalysts with a combination of desirable properties. Among these, activity for breaking the strong bonds in coal as well as for hydrogen transfer, which can saturate olefins and cap free radicals and thereby prohibit retrogressive reactions, must exist.

The potential catalysts must also be relatively inexpensive and environmentally benign. In addition, fine-particle catalysts, are of extreme interest due to their ability to access more coal surface area (Andrés et al., 1983; Watanabe et al., 1984; Herrick et al., 1990; Prégermain, 1985; Takemura et al., 1985; Pradhan et al., 1991, 1992; Huffman et al., 1993; and Zhang et al., 1994). These considerations motivated examination of fine-particle metal catalysts and catalytic precursors.

The study of coal liquefaction catalysts and catalysis, per se, can be frustrated by the enormous complexity of and extrinsic factors associated with experiments using actual coals. This has motivated the use of model compounds for the first-pass screening of potential catalytic materials. The well-defined nature of model compounds also permits mechanistic analysis of the elementary steps and thermochemistry controlling the catalysis. This is an important first step in kinetics-assisted design of catalysts. The coal model compound 4-(1-naphthylmethyl)biphenyl

(NBBM) is ideal for these purposes. It contains several coal-like functional groups and, overall, has a volatility more like that of the actual coal moieties than most other model compounds can achieve.

#### 4.1 Experimental Plan

The foregoing motivated the study of a series of catalytic materials, or catalyst precursors, for reaction with NBBM. The overall experimental plan is summarized in Table 4.1. Table 4.1 shows the two categories of catalytic materials examined, iron carbonyl-based catalyst precursors and transition metal-based catalytic materials and catalyst precursors. The use of iron pentacarbonyl-based catalyst precursors was motivated by the observations that iron pentacarbonyl has been shown to form fine particles under coal liquefaction conditions (Herrick et al., 1990), has shown activity for catalyzing coal liquefaction reactions (Pradhan et al., 1991), and is inexpensive. Under coal liquefaction conditions,  $\text{Fe}(\text{CO})_5$  is thermally unstable, being converted to catalytically active iron pyrrhotite ( $\text{Fe}_{1-x}\text{S}$ ) in the presence of sulfur (Herrick et al., 1990). Therefore, to consider the effects of thermal stability and ligand composition on the activity of the thermal decomposition product, triphenylphosphine ( $\text{PPh}_3$ ) and carbon disulfide ( $\text{CS}_2$ ) ligands were introduced into the iron coordination sphere by the preparation of the compounds  $\text{Fe}(\text{CO})_4\text{PPh}_3$ ,  $\text{Fe}(\text{CO})_3(\text{PPh}_3)_2$ , and  $\text{Fe}(\text{CO})_3(\text{PPh}_3)_2\text{CS}_2$  (Walter et al., 1994a, 1994b). In addition, reaction of  $\text{Fe}(\text{CO})_3(\text{PPh}_3)_2$  in the presence of either hydrogen or nitrogen was performed to assess the importance of molecular hydrogen during catalytic reaction of NBBM.

The similarity in composition of these catalyst precursors would suggest that the active species formed upon decomposition would have similar properties. Since kinetics-assisted design of catalysts is enhanced by examination of catalytic

species with a wide range of properties. catalytic materials containing transition metals other than iron were also examined. The transition metal-based materials included the catalyst precursors  $\text{Fe}(\text{CO})_5$ ,  $\text{Mo}(\text{CO})_6$  and  $\text{Mn}_2(\text{CO})_{10}$  and the catalytic materials  $\text{Fe}_2\text{O}_3$  and  $\text{MoS}_2$ . Collectively, these materials provided a wide range of catalyst properties for examination in the NBBM reaction system.

**Table 4.1** Summary of experimental plan for reaction of NBBM with solid catalytic materials.

	Temperature (°C)	Atmosphere	Time Range (Minutes)
<b>Iron Carbonyl-Based Catalyst Precursors</b>			
$\text{Fe}(\text{CO})_4\text{PPh}_3$	400	$\text{H}_2$	0-150
$\text{Fe}(\text{CO})_3(\text{PPh}_3)_2$	400, 420	$\text{N}_2, \text{H}_2$	0-150
$\text{Fe}(\text{CO})_2(\text{PPh}_3)_2\text{CS}_2$	400	$\text{H}_2$	0-150
<b>Transition Metal Catalysts and Catalyst Precursors</b>			
$\text{Fe}(\text{CO})_5$	400	$\text{H}_2$	0-90
$\text{Mo}(\text{CO})_6$	400	$\text{H}_2$	0-90
$\text{Mn}_2(\text{CO})_{10}$	400	$\text{H}_2$	0-90
$\text{Fe}_2\text{O}_3$	400	$\text{H}_2$	0-90
$\text{MoS}_2$	400	$\text{H}_2$	0-90

#### 4.1.1 Experimental Methods

NBBM (TCI Americas), dichloromethane (Fisher Scientific) and all other chemicals (Aldrich Chemical Company) were used as received. Reactions were carried out in 7 ml stainless steel microbatch reactors. The reactants and catalyst precursor were placed in an open 10 x 75 mm glass tube within the reactor to prevent



wall interactions. The loadings of NBBM and the catalysts and catalyst precursors are summarized in Table 4.2. The iron carbonyl-based catalyst precursors were loaded to achieve a 0.014 molar ratio of iron to NBBM and the transition metal catalysts were loaded to achieve a 0.025 molar ratio of metal to NBBM.

All reactions took place under 1000 psig (cold) pressure. The loaded reactor was pressurized to 1000 psig, with either nitrogen or hydrogen, and then discharged three times prior to heat up. This ensured reaction in the absence of air. The reactor was then plunged into a fluidized sand bath at the appropriate temperature, and, after the passage of the reaction time, removed from the sandbath for cooling in an ice bath for at least 30 minutes. A measured amount of biphenyl was then added to the contents of the glass tube, which was subsequently diluted with dichloromethane. The mixture was then separated in a Hewlett-Packard 5890 Gas Chromatograph with Flame Ionization Detector and a Hewlett-Packard 5890 Gas Chromatograph with a Hewlett-Packard 5970 Mass Selective Detector. Both Gas Chromatographs used Hewlett-Packard Ultra 2 columns (crosslinked 5% Ph Me Silicone) with dimensions 50 m x 0.2 mm and 0.33  $\mu\text{m}$  film thickness. The preparation of the iron carbonyl-based catalytic materials has been described elsewhere (Walter et al., 1994b), whereas the transition metal-based catalytic materials were purchased and used as received (Aldrich).

**Table 4.2** Summary of reactant loadings for catalytic reactions of NBBM.

Catalyst / Precursor	NBBM Loading (mg)	Catalyst Loading (mg)
$\text{Fe}(\text{CO})_4\text{PPh}_3$	50	5.0
$\text{Fe}(\text{CO})_3(\text{PPh}_3)_2$	50	8.0
$\text{Fe}(\text{CO})_2(\text{PPh}_3)_2\text{CS}_2$	50	8.3
$\text{Fe}(\text{CO})_5$	100	8.8
$\text{Mo}(\text{CO})_6$	100	11.8
$\text{Mn}_2(\text{CO})_{10}$	100	8.7
$\text{Fe}_2\text{O}_3$	100	3.6
$\text{MoS}_2$	100	7.2



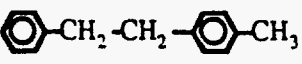

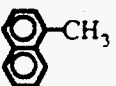
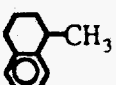
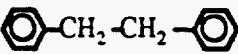
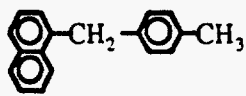
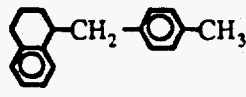
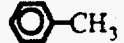
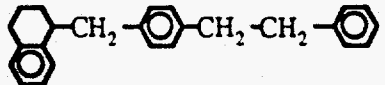
#### 4.2 Reaction Results

The reactions of NBBM were studied at 400 °C and 420 °C under 1000 psig (cold) hydrogen pressure in the presence of a set of iron-carbonyl based catalyst precursors ( $\text{Fe}(\text{CO})_4\text{PPh}_3$ ,  $\text{Fe}(\text{CO})_3(\text{PPh}_3)_2$ , and  $\text{Fe}(\text{CO})_2(\text{PPh}_3)_2\text{CS}_2$ ), in the presence of a set of transition metal-based catalytic materials ( $\text{Fe}(\text{CO})_5$ ,  $\text{Mo}(\text{CO})_6$ ,  $\text{Mn}_2(\text{CO})_{10}$ ,  $\text{Fe}_2\text{O}_3$ , and  $\text{MoS}_2$ ) and also in the absence of a catalyst. The amount of hydrogen gas present afforded an excess of 100 moles of  $\text{H}_2$  per mole of NBBM. This large excess of hydrogen pressure made any pressure changes inside the reactors due to hydrogen consumption or formation of gases due to the decomposition of the catalyst precursors negligible.

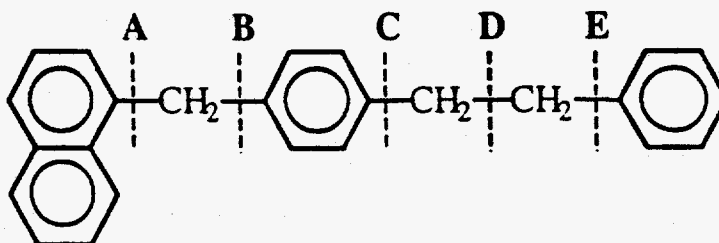
The products formed from the catalytic reaction of NBBM were the same for all of the catalytic materials examined. They are listed in Table 4.3. The main products may be summarized by the following product lumps: bond A scission

**Table 4.3** Summary of the major reaction products from NBBM catalysis under hydrogen.

**Major Reaction Products from NBBM Catalysis in Hydrogen**

Naphthalene	
Tetralin	
Methylbibenzyl	
p-Xylene	
Methylnaphthalene	
Methyltetralin	
Bibenzyl	
Naphthyltolylmethane	
Tetrahydronaphthyltolylmethane	
Toluene	
Tetrahydro-NBBM	

products, bond B scission products, bond D scission products and NBBM hydrogenation products. The scission products refer to products formed through the scission of NBBM at the bonds indicated in Figure 4.1. Thus, bond A scission products include naphthalene and its hydrogenated form tetralin, and methylbibenzyl and its secondary product p-xylene; bond B scission products include methylnaphthalene and its hydrogenated form methyltetralin, and bibenzyl; bond D scission products include naphthyltolylmethane and its hydrogenated form tetrahydronaphthyltolylmethane, and toluene; and NBBM hydrogenation products include the hydrogenated form of NBBM, tetrahydro-NBBM. All four of these product lumps were observed, with bond B scission products being present in lesser yields than the other three. In addition, bond D is a weak bibenzyl linkage, and it is expected that thermal fission of bond D would contribute significantly to the product spectra under the reaction conditions employed.



**Figure 4.1** The structure of the coal model compound 4-(1-naphthylmethyl)-bibenzyl (NBBM). The scissile bonds are labeled A through E.

The observed product spectra suggested a simple reaction network that governed the catalytic reaction of NBBM. Figure 4.2 summarizes this network in terms of the three main product lumps: bond A scission products, bond D scission products and NBBM hydrogenation products. The network also includes an "other products" lump, which

accounts for identified products that do not fall into the main products lumps mentioned above as well as products not identified through gas chromatography, e.g., gases and high molecular weight products. Two additional product classes account for secondary reactions to hydrogenated versions of products attributed to bond A and bond D scission. This reaction network will serve as a useful device with which to examine the relative contributions to the product lumps of different catalytic materials.

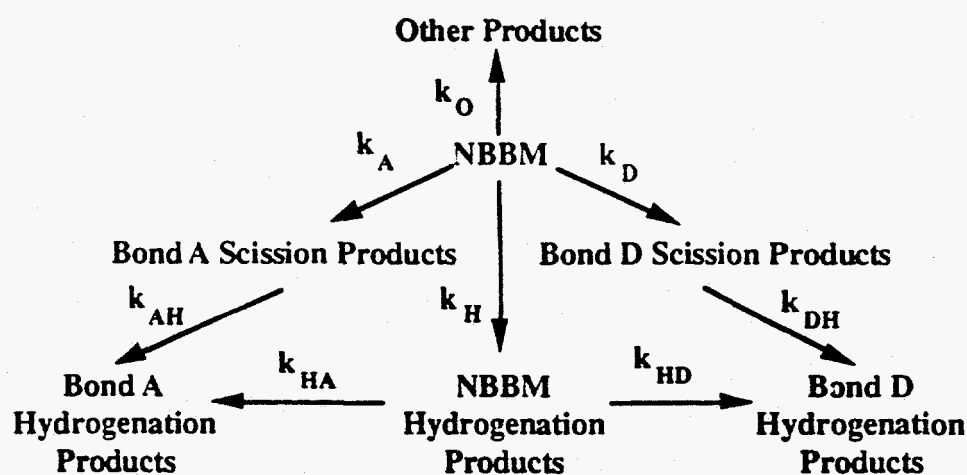
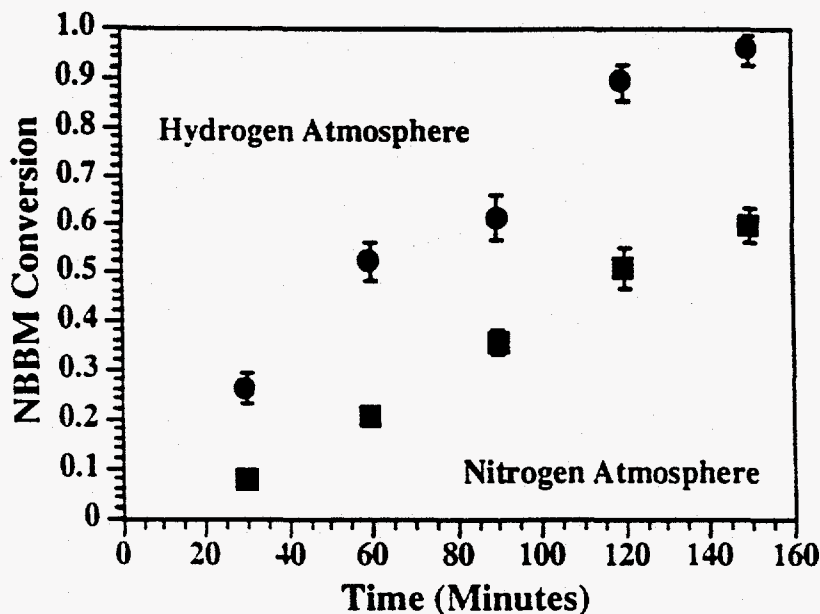


Figure 4.2 Lumped reaction network describing NBBM catalysis at 400 °C.

#### 4.2.1 NBBM Reaction in the Presence of $\text{Fe}(\text{CO})_3(\text{PPh}_3)_2$ at 420 °C under a Hydrogen or Nitrogen Atmosphere

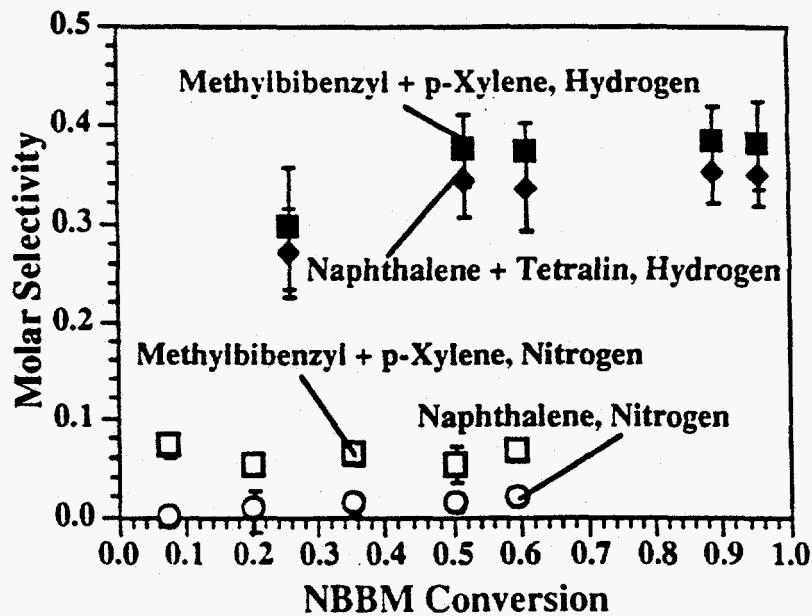
The disappearance kinetics for NBBM reaction in the presence of  $\text{Fe}(\text{CO})_3(\text{PPh}_3)_2$ , under a hydrogen and a nitrogen atmosphere, are shown in Figure 4.3. Reaction in the presence of hydrogen and the catalyst precursor revealed an accelerated disappearance of NBBM relative to the thermal background (no catalyst, nitrogen atmosphere), whereas reaction in the presence of nitrogen and the catalyst precursor yielded identical results to the thermal background. In short, the catalyst

precursor enhanced the rate of disappearance of NBBM only in the presence of hydrogen at 420 °C .



**Figure 4.3** Effect of atmosphere on NBBM conversion for reaction in the presence of the iron carbonyl-based catalyst precursor  $\text{Fe}(\text{CO})_3(\text{PPh}_3)_2$  at 420 °C. The error bars represent two standard deviations as obtained from repeated experiments.

Reactions in the presence of the catalytic precursor  $\text{Fe}(\text{CO})_3(\text{PPh}_3)_2$  under both nitrogen and hydrogen atmospheres revealed the product lumps discussed above. Figure 4.4 shows that, for catalytic reaction under nitrogen, methyl bibenzyl was a primary product, whereas naphthalene was a higher-rank product. In the presence of hydrogen, these bond A products were both primary and stoichiometric, with higher selectivities than observed in the presence of nitrogen. This suggests that the presence of the catalyst precursor and hydrogen introduced a new primary pathway effecting the scission of bond A.



**Figure 4.4** Selectivity versus Conversion for NBBM reaction in the presence of the iron carbonyl-based catalyst precursor  $\text{Fe}(\text{CO})_3(\text{PPh}_3)_2$  at  $420^\circ\text{C}$ . The error bars represent two standard deviations as obtained from repeated experiments.

There are several observations in support of this new pathway. Figure 4.5, for example, shows that the stoichiometry for the bond A products observed for catalysis under hydrogen is consistent with simple hydrogenolysis of the naphthyl-alkyl bond. The summed molar yield of methyl bibenzyl plus its derivative, p-xylene, was identical, within experimental error, to the molar yield of naphthalene plus its hydrogenation product tetralin. In addition, the observed Bond A scission is primarily responsible for the difference in NBBM conversion between catalysis under hydrogen and catalysis under nitrogen, suggesting that the catalytic material is highly selective for effecting bond A scission.

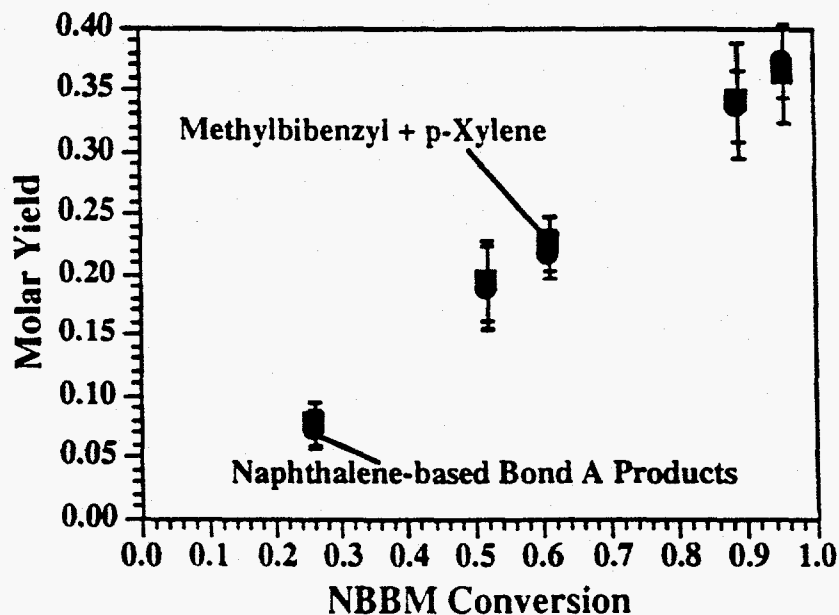


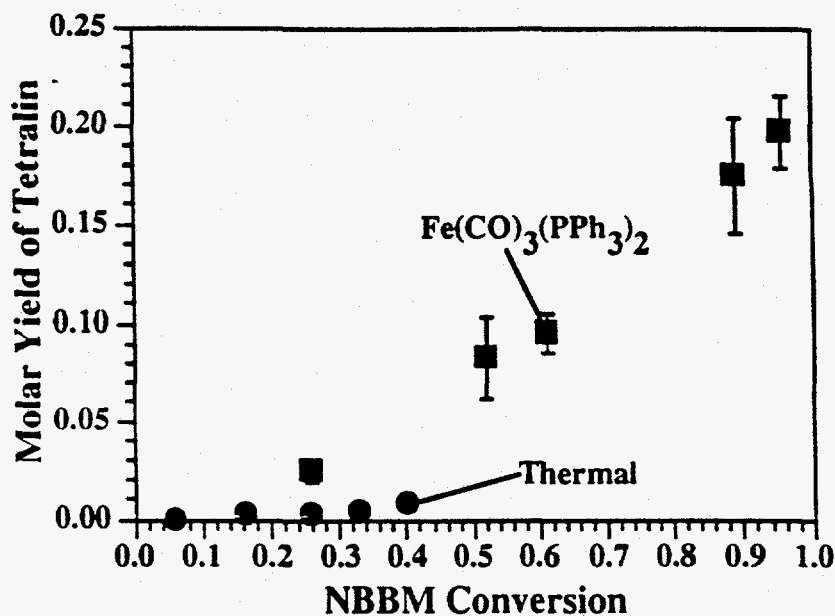
Figure 4.5 Yield versus NBBM conversion for bond A scission products produced during reaction in the presence of  $\text{Fe}(\text{CO})_3(\text{PPh}_3)_2$  at  $420^\circ\text{C}$ . The error bars represent two standard deviations as obtained from repeated experiments.

The clean selectivity for bond A cleavage observed from catalytic reaction in hydrogen suggests that a mechanism involving H atom ipso substitution is operative. Dissociation of  $\text{H}_2$  gas on the metal surface, followed by interaction of the metal bound hydrogen species with the aromatic system of the naphthalene in NBBM, would yield the observed results. The adsorption of NBBM onto the metal surface could facilitate insertion of a hydrogen atom into the naphthalene ring at the ipso position. The NBBM-hydrogen bound intermediate could then undergo a  $\beta$ -scission reaction to form a desorbed naphthalene species and a methyl bibenzyl radical. The adsorbed naphthalene complex could then desorb to naphthalene and free iron.

Further H atom addition to the adsorbed naphthalene species could result in formation of tetralin. This was observed experimentally, as summarized in Figure



4.6, which shows the large increase in the selectivity to tetralin observed from catalytic reaction in hydrogen compared to hydrolysis.

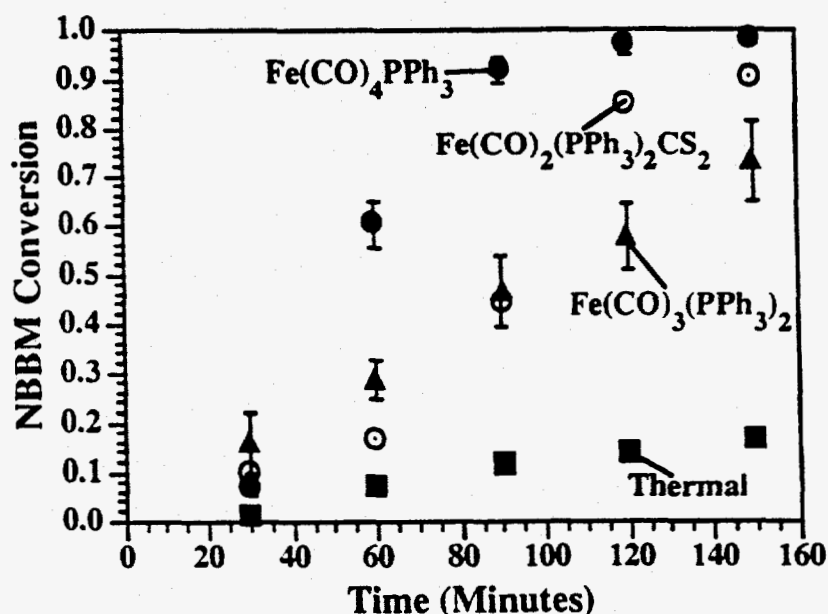


**Figure 4.6** Comparison of tetralin yields between NBBM catalysis and pyrolysis at 420 °C under a hydrogen atmosphere. The error bars represent two standard deviations as obtained from repeated experiments.

#### 4.2.2 NBBM Reaction in the Presence of $\text{Fe}(\text{CO})_2\text{PPh}_3$ , $\text{Fe}(\text{CO})_3(\text{PPh}_3)_2$ , and $\text{Fe}(\text{CO})_2(\text{PPh}_3)_2\text{CS}_2$ at 400 °C under a Hydrogen Atmosphere

The effects of precursor ligands was sought through the reaction of NBBM in the presence of a series of substituted iron-carbonyl catalyst precursors. Quantitative kinetics at 400 °C under a hydrogen atmosphere are examined at the level of the overall lumped reaction network. This information helps provide insight into the catalytic cycle that inserts the catalytically bound hydrogen into the naphthalene ring leading to bond A scission and/or hydrogenation. Both of these views will be used to guide the discussion.

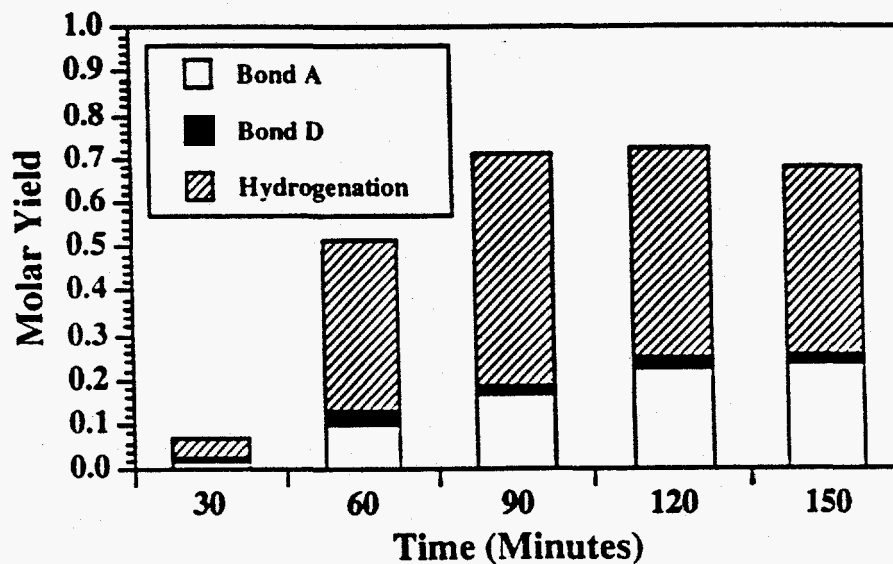
The disappearance kinetics shown in Figure 4.7 reveal that the three catalyst precursors had significant activity above the thermal baseline for the disappearance of NBBM.  $\text{Fe}(\text{CO})_4\text{PPh}_3$  led to the highest conversion over most of the reaction times. Conversion in the presence of  $\text{Fe}(\text{CO})_2(\text{PPh}_3)_2\text{CS}_2$  was initially lower than in the presence of  $\text{Fe}(\text{CO})_3(\text{PPh}_3)_2$ , but by 60 minutes the trend had reversed.



**Figure 4.7** Disappearance kinetics for NBBM reaction at 400 °C in the presence of the iron carbonyl-based catalyst precursors:  $\text{Fe}(\text{CO})_4\text{PPh}_3$ ,  $\text{Fe}(\text{CO})_3(\text{PPh}_3)_2$ , and  $\text{Fe}(\text{CO})_2(\text{PPh}_3)_2\text{CS}_2$ . The error bars for the  $\text{Fe}(\text{CO})_4\text{PPh}_3$  and  $\text{Fe}(\text{CO})_3(\text{PPh}_3)_2$  data series represent two standard deviations as obtained from repeated experiments.

Figures 4.8, 4.9 and 4.10 illustrate the time dependence of the yields of the three product classes—bond A scission, bond D scission and hydrogenation products—for reaction in the presence of each of the three catalyst precursors. Note that thermal reactions contributed less than 5% of the yields shown in Figures 4.8-4.10 for the catalytic reactions. The predominant activity for bond A scission and NBBM

hydrogenation is clear. The stoichiometry for bond A scission during reaction with each of the three catalyst precursors at 400 °C was consistent with the results discussed earlier. Ipso-substitution by hydrogen species, in addition to the thermal reactions, can account for the observed product distributions.



**Figure 4.8** Molar yields of NBBM product classes for reaction with  $\text{Fe}(\text{CO})_4\text{PPh}_3$  at 400 °C.

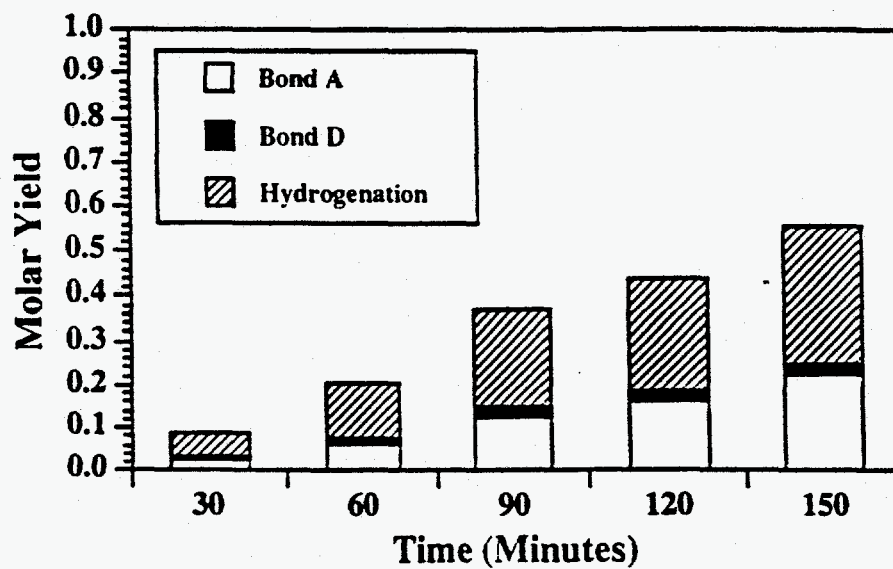


Figure 4.9 Molar yields of NBBM product classes for reaction with  $\text{Fe}(\text{CO})_3(\text{PPh}_3)_2$  at  $400^\circ\text{C}$ .

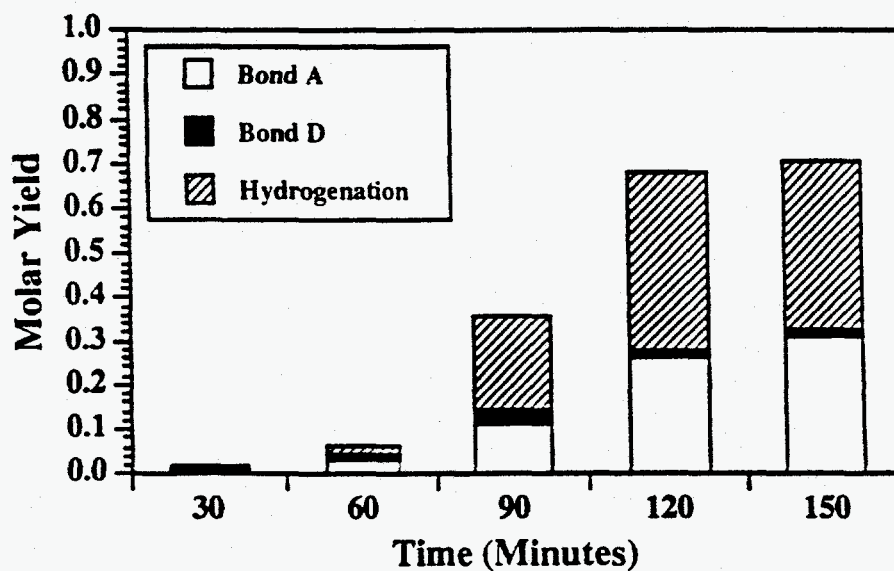
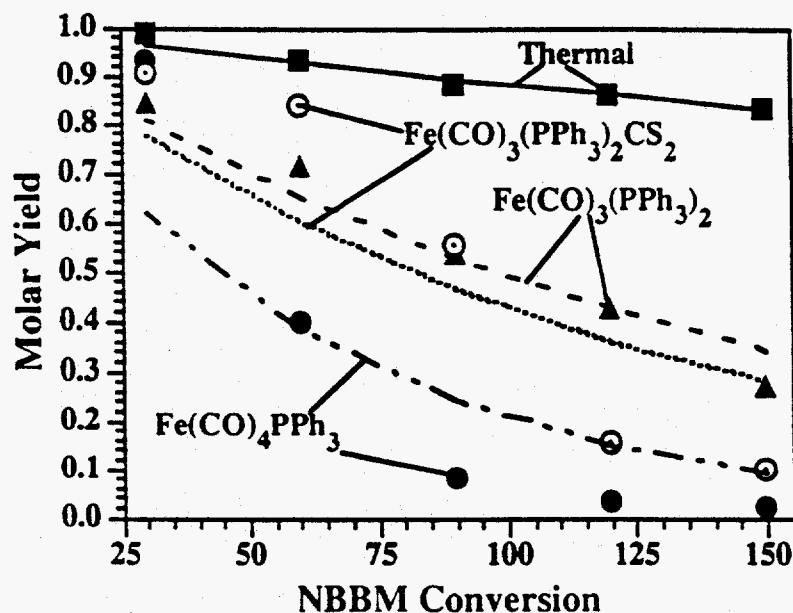


Figure 4.10 Molar yields of NBBM product classes for reaction with  $\text{Fe}(\text{CO})_2-(\text{PPh}_3)_2\text{CS}_2$  at  $400^\circ\text{C}$ .

Quantitative kinetics analysis was accomplished by representing the observed product spectra in terms of the simple reaction network of Figure 4.2. Using simple first-order kinetics to organize these data, the network predictions were regressed to the experimental data by optimizing the values of the rate constants. Table 4.4 contains the best-fit values of first-order rate constants obtained by parameter estimation using the MLSL global optimization routine (Stark, 1993). Model predictions and the experimental data for NBBM consumption are shown in Figure 4.11. The fits are good for hydrolysis and reaction in the presence of  $\text{Fe}(\text{CO})_3(\text{PPh}_3)_2$ . However, for reaction in the presence of  $\text{Fe}(\text{CO})_4\text{PPh}_3$  and  $\text{Fe}(\text{CO})_2(\text{PPh}_3)_2\text{CS}_2$  the fits are poorer, due to highly non-first order behavior, possibly due to induction periods for catalyst activity.

**Table 4.4** Regressed values for the first-order rate constants for the reaction network of Figure 4.2.

	$(k_i / \text{s}^{-1}) \times 10^5$							
	$k_A$	$k_B$	$k_D$	$k_{AB}$	$k_{DB}$	$k_{BA}$	$k_{BD}$	$k_O$
Thermal	0.38	0.12	0.46	0.00	1.87	46.15	0.00	1.10
$\text{Fe}(\text{CO})_4\text{PPh}_3$	3.42	15.61	0.26	43.45	42.72	2.36	0.00	7.19
$\text{Fe}(\text{CO})_3(\text{PPh}_3)_2$	2.32	5.29	0.47	10.52	6.47	0.00	0.00	3.71
$\text{Fe}(\text{CO})_2(\text{PPh}_3)_2\text{CS}_2$	3.93	6.23	0.10	19.00	0.58	0.00	0.00	4.16



**Figure 4.11** Model fits for the lumped network describing the reaction of NBBM at 400 °C under 1000 psig  $\text{H}_2$  (cold) in the presence of iron carbonyl based catalyst precursors. The lines are the predicted curves and the points are the experimentally measured values.

The rate constants provide insight into the underlying reaction mechanism. First, the bond D scission rate constants,  $k_D$ , are independent of the presence of the three catalysts and were all at the value observed for thermal reaction, suggesting that bond D scission is purely thermal and is unaffected by the presence of a catalyst. Second, while the values for the bond A scission constants,  $k_A$ , are similar for reaction with each of the three catalysts, they are quite different from that for thermal reaction, suggesting that a single mechanism is responsible for the bond A scission in the presence of the three catalyst precursors. Third, the values of the hydrogenation constants,  $k_H$ , reflect the higher hydrogenation activity observed for  $\text{Fe}(\text{CO})_4\text{PPh}_3$  than for  $\text{Fe}(\text{CO})_3(\text{PPh}_3)_2$  or  $\text{Fe}(\text{CO})_2(\text{PPh}_3)_2\text{CS}_2$ , suggesting that one role that the catalyst precursors' ligands play is to poison the hydrogenation activity of the ultimate

catalytic material. This could be accomplished through poisoning of the iron metal, providing fewer active sites for hydrogen adsorption and also by decreasing hydrogen mobility throughout the metal particle, thus preventing hydrogen from reaching the adsorbed naphthalene moiety. Fourth, the slower cleavage of bond A in hydrogenated NBBM relative to that for NBBM is reflected in the relationship  $k_{HA} < k_A$  for all three catalyst precursors. This reinforces the ipso substitution mechanism as operative, as the destruction of the electron-rich naphthalene system both decreases the molecule's ability to interact with the catalyst and removes the electronic topology required for ipso-substitution. Finally, all three catalyst precursors showed higher activity for hydrogenation of naphthalene ( $k_{AH}$ ) than for hydrogenation of the substituted naphthalene ( $k_H$ ), suggesting that the bare naphthalene molecules may be more easily adsorbed onto the metal surface than the bulky NBBM molecules.

The known activity of reduced iron as an effective hydrogenation catalyst also provides information about the likely mechanism. Hydrogenation catalysts are effective due to their ability to dissociate, and thus activate, molecular hydrogen. In addition, metal catalysts are also known for their ability to adsorb electron rich aromatic rings. Accordingly, the present catalyst systems likely dissociate hydrogen into atoms that can, in turn, add to adsorbed naphthyl moieties. When a hydrogen inserts at the ipso position, a thermochemically favorable  $\beta$ -scission pathway affords naphthalene and a methylbibenzyl radical. Hydrogen insertion at nonipso positions of naphthalene moieties could then lead to continued addition of hydrogen, effecting deep hydrogenation of the aromatic. This reaction cycle involving metallic iron as the active catalytic species is consistent with all of the experimental observations.

The differences in activity among the catalyst precursors may be attributed to their level of inorganic substitution. The catalyst precursors have different thermal

stabilities, and decompose on a time scale that is shorter but measurable relative to the disappearance of NBBM at 400 °C. That is, the induction periods observed in Figure 4.7 for the disappearances of NBBM suggest that the catalytically active state of the iron is not formed spontaneously under reaction conditions. The induction periods may well be the time necessary for reduction of the initial decomposition products to the active metallic iron in the hydrogen atmosphere. The type and number of inorganic substituents can contribute to the length of the induction period and the ultimate amount of the active reduced iron formed.

To this end, decomposition studies of the  $\text{Fe}(\text{CO})_4\text{PPh}_3$  catalyst precursor show that the thermal decomposition proceeds through a disproportionation pathway which produces one mole of metallic iron and one mole of  $\text{Fe}(\text{CO})_3(\text{PPh}_3)_2$  (Casey, in preparation). This initial formation of metallic iron would explain the short induction period and high initial activity observed for the  $\text{Fe}(\text{CO})_4\text{PPh}_3$  catalyst precursor in the NBBM system. Similarly, due to the presence of sulfur in the  $\text{Fe}(\text{CO})_2(\text{PPh}_3)_2\text{CS}_2$  catalyst precursor, initial decomposition pathways likely lead to a relatively stable iron sulfide structure. This structure would yield a longer induction period for the iron sulfide to be reduced to metallic iron and hydrogen sulfide under reaction conditions. However, once the reduced iron phase is formed, its activity is similar to that for the  $\text{Fe}(\text{CO})_4\text{PPh}_3$  catalyst precursor. This is consistent with the trends observed in Figures 4.8-4.10.

#### 4.2.3 NBBM Reaction in the Presence of $\text{Fe}(\text{CO})_5$ , $\text{Mo}(\text{CO})_6$ , $\text{Mn}_2(\text{CO})_{10}$ , $\text{Fe}_2\text{O}_3$ , and $\text{MoS}_2$ at 400 °C under a Hydrogen Atmosphere

Reactions of NBBM at 400 °C in hydrogen were carried out with the series of transition metal catalysts:  $\text{Fe}(\text{CO})_5$ ,  $\text{Mo}(\text{CO})_6$ ,  $\text{Mn}_2(\text{CO})_{10}$ ,  $\text{Fe}_2\text{O}_3$  and  $\text{MoS}_2$ . The transition metal carbonyl materials, namely  $\text{Fe}(\text{CO})_5$ ,  $\text{Mo}(\text{CO})_6$  and  $\text{Mn}_2(\text{CO})_{10}$ , all



degraded quickly at the reaction conditions to form metal particles. Note that this was also observed for the iron carbonyl materials. Figure 4.12 shows that all the catalytic materials significantly increased the rate of NBBM disappearance, with the exception of  $\text{Mn}_2(\text{CO})_{10}$ , which showed no increase over the thermal baseline. Since the  $\text{Mn}_2(\text{CO})_{10}$ -catalyzed reaction showed no activity over the thermal baseline in any aspect, it provided no basis for further analysis.

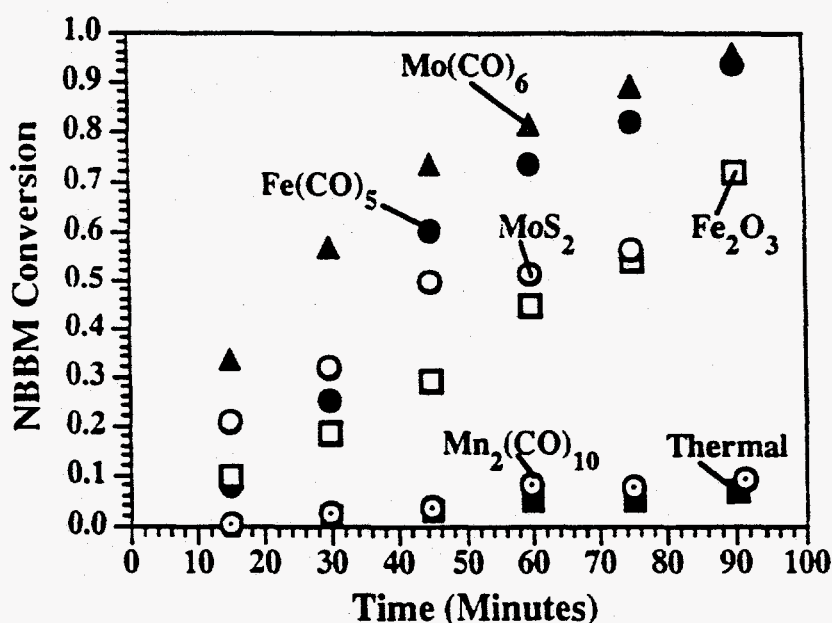


Figure 4.12 NBBM disappearance kinetics for reaction in the presence of the transition metal-based catalysts.

The transition metal catalysts showed activity for bond scission (bond A and bond B) and for hydrogenation of the naphthalene group. In this respect, they were similar to the iron carbonyl-based catalyst precursors. Bond A scission is represented in Figure 4.13 by the sum of the molar yields of naphthalene and tetralin. The activity for bond A cleavage ordered  $\text{MoS}_2 > \text{Mo}(\text{CO})_6 > \text{Fe}_2\text{O}_3 > \text{Fe}(\text{CO})_5$ , with

the molybdenum compounds showing significantly higher selectivities than the iron compounds. Figure 4.14 shows a similar trend for bond B cleavage. As with bond A cleavage, the molybdenum compounds were more selective to bond B cleavage than the iron compounds.

Hydrogenation of the naphthyl group to a tetrahydronaphthyl group showed the reversed ordering, i.e., the order was inverted from that shown for bond A cleavage. This is illustrated in Figure 4.15. The activity towards naphthyl hydrogenation aligned as  $\text{Fe}(\text{CO})_5 > \text{Fe}_2\text{O}_3 > \text{Mo}(\text{CO})_6 > \text{MoS}_2$ , with  $\text{MoS}_2$  exhibiting virtually no hydrogenation activity. The  $\text{Fe}(\text{CO})_5$  material had high enough hydrogenation activity as to enable hydrogenation of the phenyl rings of NBBM and the tetralin phenyl groups to produce decahydronaphthyl groups (in small quantities). Moreover, the catalysts examined show a range of activities for both hydrogenation and bond cleavage.

The simple reaction network of Figure 4.2 is useful for summarizing these reactivity trends. Table 4.5 lists the best-fit values of the first-order rate constants associated with the reaction network for the transition metal series of catalysts. As with the iron carbonyl-based catalyst precursors, the rate constant for bond D scission,  $k_D$ , was the same for all catalysts. This is strictly a thermal reaction. The ordering for NBBM hydrogenation rate constants,  $k_H$ , was  $\text{Fe}(\text{CO})_5 > \text{Mo}(\text{CO})_6 > \text{Fe}_2\text{O}_3 > \text{MoS}_2$  whereas the observed hydrogenation product formation ordering was  $\text{Fe}(\text{CO})_5 > \text{Fe}_2\text{O}_3 > \text{Mo}(\text{CO})_6 > \text{MoS}_2$ . This apparent discrepancy may be explained by the activity of  $\text{Mo}(\text{CO})_6$  for competing reactions. For example it had a high rate of bond A scission, so the concentration of NBBM in the  $\text{Mo}(\text{CO})_6$  system dropped not only due to hydrogenation but other reactions. This caused the  $\text{Mo}(\text{CO})_6$  rate of hydrogenation to

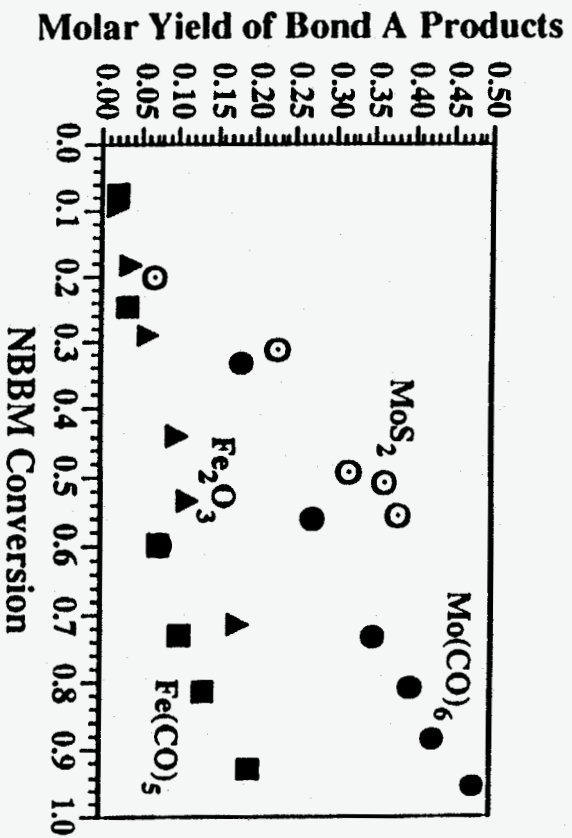


Figure 4.13 Molar yield of bond A scission products (naphthalene + tetralin) as a function of NBBM conversion for NBBM reaction with Fe(CO)<sub>5</sub>, Mo(CO)<sub>6</sub>, Fe<sub>2</sub>O<sub>3</sub> and MoS<sub>2</sub> catalytic materials.

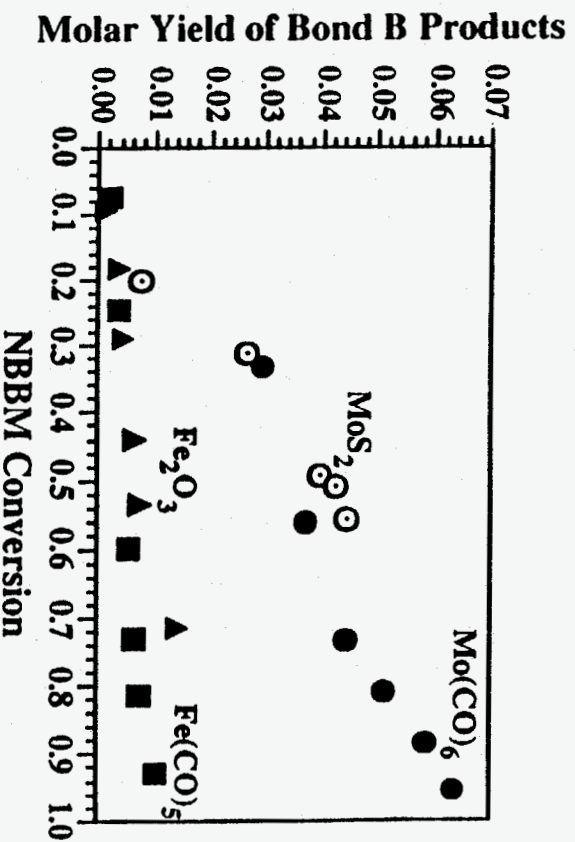


Figure 4.14 Molar yield of bond B scission products (methylnaphthalene + methyltetralin) as a function of NBBM conversion for NBBM reaction with Fe(CO)<sub>5</sub>, Mo(CO)<sub>6</sub>, Fe<sub>2</sub>O<sub>3</sub> and MoS<sub>2</sub> catalytic materials.

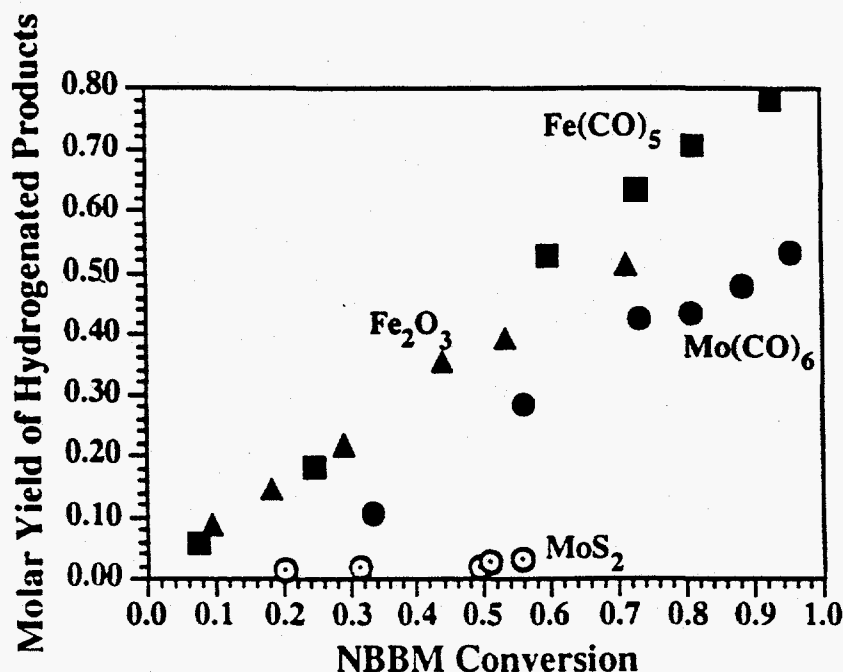


Figure 4.15 Molar yield of naphthyl hydrogenation products (naphthalene + tetralin) as a function of NBBM conversion for NBBM reaction with  $\text{Fe}(\text{CO})_5$ ,  $\text{Mo}(\text{CO})_6$ ,  $\text{Fe}_2\text{O}_3$  and  $\text{MoS}_2$  catalytic materials.

be slower than for reaction with  $\text{Fe}_2\text{O}_3$  even though  $\text{Mo}(\text{CO})_6$  has the higher rate constant. Similarly, the bond A scission rate constants,  $k_A$ , were ordered  $\text{Mo}(\text{CO})_6 > \text{MoS}_2 > \text{Fe}(\text{CO})_5 > \text{Fe}_2\text{O}_3$  whereas the observed yields of bond A scission products were ordered  $\text{MoS}_2 > \text{Mo}(\text{CO})_6 > \text{Fe}_2\text{O}_3 > \text{Fe}(\text{CO})_5$ . Again, this was due to the alternative pathways in the reaction network, which was thus able to decouple the concentration effects from the catalysts' intrinsic activities for the different observed reaction families.

These observed trends for bond cleavage and hydrogenation activities suggest a qualitative picture of the role of the catalyst in the reaction of NBBM. Common is the notion of a metal surface containing adsorbed NBBM molecules and hydrogen atoms. If the metal surface has a threshold hydrogenation activity, then a

hydrogen atom may be inserted in the naphthyl group of the NBBM molecule. If the hydrogenation activity of the metal is higher yet, then subsequent hydrogen additions will lead to the tetrahydro-NBBM product, which cannot subsequently undergo catalytic bond A scission. However, if the first hydrogen atom addition occurs at the ipso position, and the hydrogenation activity is not as great, then the complex can undergo bond A scission leading to naphthalene and a methylbibenzyl radical (or adsorbed species). This scenario would explain why a very strong hydrogenation catalyst would have a lower selectivity to bond cleavage ( $\text{Fe}(\text{CO})_5$ ), and a catalyst with no hydrogenation ability would also have no bond cleavage activity ( $\text{Mn}_2(\text{CO})_{10}$ ).

**Table 4.5** Regressed values for the first-order rate constants for the reaction network of Figure 4.2.

	$(k_i / \text{s}^{-1}) \times 10^5$							
	$k_A$	$k_D$	$k_B$	$k_O$	$k_{AH}$	$k_{DH}$	$k_{HA}$	$k_{HD}$
$\text{Fe}(\text{CO})_5$	5.3	1.0	22.0	32.0	99.4	47.9	0.0	0.0
$\text{Mo}(\text{CO})_6$	19.3	0.4	14.8	13.1	30.0	0.0	12.5	1.9
$\text{Mn}_2(\text{CO})_{10}$	0.6	0.5	0.5	0.0	12.8	0.0	1.9	5.5
$\text{Fe}_2\text{O}_3$	3.7	1.0	9.7	2.1	50.6	26.2	0.0	0.0
$\text{MoS}_2$	13.9	0.4	1.1	5.6	1.8	0.0	0.0	103.6

### 4.3 Summary and Conclusions

The catalytic chemistry of NBBM in the presence of various transition metal-based catalysts and catalyst precursors was examined. Reaction in the presence of  $\text{Fe}(\text{CO})_3(\text{PPh}_3)_2$  under hydrogen and nitrogen at 420 °C demonstrated that the presence of hydrogen is necessary for catalytic activity.  $\text{Fe}(\text{CO})_4\text{PPh}_3$ ,  $\text{Fe}(\text{CO})_3(\text{PPh}_3)_2$ ,  $\text{Fe}(\text{CO})_2(\text{PPh}_3)_2\text{CS}_2$ ,  $\text{Fe}(\text{CO})_5$ ,  $\text{Mo}(\text{CO})_6$ ,  $\text{Fe}_2\text{O}_3$  and  $\text{MoS}_2$  all showed significant activity for the disappearance of NBBM above the thermal baseline at 400 °C, while  $\text{Mn}_2(\text{CO})_{10}$  was inactive.

Two of the main product classes were bond A scission and NBBM hydrogenation. A simple reaction network employed to summarize the kinetics of the reaction systems indicated that for  $\text{Fe}(\text{CO})_4\text{PPh}_3$ ,  $\text{Fe}(\text{CO})_3(\text{PPh}_3)_2$  and  $\text{Fe}(\text{CO})_2(\text{PPh}_3)_2\text{CS}_2$ : bond D scission was purely thermal and unaffected by the presence of the catalyst precursors; bond A rate constants were similar for reaction in the presence of all three catalyst precursors and different from that for thermal reaction; and the hydrogenation rate constant was higher for  $\text{Fe}(\text{CO})_4\text{PPh}_3$  than for the other two catalyst precursors.

A consistent reaction mechanism involves catalytic dissociation of  $\text{H}_2$  into hydrogen atoms by the reduced metal, which are, in turn, inserted into the naphthalene system of NBBM; the naphthalene site at which the hydrogen atom is inserted determines the outcome of bond A scission or hydrogenation. The slower rate of bond A scission observed by the hydrogenated NBBM species can be qualitatively explained with decreased catalyst interaction and removal of ipso-substitution electronic topology. A scenario that relates the observed induction times for two of

the catalyst precursors to the ease of formation of a reduced iron phase is consistent with the observed trends.

Similar activities were observed for  $\text{Fe}(\text{CO})_5$ ,  $\text{Mo}(\text{CO})_6$ ,  $\text{Fe}_2\text{O}_3$ , and  $\text{MoS}_2$ . The main observed reactions were bond A scission and naphthyl hydrogenation. This series of materials had the interesting feature that as the activity for bond A scission increased, activity for naphthyl hydrogenation decreased. This suggests that high NBBM hydrogenation rates destroy possible sites for hydrogen ipso substitution, resulting in lower bond scission rates.

## REFERENCES

- Andrés, M., Charcosset, H., Chiche, P., Davignon, L., Djega-Mariadassou, G., Joly, J., Prégermain, S. (1983) "Catalysis of Coal Hydroliquefaction by Synthetic Iron Catalysts." *Fuel*, **62**, 69.
- Casey, S.M. (in preparation) *Synthesis and Characterization of Fine-Particle Unsupported Catalysts*. (Ph.D. Dissertation, University of Delaware.)
- Herrick, D.E., Tierney, J.W., Wender, I., Huffman, G.P., Huggins, F.E. (1990) "Activity and Characterization of Coprocessing Catalysts Produced from an Iron Pentacarbonyl Precursor." *Energy & Fuels*, **4**, 231.
- Huffman, G.P., Ganguly, B., Zhao, J., Rao, K.R.P.M., Shah, N., Feng, Z., Huggins, F.E., Taghiei, M.M., Lu, F., Wender, I., Pradhan, V.R., Tierney, J.W., Seehra, M.S., Ibrahim, M.M., Shabtai, J., Eyring, E.M. (1993) "Structure and Dispersion of Iron-Based Catalysts for Direct Coal Liquefaction." *Energy & Fuels*, **7**, 285.
- Pradhan, V.R., Tierney, J.W., Wender, I. (1991) "Catalysis in Direct Coal Liquefaction by Sulfated Metal Oxides." *Energy & Fuels*, **5**, 497.
- Pradhan, V.R., Holder, G.D., Wender, I., Tierney, J.W. (1992) "Kinetic Modeling of Direct Liquefaction of Wyodak Coal Catalyzed by Sulfated Iron Oxides." *Ind. Eng. Chem. Res.*, **31**, 2051.
- Prégermain, S. (1985) "Disposable Catalysts in One-Stage Coal Liquefaction." *Proceedings: International Conference on Coal Science*, 189.
- Stark, S.M. (1993) *An Investigation of the Applicability of Parallel Computation to Demanding Chemical Engineering Problems*. (Ph.D. Dissertation, University of Delaware.)
- Takemura, Y., Shibaoka, M., Yamada, T. (1985) "Behavior of Iron Catalysts During Coal Hydrogenation." *Proceedings: International Conference on Coal Science*, 185.
- Walter, T.D., Casey, S.M., Klein, M.T., Foley, H.C., "Reaction of 4-(Naphthylmethyl)bibenzyl, Thermally and in the Presence of  $\text{Fe}(\text{CO})_3(\text{PPh}_3)_2$ ," *Catalysis Today*, 1994a, **19**, 367.



Walter, T.D., Casey, S.M., Klein, M.T., Foley, H.C., "Effects of Iron Carbonyl-Based Catalyst Precursors on the Reaction of 4-(Naphthylmethyl)bibenzyl," *Energy & Fuels*, 1994b, 8, 470.

Watanabe, Y., Yamada, O., Fujita, K., Takegami, Y., Suzuki, T. (1984) "Coal Liquefaction Using Iron Complexes as Catalysts," *Fuel*, 63, 752.

Zhang, Z.-G., Scott, D.S., Silveston, P.L. (1994b) "Successive Pulsing of an Iron-Loaded Canadian Subbituminous Coal Char," *Energy & Fuels*, 8, 943.

## Chapter 5

### MODELING OF THE CATALYTIC CHEMISTRY OF 4-(1-NAPHTHYLMETHYL)BIBENZYL

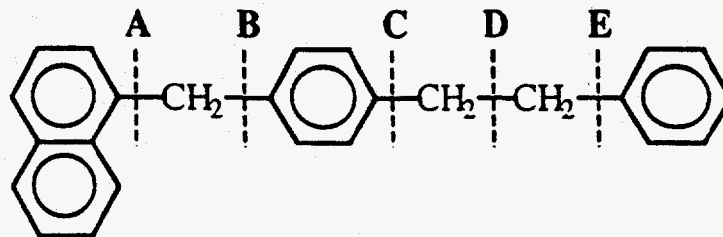
The desire for molecular level information about the composition and properties of hydrocarbon feed stocks and their reaction products has generated considerable interest in the construction of mechanistic kinetic models, even for complex feed stocks such as coal and petroleum resids. The main challenges to be overcome in mechanistic modeling derive from the complexity of accounting for large numbers of species, reactions and rate constants. To begin to resolve this conflict, a novel mechanism-based lumping scheme (Neurock and Klein, 1993) has been developed where the large number of reacting species can be broken down into a small number of reaction moieties that undergo the same chemical transformations, regardless of their degree of molecular substitution. This "reaction family" lumping approach provides, conceptually, an algorithm for the generation of appropriate mechanistic models given the initial feed composition, the contributing reaction families and rules governing the application of the reaction families.

The reaction family concept can also be employed as an aid in the estimation of model rate constants. Each reaction family can be constrained to follow a quantitative structure-reactivity relationship (QSRR), which, essentially, relates rate constant values to the molecular structure of products and reactants. Once parameterized (e.g., through model compound experiments), the QSRR allows a priori prediction of rate constants given a value for an appropriate reactivity index, which

can be estimated from the reactants' and the products' structures. The data base of QSRR parameters is thus expected to be of fundamental value, i.e., they are system independent.

Coal liquefaction and resid upgrading present special challenges due to the size of the reacting mixtures. Because of the macromolecular nature of these materials, upgrading strategies employing fine particle catalysts are of keen interest. Since catalysis is a kinetic phenomenon, it seemed cogent to use a mechanistic model to gain quantitative insight into the controlling mechanisms and allow specification of optimal catalytic materials through kinetics-assisted design. To begin to achieve this goal, a mechanistic model for the catalytic reaction of NBBM was developed with the goal of extracting catalyst-sensitive QSRR parameters that could be used for the specification of an optimal NBBM reaction catalyst. Extension of this work would allow for the kinetics-assisted design of a coal liquefaction catalyst.

NBBM is similar to coal and resids in that it is a multifunctional, low-volatility compound that mimics some of the important attributes of coal and resid, e.g., a fused aromatic moiety connected to other aromatics by short alkyl chains. The structure, shown in Figure 5.1, is simple enough, however, that the reaction products can be identified and quantified. It is noteworthy that the catalytic reaction of NBBM has been shown to be similar to coal in that catalysts which increase the rate of disappearance of NBBM also increase the rate of coal liquefaction (Linehan et al., 1993; and Guin et al., 1993).



**Figure 5.1** The structure of the coal and resid model compound 4-(1-naphthylmethyl)biphenyl (NBBM). The scissile bonds are labeled A through E.

### 5.1 Guiding Experimental Results



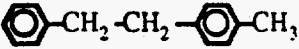

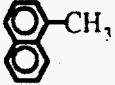
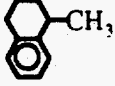
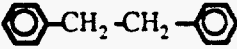
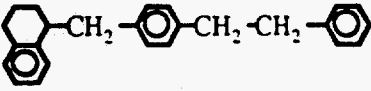
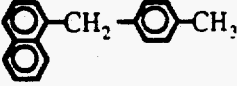
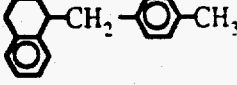
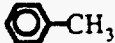
The experimental findings, discussed in Chapter 4 of this document, from the reaction of NBBM with the catalytic materials  $\text{Fe}(\text{CO})_5$ ,  $\text{Mo}(\text{CO})_6$ ,  $\text{Mn}_2(\text{CO})_{10}$ ,  $\text{Fe}_2\text{O}_3$ , and  $\text{MoS}_2$  will be used to guide the model development and attain quantitative kinetic parameters. The major products of NBBM reaction with each of these materials at 400 °C under hydrogen are listed in Table 5.1. Naphthyltolylmethane and toluene are pyrolysis products whose formation rate constants are independent of the presence of the catalyst. The formation of naphthalene and methylbiphenyl from "bond A" scission is likely the result of ipso addition of a surface hydrogen atom into the naphthalene ring of NBBM, with subsequent ejection of the methylbiphenyl radical. Tetralin and p-xylene are secondary "bond A" products that evolve from the hydrogenation of naphthalene and fission of methylbiphenyl, respectively. The less prevalent methylnaphthalene and biphenyl are likely formed from a more energetically demanding ipso substitution of hydrogen to the "B" phenyl ring of NBBM, with subsequent ejection of the methylnaphthalene radical. Methyltetralin is a hydrogenation product of methylnaphthalene. Primary hydrogenation reactions,

hydrogenation of the NBBM molecule to tetrahydro-NBBM, was also a significant catalytic reaction path.

While the reaction network seemed qualitatively independent of the identity of the catalyst, the rate of formation of the "bond A", "bond B" and NBBM hydrogenation product lumps differed among the catalytic materials. For example, the yields of the bond A scission products were highest with the molybdenum-containing compounds. Bond A scission rates aligned as  $\text{Mo}(\text{CO})_6 > \text{MoS}_2 > \text{Fe}(\text{CO})_5 > \text{Fe}_2\text{O}_3 > \text{Mn}_2(\text{CO})_{10}$ . In contrast, the yields of the NBBM hydrogenation product were highest with the iron containing compounds. A rate ranking of  $\text{Fe}(\text{CO})_5 > \text{Fe}_2\text{O}_3 > \text{Mo}(\text{CO})_6 > \text{MoS}_2 > \text{Mn}_2(\text{CO})_{10}$  was observed. The  $\text{Mn}_2(\text{CO})_{10}$  catalyst precursor showed no activity above the thermal baseline at the reaction conditions employed.

These trends for bond cleavage and hydrogenation activities suggest a selectivity tradeoff that depends on the details of the surface chemistry. In general, the metal surface will contain adsorbed NBBM molecules and hydrogen atoms. Evidently, the examined metals had sufficient hydrogenation activity for a hydrogen atom to be inserted at any position in the naphthyl group of the NBBM molecule. If the hydrogenation activity of the metal is high, then subsequent hydrogen additions will lead to tetrahydro-NBBM. Note that this hydroaromatic cannot subsequently undergo catalytic bond A scission by ipso substitution. However, if the first hydrogen atom addition occurs at the ipso position, and the hydrogenation activity is not as great, then the complex can undergo bond A scission leading to naphthalene and a methylbibenzyl radical (or adsorbed species). Overall, this scenario rationalizes why a very strong hydrogenation catalyst would have a lower selectivity to bond cleavage ( $\text{Fe}(\text{CO})_5$ ), and a catalyst with no hydrogenation ability would also have no bond cleavage activity ( $\text{Mn}_2(\text{CO})_{10}$ ).

**Table 5.1** Summary of the major reaction products from NBBM catalysis under hydrogen.**Major Reaction Products from NBBM Catalysis in Hydrogen**

Naphthalene	
Tetralin	
Methylbibenzyl	
p-Xylene	
Methylnaphthalene	
Methyltetralin	
Bibenzyl	
Tetrahydro-NBBM	
Naphthyltolylmethane	
Tetrahydronaphthyltolylmethane	
Toluene	

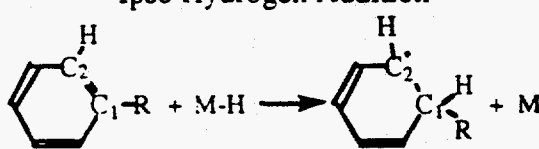
This qualitative picture of NBBM catalysis guided the construction of the mechanistic reaction model in terms of six reaction families: 1) hydrogen adsorption/desorption, 2) naphthyl adsorption/desorption, 3) ipso H atom insertion, 4) radical elimination, 5) naphthyl hydrogenation and 6) surface recombination. The bond breaking and bond making results of each of these six reaction families can be summarized concisely in terms of the formal reaction matrix (Broadbelt, 1994) for each. Mathematically, addition of the reaction matrix to the reactant matrix yields the product matrix. This is illustrated in Table 5.2 for a representative reaction of each of the reaction families.

Table 5.2 exposes the reaction matrix to be a mathematical representation of the changes in bonding which occur in molecules as they undergo reaction. Each of the rows and columns of the matrix correspond to an atom which participates in the reaction. The off-diagonal elements of the matrix represent the change in bond order of the associated atoms as a result of the reaction. The diagonal elements represent the change in number of non-bonded electrons (e.g., the formation (+1) or capping (-1) of a free radical center) associated with that atom.

### 5.1.1 Algorithm for Determining Model Reactions

The catalytic reaction steps included in the mechanistic kinetics model, and the associated FORTRAN code for the governing ordinary differential equations, were generated through exhaustive application of these reaction families to both the NBBM/H<sub>2</sub>/catalyst starting mixture and also the reaction products. The initial reactants were NBBM, H<sub>2</sub> gas and the metal.

**Table 5.2** Reaction matrices for the elementary step reaction families used in constructing the NBBM mechanistic kinetics model.

Reaction Family	Reaction Matrix
Hydrogen Adsorption $2 M + H_2 \longrightarrow 2 M-H$	$\begin{matrix} M_1 & M_2 & H_1 & H_2 \\ M_1 & \begin{bmatrix} 0 & 0 & +1 & 0 \end{bmatrix} \\ M_2 & \begin{bmatrix} 0 & 0 & 0 & +1 \end{bmatrix} \\ H_1 & \begin{bmatrix} +1 & 0 & 0 & -1 \end{bmatrix} \\ H_2 & \begin{bmatrix} 0 & +1 & -1 & 0 \end{bmatrix} \end{matrix}$
Naphthyl Adsorption $M + \text{Naph-R} \longrightarrow M\text{-Naph-R}$	$\begin{matrix} M & N \\ M & \begin{bmatrix} 0 & +1 \end{bmatrix} \\ N & \begin{bmatrix} +1 & 0 \end{bmatrix} \end{matrix}$
Ipso Hydrogen Addition 	$\begin{matrix} M & H & C_1 & C_2 \\ M & \begin{bmatrix} 0 & -1 & 0 & 0 \end{bmatrix} \\ H & \begin{bmatrix} -1 & 0 & +1 & 0 \end{bmatrix} \\ C_1 & \begin{bmatrix} 0 & +1 & 0 & -1 \end{bmatrix} \\ C_2 & \begin{bmatrix} 0 & 0 & -1 & +1 \end{bmatrix} \end{matrix}$
Radical Elimination (Reverse of Ipso Hydrogen Addition)	$\begin{matrix} M & H & C_1 & C_2 \\ M & \begin{bmatrix} 0 & +1 & 0 & 0 \end{bmatrix} \\ H & \begin{bmatrix} +1 & 0 & -1 & 0 \end{bmatrix} \\ C_1 & \begin{bmatrix} 0 & -1 & 0 & +1 \end{bmatrix} \\ C_2 & \begin{bmatrix} 0 & 0 & +1 & -1 \end{bmatrix} \end{matrix}$
Surface Recombination $M-R\cdot + M-R'\cdot \longrightarrow 2 M + R-R'$	$\begin{matrix} M_1 & M_2 & R & R' \\ M_1 & \begin{bmatrix} 0 & 0 & -1 & 0 \end{bmatrix} \\ M_2 & \begin{bmatrix} 0 & 0 & 0 & -1 \end{bmatrix} \\ R & \begin{bmatrix} -1 & 0 & -1 & +1 \end{bmatrix} \\ R' & \begin{bmatrix} 0 & -1 & +1 & -1 \end{bmatrix} \end{matrix}$
Hydrogen Desorption (Reverse of Hydrogen Adsorption)	$\begin{matrix} M_1 & M_2 & H_1 & H_2 \\ M_1 & \begin{bmatrix} 0 & 0 & -1 & 0 \end{bmatrix} \\ M_2 & \begin{bmatrix} 0 & 0 & 0 & -1 \end{bmatrix} \\ H_1 & \begin{bmatrix} -1 & 0 & 0 & +1 \end{bmatrix} \\ H_2 & \begin{bmatrix} 0 & -1 & +1 & 0 \end{bmatrix} \end{matrix}$
Naphthyl Desorption (Reverse of Naphthyl Adsorption)	$\begin{matrix} M & N \\ M & \begin{bmatrix} 0 & -1 \end{bmatrix} \\ N & \begin{bmatrix} -1 & 0 \end{bmatrix} \end{matrix}$



Dissociative adsorption of  $H_2$  and adsorption of NBBM onto the metal surface initiate this reaction scheme. The main bond breaking pathways occur through ipso substitution of catalytically bound hydrogen atoms to NBBM (or other substituted naphthalene species adsorbed on the catalyst surface) followed by radical elimination. Bound hydrogen atoms can be inserted into either naphthyl or phenyl rings, effecting bond A scission, bond B scission, bond C scission or bond E scission.

## 5.2 Model Description

The complete set of reactions is listed in Table 5.3. The reaction scheme begins with the adsorption of  $H_2$  and naphthyl containing molecules (only NBBM is present initially) on the metal surface. The allowed surface reactions leading to bond scission consist of insertion of a bound hydrogen atom at the ipso position of an adsorbed substituted naphthalene molecule. The ipso substituted intermediates then undergo bond scission to yield an adsorbed naphthalene containing fragment and a free radical. Adsorbed free radicals also may recombine. The other, non-elementary, surface pathway accomplishes insertion of four bound hydrogen atoms into an adsorbed naphthalene containing molecule. Hydrogenated products are modeled as very weakly adsorbed on the metal.

The catalytic reactions of Table 5.3 were coupled with the elementary steps for the pyrolysis background which were developed in Chapter 3 of this document to model the rate of formation of the observed product spectra. The molecularity provided the rate expression of each step, and thus, solution of this model required only further estimates of the associated rate constants.

**Table 5.3** Catalytic reactions included in the mechanistic kinetics model. M- signifies surface bound species.

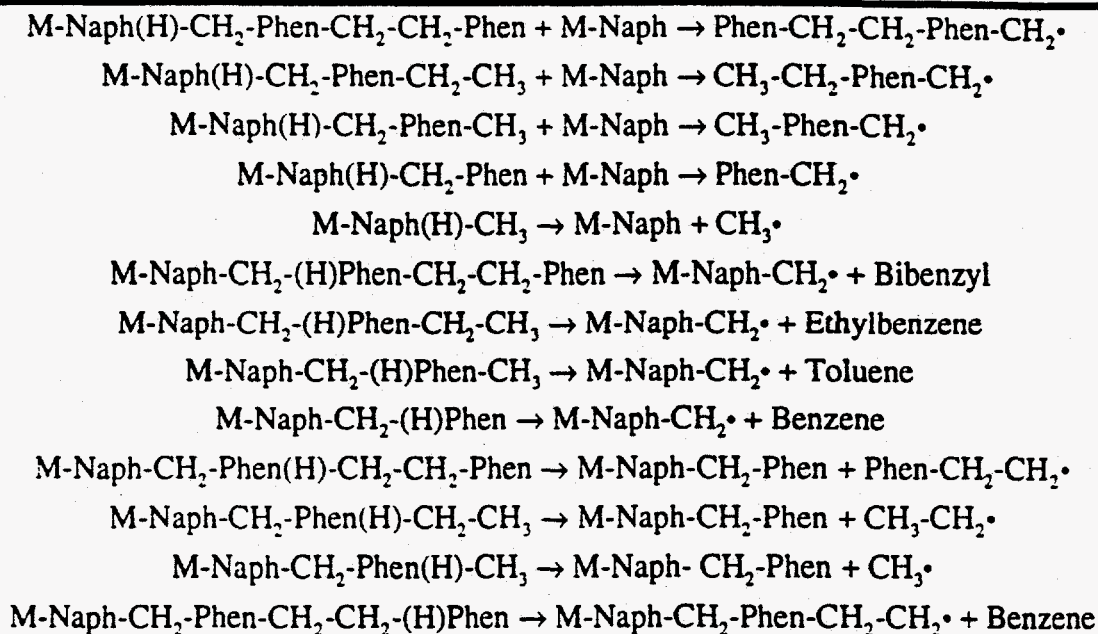
Hydrogen Adsorption Reactions
$2 M + H_2 \rightarrow 2 M-H$
Naphthyl Adsorption Reactions
$M + NBBM \rightarrow M-NBBM$
$M + \text{Naph-CH}_2\text{-Phen-CH}_2\text{-CH}_3 \rightarrow M\text{-Naph-CH}_2\text{-Phen-CH}_2\text{-CH}_3$
$M + \text{Naph-CH}_2\text{-Phen-CH}_3 \rightarrow M\text{-Naph-CH}_2\text{-Phen-CH}_3$
$M + \text{Naph-CH}_2\text{-Phen} \rightarrow M\text{-Naph-CH}_2\text{-Phen}$
$M + \text{Naph-CH}_3 \rightarrow M\text{-Naph-CH}_3$
$M + \text{Naph} \rightarrow M\text{-Naph}$
H Atom Ipso Insertion Reactions
$M-H + M-NBBM \rightarrow M\text{-Naph(H)-CH}_2\text{-Phen-CH}_2\text{-CH}_2\text{-Phen}$
$M-H + M\text{-Naph-CH}_2\text{-Phen-CH}_2\text{-CH}_3 \rightarrow M\text{-Naph(H)-CH}_2\text{-Phen-CH}_2\text{-CH}_3$
$M-H + M\text{-Naph-CH}_2\text{-Phen-CH}_3 \rightarrow M\text{-Naph(H)-CH}_2\text{-Phen-CH}_3$
$M-H + M\text{-Naph-CH}_2\text{-Phen} \rightarrow M\text{-Naph(H)-CH}_2\text{-Phen}$
$M-H + M\text{-Naph-CH}_3 \rightarrow M\text{-Naph(H)-CH}_3$
$M-H + M-NBBM \rightarrow M\text{-Naph-CH}_2\text{-(H)Phen-CH}_2\text{-CH}_2\text{-Phen}$
$M-H + M\text{-Naph-CH}_2\text{-Phen-CH}_2\text{-CH}_3 \rightarrow M\text{-Naph-CH}_2\text{-(H)Phen-CH}_2\text{-CH}_3$
$M-H + M\text{-Naph-CH}_2\text{-Phen-CH}_3 \rightarrow M\text{-Naph-CH}_2\text{-(H)Phen-CH}_3$
$M-H + M\text{-Naph-CH}_2\text{-Phen} \rightarrow M\text{-Naph-CH}_2\text{-(H)Phen}$
$M-H + M-NBBM \rightarrow M\text{-Naph-CH}_2\text{-Phen(H)-CH}_2\text{-CH}_2\text{-Phen}$
$M-H + M\text{-Naph-CH}_2\text{-Phen-CH}_2\text{-CH}_3 \rightarrow M\text{-Naph-CH}_2\text{-Phen(H)-CH}_2\text{-CH}_3$
$M-H + M\text{-Naph-CH}_2\text{-Phen-CH}_3 \rightarrow M\text{-Naph-CH}_2\text{-Phen(H)-CH}_3$
$M-H + M-NBBM \rightarrow M\text{-Naph-CH}_2\text{-Phen-CH}_2\text{-CH}_2\text{-(H)Phen}$

Table 5.3 continued

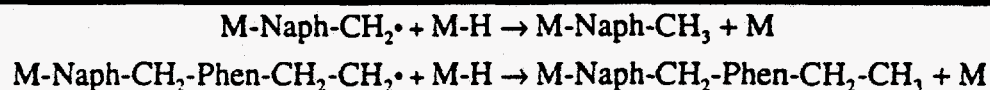
---

**Radical Elimination Reactions**

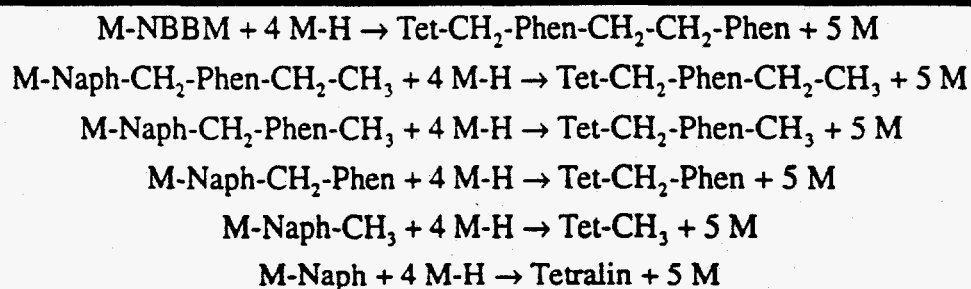

---


**Surface Recombination Reactions**


---


**Naphthyl Hydrogenation Reactions**


---



### 5.2.1 Estimation of Rate Constants

The reaction family concept (Semenov, 1958; and McMillen and Malhotra, 1990) was exploited to estimate the rate constant for each reaction step. Associated linear free energy relationships for homogeneous (LaMarca, 1992) and heterogeneous catalytic reactions (Mochida and Yoneda, 1967; Yoneda, 1967; Matsumoto et al., 1968; Dunn, 1968; Dumesic et al., 1987; and Landau et al., 1992) have been shown to correlate kinetics well. For catalytic cycles, a reasonable estimate of the rate determining step (RDS) allows an LFER to relate the overall reaction rate to a reactivity index of the RDS. This motivated the current scheme where the rate constant ( $k$ ) for each reaction was constrained by the reaction enthalpy ( $\Delta H_{\text{reaction}}$ ) according to the relationship of Equation 5.1. Each reaction family was characterized by two parameters,  $A$  and  $\alpha$ . In the present application, the value of  $\alpha$  was fixed at the thermal value of 0.5 for the catalytic radical elimination reaction family.

$$\log_{10} k = A - \frac{\alpha \Delta H_{\text{reaction}}}{2.303RT} \quad (5.1)$$

Table 5.4 summarizes the kinetically independent reaction families and the associated LFER for each. The list reveals subdivisions of certain reactions. For example, the experimental observation that naphthalene hydrogenated at a higher rate than substituted naphthalenes suggested possible steric differences between the two. Different  $A$  factors were thus allowed for their adsorption reactions.

**Table 5.4** Summary of reaction families used to predict rate constants.

Reaction Family	$\log_{10}k$
Hydrogen Adsorption	2.60
Naphthalene Adsorption	$3.54 + \frac{0.28\Delta H_{\text{reaction}}}{2.303RT}$
Substituted Naphthalene	$3.0 + \frac{0.28\Delta H_{\text{reaction}}}{2.303RT}$
H Atom Ipso Insertion Reactions to Naphthyl Moieties	-1.24
H Atom Ipso Insertion Reactions to "B" Phenyl Moieties	-1.86
Radical Elimination Reactions	$15.0 + \frac{0.5\Delta H_{\text{reaction}}}{2.303RT}$
Surface Recombination Reactions	9.0
Naphthyl Hydrogenation Reactions	2.01
Hydrogen Desorption	0.3
Naphthyl Desorption	3.25

Prediction of the rate constants thus amounted to obtaining reaction and adsorption enthalpies. This was calculated in the standard manner as the difference between the enthalpy of formation ( $\Delta H^\circ_f$ ) of the products and the reactants. Since many model components were without experimental values, estimation techniques were examined. For this purpose, computational quantum chemistry served as the tool for estimating species properties (e.g.,  $\Delta H^\circ_f$ ) from structure.

Computational quantum chemistry has been demonstrated by Neurock (1992) to be a reliable method for estimating QSRR/LFER reaction indices. Specifically, for hydrocarbon species, semiempirical methods such as the MOPAC program (Stewart, 1989), which utilizes an MNDO method for solving the

Schrödinger equation (Dewar et al., 1977a, 1977b, 1978a, 1978b), are both useful and relatively easy to use. However, the catalytic reaction families examined herein involve interactions with transition metals which cannot be handled by the current MNDO parameter sets. Consequently, a different method for estimating energetics of transition metal-containing compounds was sought.

#### **5.2.1.1 A Computational Quantum Chemical Method for Estimating Energetics of Transition Metal Species**

The main challenges facing the estimation of an index for species involving metal surfaces was the large number of metal atoms contained in a metal particle. This renders a complex quantum mechanical calculation of the entire system impossible. These two challenges were overcome through the use of the Atomic Superposition Electron Delocalization Molecular Orbital (ASED-MO) method. This provided a computationally tractable examination of the interaction between hydrocarbons and small metal clusters.

ASED-MO is a quantum mechanical method proposed by Anderson (1972, 1990) for calculating molecular energetics. It is a semiempirical method based on the Extended Hückel method (Hoffmann, 1963) for solution of the Schrödinger equation. In ASED-MO, a molecule is considered as a superposition of rigid atoms, and the energy of the system is taken as the sum of pair-wise repulsion energies. The energy is then calculated for each electron using a one electron Hamiltonian for the case of a point charge in the potential field generated by the other electrons and nuclei in the system. Then, assuming that the molecular orbital wave functions are linear combinations of the atomic orbitals (Extended Hückel), the molecular orbital coefficients are solved from the secular equation (Anderson, 1975a). This allows determination of the energy of the molecule.

The parameters required for use of the ASED-MO method are the experimentally determined valence state ionization energies (VSIE) of the atoms considered and the theoretically derived Slater-type orbital parameters, which allow explicit calculation of the wave functions and are found in the literature. Table 5.5 lists the parameters used for this analysis (Ades et al., 1994).

**Table 5.5** Atomic orbital parameters used for ASED-MO calculations.

Atom	Orbital	VSIE (eV)	$\xi_1$ (au <sup>-1</sup> )	$\xi_2$ (au <sup>-1</sup> )	$C_1$	$C_2$
H	1s	-13.6	1.3			
C	2s	-21.4	1.625			
	2p	-11.4	1.625			
O	2s	-28.48	2.2459			
	2p	-13.62	2.2266			
S	3s	-20.0	1.817			
	3p	-13.3	1.817			
	3d	-8.0	1.50			
Mn	4s	-7.434	1.6208			
	4p	-3.01	1.3208			
	3d	-9.0	5.15	1.7	0.514	0.693
Fe	4s	-9.1	1.9			
	4p	-5.32	1.9			
	3d	-12.6	5.35	2.0	0.5505	0.6260
Mo	5s	-7.1	1.956			
	5p	-3.92	1.921			
	4d	-8.56	4.542			

The ASED-MO method has been found to predict molecular geometries and energies for small diatomic and triatomic molecules (Anderson, 1972, 1975b, 1976) accurately. Moreover, it has also been found to correctly predict experimentally observed trends in larger molecules and metal clusters (Saillard and Hoffmann, 1984; Anderson et al., 1988a, 1989a; and Koerts and van Santen, 1991). As a result, the ASED-MO method has shown an ability to provide insight into bonding and hydrocarbon activation which occurs on metal surfaces (Anderson, 1981; Anderson et al., 1988b, 1989b; and Ades et al., 1991, 1994). Thus, it seemed reasonable to expect the ASED-MO method to predict accurate trends for the relatively demanding calculations for the large metal clusters used here.

#### 5.2.1.2 Analysis of Metal Clusters

The reaction systems including  $\text{Fe}(\text{CO})_5$ ,  $\text{Mo}(\text{CO})_6$ ,  $\text{Mn}_2(\text{CO})_{10}$ ,  $\text{Fe}_2\text{O}_3$  and  $\text{MoS}_2$  catalytic precursors were considered. The carbonyl compounds,  $\text{Fe}(\text{CO})_5$ ,  $\text{Mo}(\text{CO})_6$ , and  $\text{Mn}_2(\text{CO})_{10}$  are unstable at the reaction conditions (400 °C and 1000 psig of  $\text{H}_2$ , cold) and decompose to metal particles. These cases were thus modeled as simple metal clusters of Fe, Mo and Mn.  $\text{Fe}_2\text{O}_3$  and  $\text{MoS}_2$  are more stable, so their active species were assumed to be identical to the initial structure.

The model catalytic crystal structures were obtained from the literature (Ewald and Hermann, 1931; Wyckoff, 1931, 1935; Bragg et al., 1965; and Glazer, 1987). The elemental clusters of Fe and Mo are body centered cubic (bcc) structures, whereas Mn is a distorted face centered cubic (fcc) structure and  $\text{Fe}_2\text{O}_3$  and  $\text{MoS}_2$  are hexagonal structures (hex). The unit cell parameters for the structures are listed in Table 5.6 and were used to construct clusters of between 40-50 atoms for use in the ASED-MO calculations. The bcc structures contain 41 atoms and are constructed of



four unit cells in the x and y directions and one half unit cell in the negative z direction, as shown in Figure 5.2. The fcc structure contains 49 atoms and is constructed three unit cells in the x and y directions and one half unit cell in the negative z direction as shown in Figure 5.3. The iron oxide and molybdenum disulfide clusters contain 45 and 50 atoms, respectively, (18 iron, 27 oxygen, 25 molybdenum and 25 sulfur) with the top layer of each cluster being comprised of metal atoms. This is illustrated in Figures 5.4 and 5.5.

**Table 5.6** Structural parameters for the metal clusters modeled with the ASED-MO method.

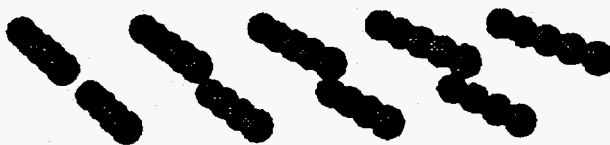
Cluster	Geometry	a (Angstroms)	b (Angstroms)	c (Angstroms)
Fe	bcc	3.464		
Mo	bcc	3.147		
Mn	distorted fcc	3.774	3.774	3.533

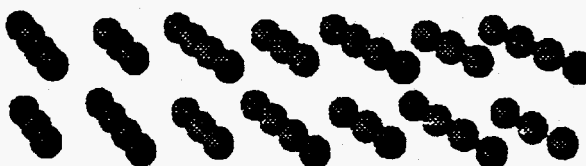
Cluster	Geometry	$a_0$ (Angstroms)	$\alpha$
Fe <sub>2</sub> O <sub>3</sub>	hex	5.4135	55.283°

Cluster	Geometry	$a_0$ (Angstroms)	$c_0$ (Angstroms)
MoS <sub>2</sub>	hex	3.15	12.30



**Figure 5.2** Cluster geometry used for the bcc metal structures of Fe and Mo.



**Figure 5.3** Cluster geometry used for the distorted fcc structure of Mn.



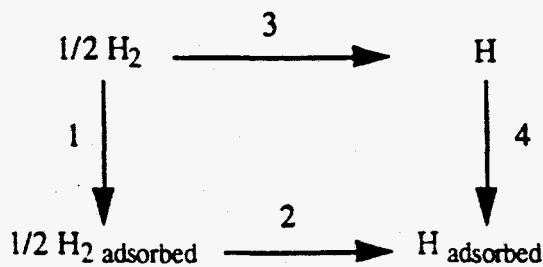
**Figure 5.4** Cluster geometry used for the hexagonal structure of  $\text{Fe}_2\text{O}_3$ . The darker shaded atoms are Fe and the lighter shaded atoms are O.



**Figure 5.5** Cluster geometry used for the hexagonal structure of  $\text{MoS}_2$ . The darker shaded atoms are Mo and the lighter shaded atoms are S.

Molecular orbital calculations were carried out to estimate the reaction indices shown in Table 5.7 for the metal-hydrocarbon reactions. All calculations considered interactions on the (001) surface of the metal clusters only. The adsorption enthalpy of naphthalene, which may be directly calculated with ASED-MO, was employed as the index for adsorption of naphthalene-containing molecule on the metal surface. Similarly, since hydrogen ipso substitution at the naphthalene moiety plays a prominent role in the mechanistic kinetic model, the direct calculation of the adsorption energy for an H-substituted naphthalene molecule was also carried out. However, since the mechanism for dissociative adsorption of  $\text{H}_2$  on a metal surface is unclear, the enthalpy of adsorption of a single hydrogen atom is employed as the reaction index for  $\text{H}_2$  adsorption. The basis for this index choice is illustrated in Figure 5.6. The actual dissociative adsorption likely proceeds through some combination of reactions 1 and 2 either in series or simultaneously. However, since enthalpy is a state function, consideration of the reaction path following reactions 3 and 4 will yield the same enthalpy of adsorption. It is noteworthy that the gas phase dissociation of  $\text{H}_2$  (reaction 3 in Figure 5.7) is independent of the metal surface. Thus, estimation of the enthalpy of adsorption of a hydrogen atom is sufficient to

characterize the changes in enthalpy for dissociative adsorption of  $H_2$  on different metal surfaces. The errors associated with the energy estimates calculated with the ASED-MO method as well as the constant enthalpy of dissociation for reaction 3 will be absorbed by the adjustable parameters of the linear free energy relationship.



**Figure 5.6** Alternate reaction paths leading to dissociative adsorption of  $H_2$  on a metal surface.

The ASED-MO calculations modeling hydrogen adsorption and desorption involved fixing the coordinates of the metal atoms and varying the position of a lone hydrogen atom in the proximity of the cluster's (001) surface. The ASED-MO energy was then minimized using a global optimization routine (Stark, 1993) that sought the optimal geometry for the hydrogen-cluster interaction. This optimal energy was subtracted from that for infinite separation between the hydrogen atom and the cluster to estimate the enthalpy of adsorption for a hydrogen atom.

Table 5.7 Summary of reaction families used to predict rate constants.

Reaction Family	Reaction Index
Hydrogen Adsorption	$\Delta H_{\text{ads}}$ for H atom adsorption
Naphthalene Adsorption	$\Delta H_{\text{ads}}$ for naphthalene adsorption
H Atom Ipso Insertion Reactions	$(\Delta H_{\text{ads}}$ for a H substituted naphthyl radical)- $(\Delta H_{\text{ads}}$ for H atom + $\Delta H_{\text{ads}}$ for naphthalene) + $(\Delta H_{\text{reaction}}$ for hydrocarbon insertion only)
Radical Elimination Reactions	$\Delta H_{\text{reaction}}$ for hydrocarbon elimination only
Surface Recombination Reactions	0.0
Naphthyl Hydrogenation Reactions	$(\Delta H_{\text{ads}}$ for a H substituted naphthyl radical)- $(\Delta H_{\text{ads}}$ for H atom + $\Delta H_{\text{ads}}$ for naphthalene) + $(\Delta H_{\text{reaction}}$ for hydrocarbon insertion only)
Hydrogen Desorption	$-\Delta H_{\text{ads}}$ for H atom adsorption
Naphthyl Desorption	$-\Delta H_{\text{ads}}$ for Naphthalene adsorption

A similar method was used for calculations modeling naphthyl adsorption at a cluster's (001) surface. The positions of the cluster atoms were fixed, as was the structure of the naphthalene molecule. The naphthalene molecule was then placed flat, parallel to the cluster surface, and its position relative to the surface varied to find the minimum energy location. A calculation was also performed at infinite naphthalene-cluster separation and the difference in energies was taken as the heat of adsorption for naphthalene. The identical procedure was employed to estimate the heat of adsorption for a naphthalene molecule substituted with a hydrogen atom at the 1 position to probe the effect of hydrogen insertion into the aromatic rings.

Table 5.8 lists the adsorption enthalpies estimated with the ASED-MO method for the Fe, Mo, Mn, Fe<sub>2</sub>O<sub>3</sub>, and MoS<sub>2</sub> clusters. The Mn cluster binds

naphthalene most strongly. The Mo-containing clusters bind the naphthalene molecules more tightly than do the Fe containing clusters. The differences in energies for hydrogen adsorption are less dramatic. The Fe-containing clusters bond H atoms most strongly, whereas the Mo-containing clusters bond H atoms least strongly.

**Table 5.8** Adsorption energies for hydrogen and naphthalene on the (001) surface of catalytic metal clusters.

Cluster	$\Delta H_{\text{ads}}$ H Atom	$\Delta H_{\text{ads}}$ Naphthalene	$\Delta H_{\text{ads}}$ H Substituted Naphthalene
Fe	-2.542 eV	-5.935 eV	-4.896 eV
Mo	-0.988 eV	-13.614 eV	-14.100 eV
Mn	-1.444 eV	-49.397 eV	-51.291 eV
Fe <sub>2</sub> O <sub>3</sub>	-3.491 eV	-2.969 eV	-3.012 eV
MoS <sub>2</sub>	-0.819 eV	-17.816 eV	-18.195 eV

### 5.2.1.3 LFERs for Catalytic Reaction Families

The foregoing estimates for the enthalpies of adsorption of hydrogen and naphthalene species allowed the specification of the indices for the LFERs describing the catalytic reactions of NBBM. The specific forms of the reaction indices associated with the catalytic reactions families were listed in Table 5.7. For example, the enthalpy of adsorption for a free H atom was demonstrated to be an accurate reaction index for dissociative adsorption of H<sub>2</sub> on the metal surface. The reaction index for the ipso insertion of a catalytically bound hydrogen atom into an aromatic ring, shown in Figure 5.7, is defined as its enthalpy of reaction. Equation 5.2 shows the standard definition for the reaction enthalpy in terms of the enthalpies of formation of the

reactants and product. In addition, the adsorption enthalpies for the reactants and product may also be represented in terms of the enthalpies of formation of the participating species as defined in Equations 5.3-5.5. Rearrangement of Equations 5.3-5.5 to obtain explicit relations for  $\Delta H^\circ_{\text{f H}}$ ,  $\Delta H^\circ_{\text{f Ar-R}}$  and  $\Delta H^\circ_{\text{f Ar(H)-R}}$ , respectively. Subsequent substitution into equation 5.2 yields the exact relationship of Equation 5.6

$$\Delta H^\circ_{\text{reaction}} = \Delta H^\circ_{\text{f M}} + \Delta H^\circ_{\text{f M-Ar(H)-R}} - \Delta H^\circ_{\text{f M-H}} - \Delta H^\circ_{\text{f M-Ar-R}} \quad (5.2)$$

$$\Delta H^\circ_{\text{ads H}} = \Delta H^\circ_{\text{f M-H}} - (\Delta H^\circ_{\text{f M}} + \Delta H^\circ_{\text{f H}}) \quad (5.3)$$

$$\Delta H^\circ_{\text{ads Ar-R}} = \Delta H^\circ_{\text{f M-Ar-R}} - (\Delta H^\circ_{\text{f M}} + \Delta H^\circ_{\text{f Ar-R}}) \quad (5.4)$$

$$\Delta H^\circ_{\text{ads Ar(H)-R}} = \Delta H^\circ_{\text{f M-Ar(H)-R}} - (\Delta H^\circ_{\text{f M}} + \Delta H^\circ_{\text{f Ar(H)-R}}) \quad (5.5)$$

$$\Delta H^\circ_{\text{reaction}} = \Delta H^\circ_{\text{ads Ar(H)-R}} - (\Delta H^\circ_{\text{ads H}} + \Delta H^\circ_{\text{ads Ar-R}}) + \Delta H^\circ_{\text{reaction Ar-R + H} \rightarrow \text{Ar(H)-R}} \quad (5.6)$$

describing the reaction enthalpy in terms of the associated adsorption enthalpies and the reaction's gas phase reaction enthalpy. The terms on the right-hand side of Equation 5.6 may be estimated directly with ASED-MO to determine the reaction index value. Additionally, the radical elimination and surface recombination reaction enthalpies were estimated to be those of the analogous hydrocarbon-only systems. For the catalytic hydrogenation family, which consists of addition of four catalytically bound hydrogen atoms into an aromatic ring, the reaction indices were estimated to be the reaction enthalpy for ipso addition of an H atom. This was tantamount to assuming that the insertion of the first H atom is the rate determining step for the overall rate of hydrogenation.



**Figure 5.7** Chemical equation for an ipso insertion of a catalytically bound hydrogen atom to an aromatic ring.

### 5.3 Parameter Estimation

Optimization of the model parameters,  $A$  and  $\alpha$  for each of the reaction families of Table 5.4 to maximize model agreement with experimental observations for the five catalysts  $\text{Fe}(\text{CO})_5$ ,  $\text{Mo}(\text{CO})_6$ ,  $\text{Mn}_2(\text{CO})_{10}$ ,  $\text{Fe}_2\text{O}_3$ , and  $\text{MoS}_2$  was achieved through the use of the MLSL algorithm, as coded by Stark (1993), on an IBM RS/6000 Model 530H workstation. Briefly, the MLSL program randomly chooses points within the parameter space at which the objective function is evaluated. Subsequently, a local minimization procedure is started at 10% of the randomly chosen points which have the lowest objective function value. The identified local minima are reported, and the local minimum with the smallest objective function value is taken as the global minimum.

The objective function used for the regression is a variation of the sum of square errors shown in Equation 5.7, where  $F$  is the value of the objective function, and  $y_{ij}^{\text{pred}}$  and  $y_{ij}^{\text{exp}}$  are the predicted and measured molar yields for product  $i$  at time  $j$ , respectively. The weighting factor ( $w_i$ ) enables the contribution of each species to the objective function to be manipulated. The values of the optimal parameters are listed in Table 5.9.

$$F = \sum_{j=1}^{\text{\#times}} \sum_{i=1}^{\text{\#comp}} w_i (y_{ij}^{\text{pred}} - y_{ij}^{\text{exp}})^2 \quad (5.7)$$

Model predictions of the main NBBM catalysis products were compared to the associated experimental NBBM catalysis data at 400 °C under 1000 psig  $\text{H}_2$  (cold). This is summarized in the form of the parity plot of Figure 5.8 which shows that the model predictions are in general agreement with the experimental results. The deviation between the model prediction and the experimental data increases as the product yield decreases. Most of the scatter is for products whose yields are less than

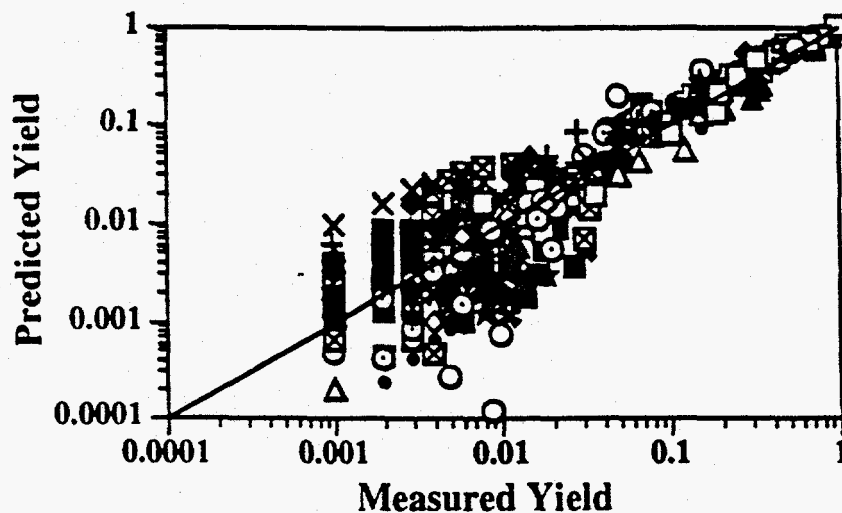


1%. This low yield deviation is put into perspective by the parity plot of Figure 5.9 which shows the product yields on a linear scale.

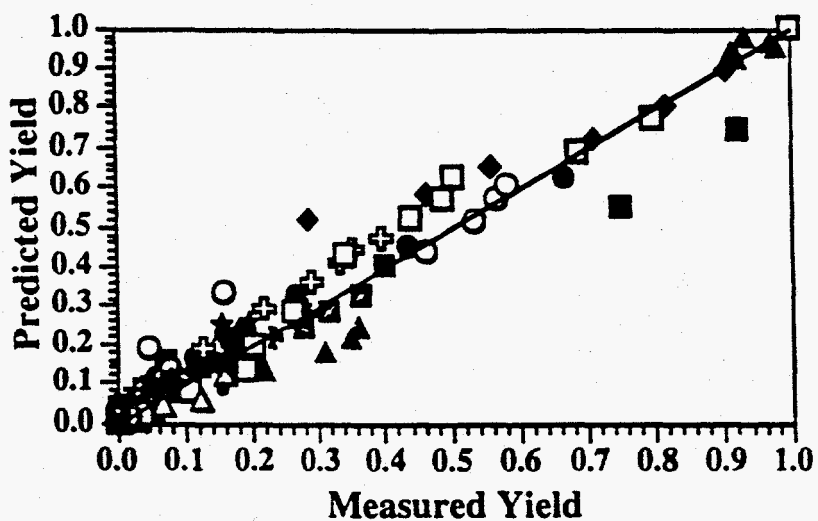
Figures 5.10-5.12 show that the mechanistic model captures the behavior of NBBM disappearance as well as the formation of the two main product lumps, bond A scission and NBBM hydrogenation. Thus, the mechanistic model is validated in its ability to describe the essence of NBBM catalysis at 400 °C with several transition metal-based catalysts.

**Table 5.9** Optimal parameters for the mechanistic model describing NBBM catalysis at 400 °C with  $\text{Fe}(\text{CO})_5$ ,  $\text{Mo}(\text{CO})_6$ ,  $\text{Mn}_2(\text{CO})_{10}$ ,  $\text{Fe}_2\text{O}_3$  and  $\text{MoS}_2$ .

Reaction Family	A	$\alpha$
Hydrogen Adsorption	2.60	0.0
Naphthalene Adsorption	3.54	0.28
Substituted Naphthalene	3.0	0.28
H Atom Ipso Insertion Reactions to Naphthyl Moieties	-1.24	0.0
H Atom Ipso Insertion Reactions to "B" Phenyl Moieties	-1.86	0.0
Radical Elimination Reactions	15.0	0.5
Surface Recombination Reactions	9.0	0.0
Naphthyl Hydrogenation Reactions	2.01	0.0
Hydrogen Desorption	0.3	0.0
Naphthyl Desorption	3.25	0.28



**Figure 5.8** Parity plot for the NBBM mechanistic model describing catalytic reaction of NBBM at 400 °C under hydrogen with  $\text{Fe}(\text{CO})_5$ ,  $\text{Mo}(\text{CO})_6$ ,  $\text{Mn}_2(\text{CO})_{10}$ ,  $\text{Fe}_2\text{O}_3$  and  $\text{MoS}_2$  on a logarithmic scale.



**Figure 5.9** Parity plot for the NBBM mechanistic model describing catalytic reaction of NBBM at 400 °C under hydrogen with  $\text{Fe}(\text{CO})_5$ ,  $\text{Mo}(\text{CO})_6$ ,  $\text{Mn}_2(\text{CO})_{10}$ ,  $\text{Fe}_2\text{O}_3$  and  $\text{MoS}_2$  on a linear scale.

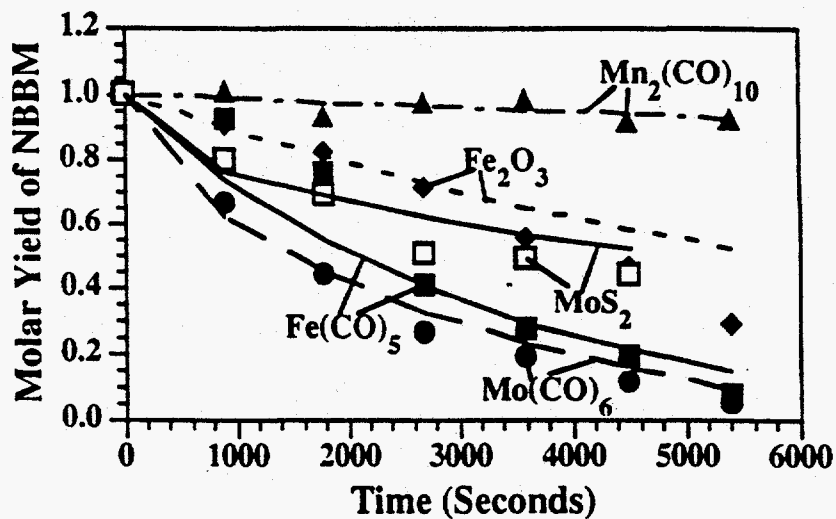


Figure 5.10 Model predictions and experimental data describing the catalytic disappearance of NBBM at 400 °C under hydrogen with  $Fe(CO)_5$ ,  $Mo(CO)_6$ ,  $Mn_2(CO)_{10}$ ,  $Fe_2O_3$  and  $MoS_2$ .

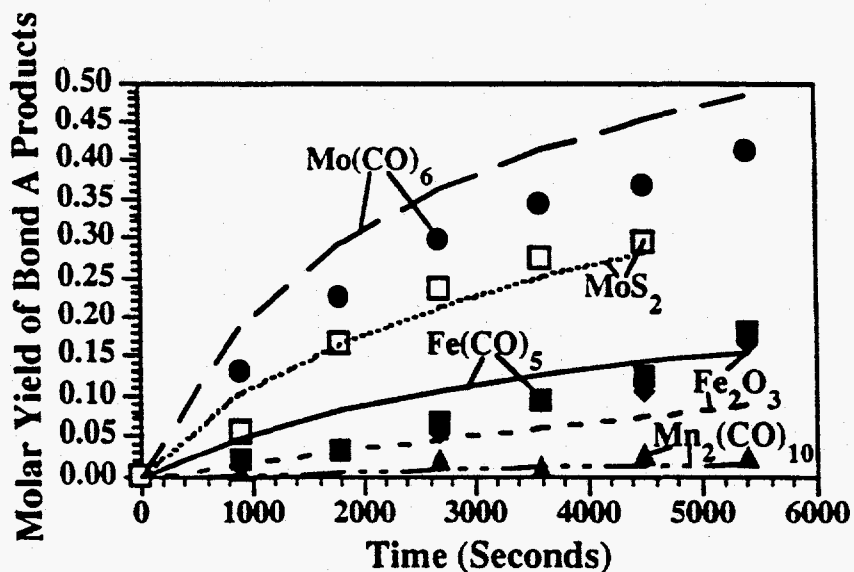


Figure 5.11 Model predictions and experimental data for the bond A scission products methylbibenzyl and p-xylene from reaction of NBBM at 400 °C under hydrogen with  $Fe(CO)_5$ ,  $Mo(CO)_6$ ,  $Mn_2(CO)_{10}$ ,  $Fe_2O_3$  and  $MoS_2$ .

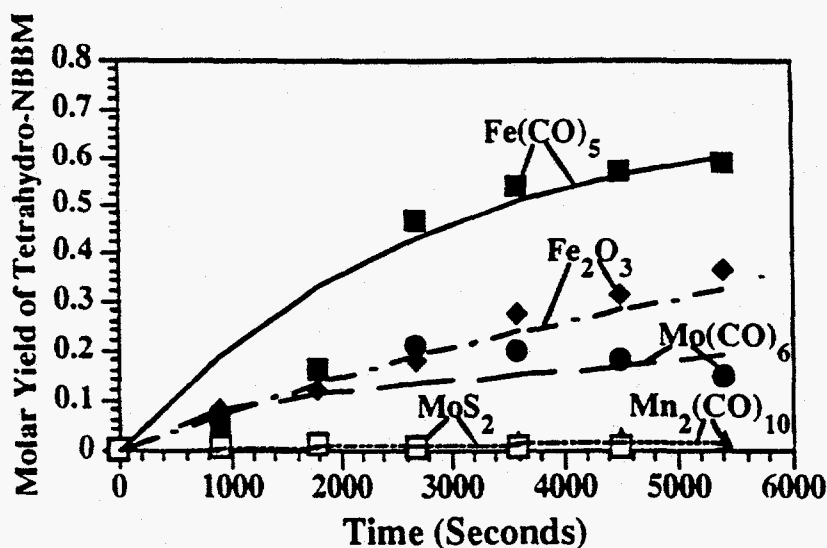


Figure 5.12 Model predictions and experimental data for NBBM hydrogenation products from reaction of NBBM at 400 °C under hydrogen with  $\text{Fe}(\text{CO})_5$ ,  $\text{Mo}(\text{CO})_6$ ,  $\text{Mn}_2(\text{CO})_{10}$ ,  $\text{Fe}_2\text{O}_3$  and  $\text{MoS}_2$ .

#### 5.4 Mechanistic Modeling Results

The now-validated model can be used to probe the important NBBM catalytic reaction pathways and underlying reaction mechanisms. To this end, the NBBM catalytic reaction model was examined in terms of the controlling mechanisms which lead to the formation of the major products.

The major product lumps, bond A scission, bond B scission and NBBM hydrogenation all require interaction of catalyst-activated hydrogen with adsorbed NBBM or other naphthalene-containing molecules. Thus, the surface concentrations of the adsorbed species is critical to understanding the behavior of the reacting system. Figures 5.13-5.15 show the time dependence of the surface concentrations of unoccupied catalytic sites, bound naphthalene-containing molecules (naphthalene, methylnaphthalene, naphthylphenylmethane, naphthyltolylmethane and NBBM) and

bound H atoms, respectively. It is noteworthy that the stoichiometry of the mechanistic reactions involving the metal sites effect an overall site balance, catalyst sites are neither created or consumed. Figure 5.13 shows that, for each of the clusters examined, the model predicts that nearly all (> 99.5%) of the available catalytic sites are occupied. Figure 5.14 shows that as the ASFD-MO enthalpy of adsorption for naphthalene decreases (increasing exothermicity), the relative coverage with naphthalene containing molecules increases. Figure 5.15 shows that the relative coverages of hydrogen inversely mirror the trends observed with NBBM. Since the parameter estimation results showed the energetics of hydrogen adsorption to have essentially no effect on the model results ( $\alpha = 0.0$  in Table 5.9), it appears that the energetics of naphthalene adsorption control the distribution of surface species. As the strength of the naphthalene-metal interaction increases, more hydrogen atoms are displaced from the metal, thus influencing the distribution of potential reactants.

These surface concentrations affect the chemistry directly. The main catalytic chemistries, ipso H atom addition to aromatic rings and naphthyl hydrogenation, require the presence of both adsorbed hydrogen and adsorbed naphthalenes. As a result, too much of one species comes at the expense of the other and thus the rate. This was the case for Mn, which displayed a very strong naphthalene adsorption binding energy. The naphthalene containing molecules completely displaced hydrogen from the metal surface and no catalytic reactions were possible. This result agrees with the observed lack of activity for NBBM reaction with  $\text{Mn}_2(\text{CO})_{10}$ . Similarly, reaction in the presence of a metal surface which showed little or no ability for naphthalene adsorption would produce a hydrogen covered catalytic surface and would show no activity for NBBM consumption.

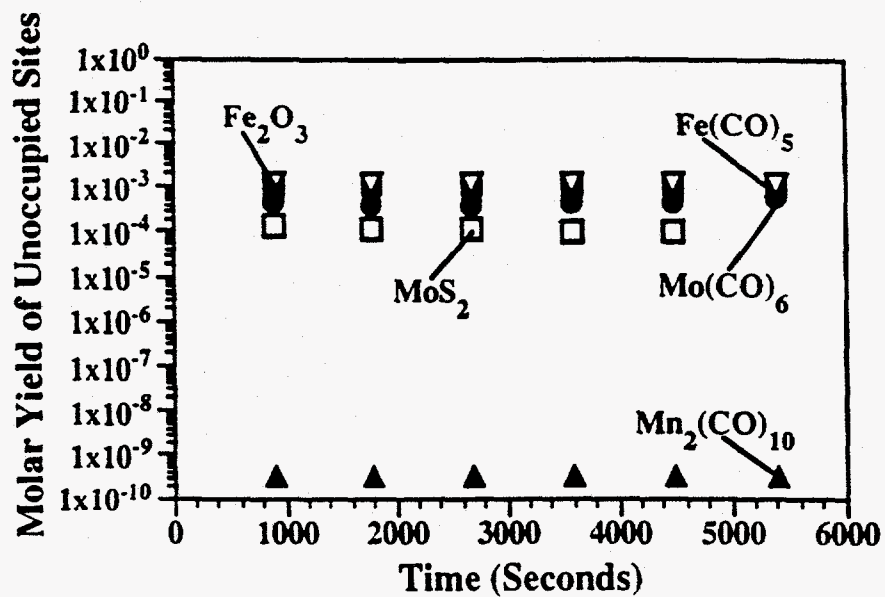


Figure 5.13 Plot of molar yield of unoccupied catalyst sites as a function of reaction time for Fe, Mo,  $\text{Fe}_2\text{O}_3$  and  $\text{MoS}_2$  clusters.

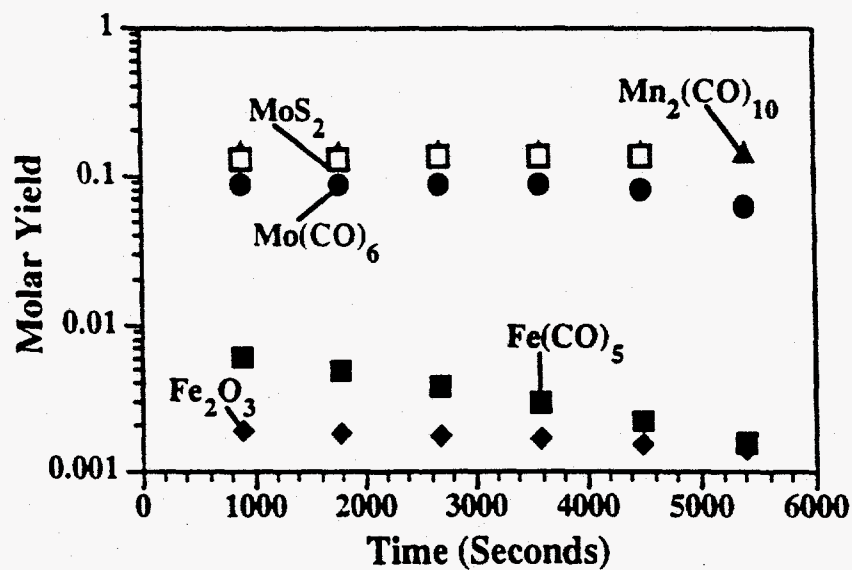


Figure 5.14 Plot of molar yield of catalytically bound, naphthalene containing molecules as a function of reaction time for Fe, Mo, Mn,  $\text{Fe}_2\text{O}_3$  and  $\text{MoS}_2$  clusters.

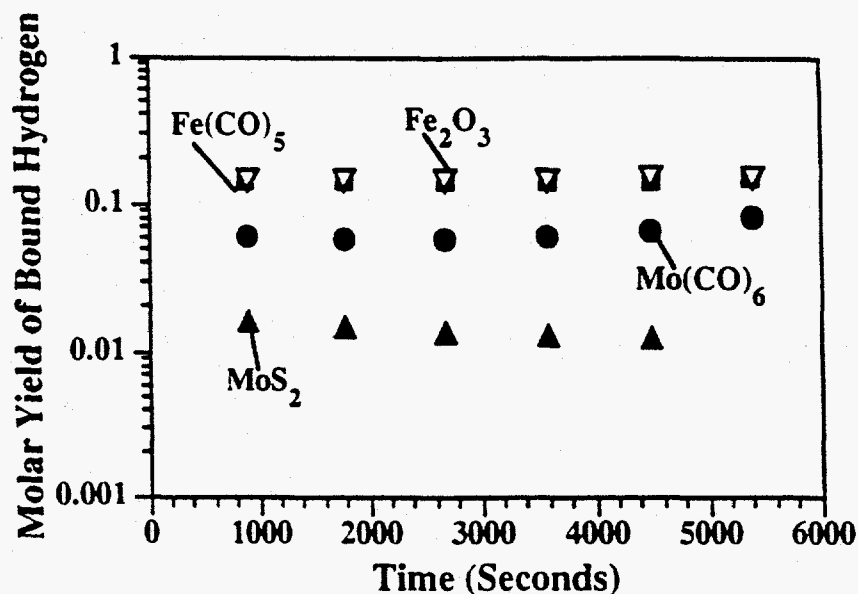
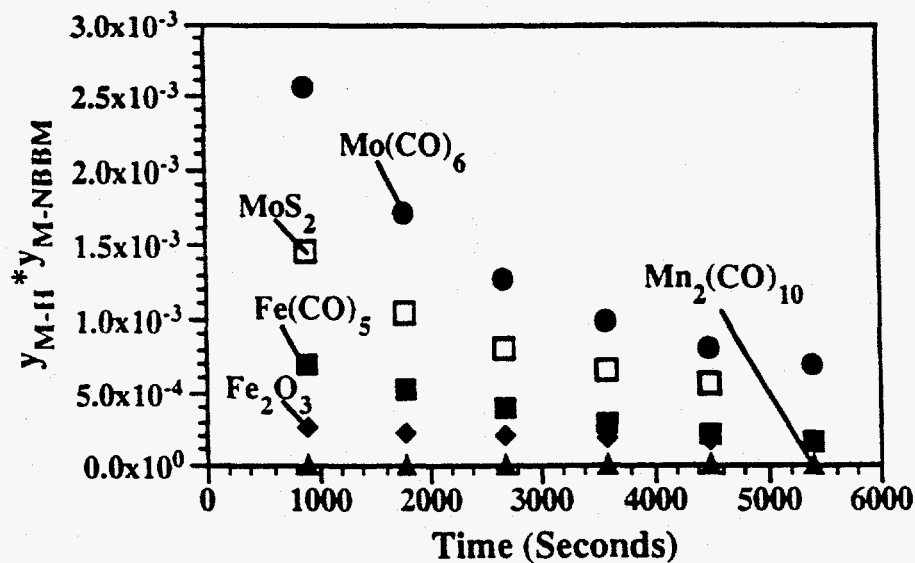


Figure 5.15 Plot of molar yield of catalytically bound H atoms as a function of reaction time for Fe, Mo, Fe<sub>2</sub>O<sub>3</sub> and MoS<sub>2</sub> clusters.

The relative surface concentrations of the naphthalene-containing species and hydrogen can also be used to explain the relative activities observed for bond A scission and naphthyl hydrogenation. The ordering in rates for the bond A scission reaction should match the ordering of the product of the concentrations of the catalytically bound hydrogen and the catalytically bound NBBM. This product is proportional to the rate expression for the rate determining ipso addition reaction. Figure 5.16 reveals that the ordering of this product for the metal surfaces matches the ordering observed for the formation of Bond A products in Figure 5.11.

The rate of naphthyl hydrogenation could be more sensitive to the concentration of surface bound hydrogen because of the "higher order" role of hydrogen. To this end, the ordering in rates for the catalytic hydrogenation reaction was tested against the ordering of the product of the concentration of the catalytically

bound hydrogen raised to the fourth power and the concentration of the catalytically bound NBBM. Figure 5.17 shows the ordering of this product matches the trend of Figure 5.11 for the rate of formation of the NBBM hydrogenation product tetrahydro-NBBM.



**Figure 5.16** The product of the molar yields of catalytically bound hydrogen atoms and catalytically bound NBBM molecules as a function of reaction time.



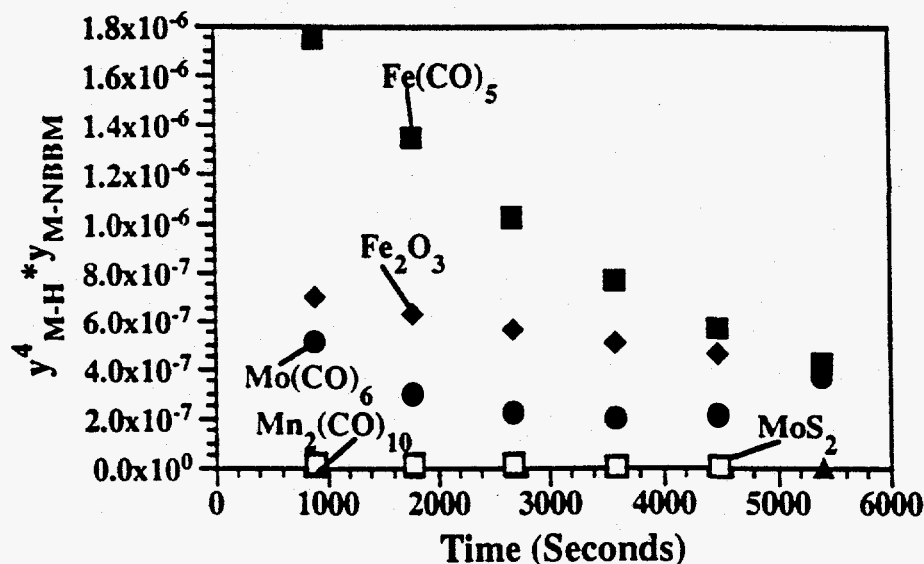


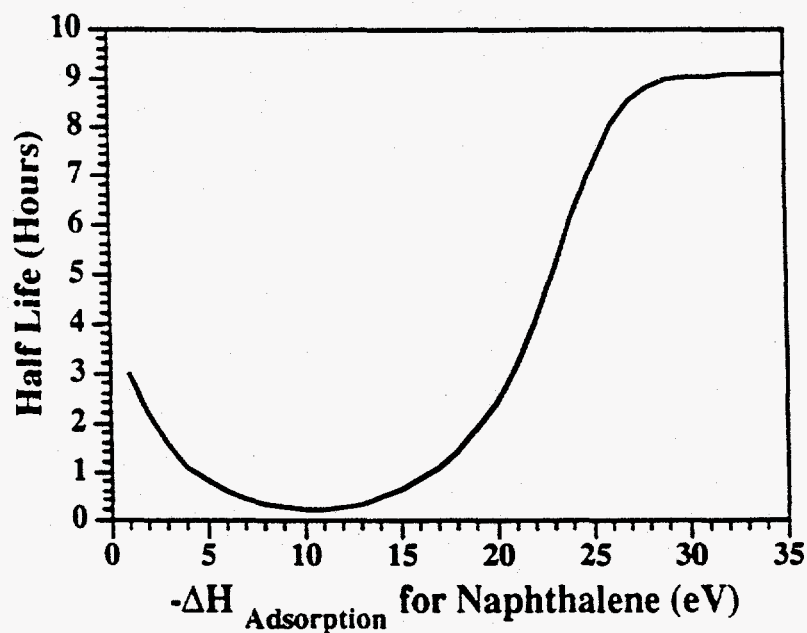
Figure 5.17 The product of the molar yields of catalytically bound hydrogen atoms to the fourth power and catalytically bound NBBM molecules as a function of reaction time.

### 5.5 Kinetics-Assisted Design of Catalysts

The dependence of the rate of NBBM consumption on the metal-naphthalene energetics established by the aforementioned mechanistic kinetics model constitutes a structure function relationship. Thus, prediction of NBBM disappearance rates and product selectivities is possible with the specification of the adsorption enthalpy only. Note that the use of the quantitative parameters derived here require use of the ASSED-MO enthalpy estimation method. As an example of the usefulness of this information, consider the limits of either very strong naphthalene adsorption or very weak naphthalene adsorption, where the rate of NBBM disappearance vanishes. It is intuitive that the highest rates of consumption will be at intermediate naphthalene-metal interactions. The associated enthalpy of adsorption at this maximum represents a property of an optimal catalytic material for NBBM consumption. Thus, the

specification of the maximum point gives the catalyst designer a starting point with which to design an optimally effective catalytic material.

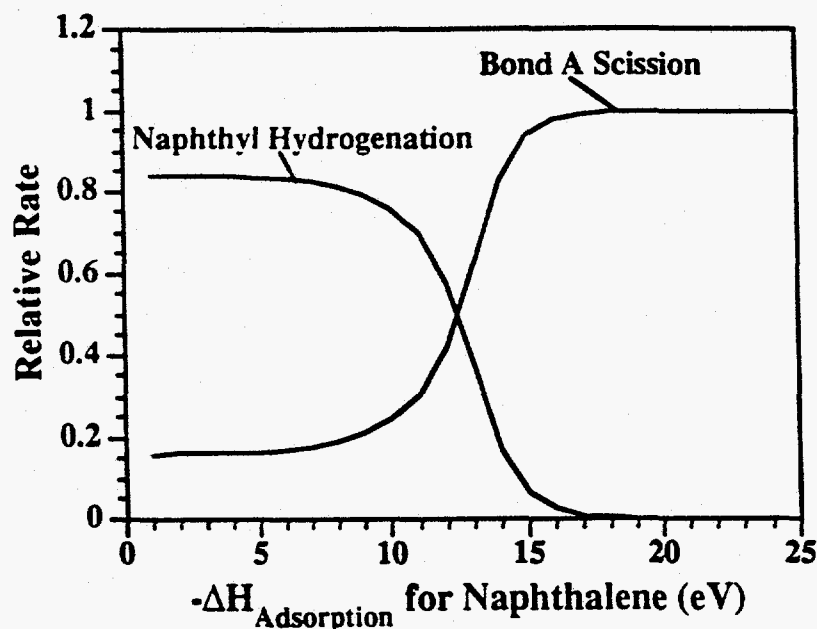
Figure 5.18 summarizes calculations aimed at probing this optimal material. Clearly, the half life for NBBM reaction predicted by the mechanistic model as a function of the ASED-MO estimated adsorption enthalpy passes through a minimum, which is the location of the highest rate and thus optimal material. The minimum of this curve occurs at approximately 10.5 eV.



**Figure 5.18** Plot of the half life for NBBM disappearance as a function of the ASED-MO estimated metal-naphthalene adsorption enthalpy.

It may be reasonable to assess the relative contributions of the hydrogenation and bond scission activities. The previous analysis did not distinguish between the activities leading to NBBM disappearance, and this left open the question of selectivity. Figure 5.19 shows the predicted relative rates of bond A scission and

hydrogenation as a function of the ASED-MO naphthalene adsorption enthalpy. For example, if it were known that coal liquefaction required equal rates of bond scission and hydrogenation for optimal conversion, then the optimal value of the naphthalene-metal interaction would be 12.5 eV. Any mechanistic insight which is gained for the complex reaction system may be used in this manner with a mechanistic modeling approach.



**Figure 5.19** Structure-function relationship for the relative contribution of the hydrogenation and bond scission reaction families to the reaction of NBBM at 400 °C in a hydrogen atmosphere.

The specification of the catalytic material possessing the optimal attributes of either Figure 5.18 or Figure 5.19 may be carried out through computer-aided screening. For example, a candidate catalytic material may be proposed and its adsorption enthalpy estimated with the ASED-MO method. Table 5.10 lists several

commonly used catalytic metals, including the materials used to parameterize the mechanistic model, their ASED-MO predicted adsorption enthalpies, and their predicted NBBM half lives. Mo and Pd predict the highest activity for NBBM consumption and, thus, will be the most effective catalysts for NBBM consumption of the examined materials. Due to the structural and reactivity similarities between NBBM and coal, Mo and Pd provide good starting points for the search for an optimally effective catalyst for coal liquefaction. The kinetics-assisted catalyst design method seems to be a reasonable assist in reducing both the cost and the effort in synthesizing and testing new candidate materials.

Table 5.10 ASED-MO predicted naphthalene adsorption enthalpies for several materials commonly used as catalysts.

Metal Cluster	$-\Delta H_{ads}$ H atom (eV)	$-\Delta H_{ads}$ Naphthalene (eV)	NBBM Half Life (ks)
Fe (bcc)	-2.54	-5.93	2.08
Mo (bcc)	-0.988	-13.61	1.50
Mn (dist. fcc)	-1.44	-49.40	32.72
Ni (fcc)	-0.331	-18.42	5.81
Pd (fcc)	-0.228	-6.82	1.58
Pt (fcc)	-0.216	-4.47	3.46
Rh (fcc)	-1.48	-2.52	6.72
Fe <sub>2</sub> O <sub>3</sub> (hex)	-3.49	-2.97	5.73
MoS <sub>2</sub> (hex)	-0.819	-17.82	4.94

### 5.6 Summary and Conclusions

The mechanism of the catalytic reaction of the coal model compound NBBM was modeled following an approach that employs the concept of reaction families and QSRR/LFERs for rate constant evaluation. Six NBBM catalytic reaction

families, namely hydrogen adsorption/desorption, naphthyl adsorption/desorption, ipso H atom insertion, radical elimination, naphthyl hydrogenation and surface recombination, were summarized in the form of reaction matrices which, when applied to the NBBM catalytic system, generated a mechanistic kinetics model for NBBM catalysis under hydrogen.

LFER parameters were determined through optimization of the model predictions with observed experimental yields for NBBM catalysis at 400 °C under hydrogen in the presence of each of the five catalytic materials  $\text{Fe}(\text{CO})_5$ ,  $\text{Mo}(\text{CO})_6$ ,  $\text{Mn}_2(\text{CO})_{10}$ ,  $\text{Fe}_2\text{O}_3$ , and  $\text{MoS}_2$ . Because of the fundamental nature of this model, the quantitative LFER parameters obtained from this kinetics analysis can be used to estimate rate constants in a model of several heavy hydrocarbon complex systems with the one constraint being that the metal-hydrocarbon energetics must be estimated with the ASED-MO method. The model was validated by its ability to describe the formation of the major products observed experimentally.

The model was also used to probe the controlling mechanisms of NBBM catalysis. It was found that the naphthalene-metal adsorption interaction controlled the rates and selectivities for NBBM reaction. At the limit of extremely strong naphthalene-metal adsorption, hydrogen is completely displaced from the catalytic surface preventing NBBM consumption. Similarly, at the limit of extremely weak naphthalene-metal adsorption, naphthalene containing compounds (NBBM) are displaced from the catalytic surface by hydrogen also preventing catalytic consumption of NBBM. Intermediate naphthalene-metal adsorption energies provide both bond scission and naphthyl hydrogenation activities. Due to the higher sensitivity of the hydrogenation rate to surface hydrogen concentration, bond scission dominates at stronger naphthalene-metal binding energies and hydrogenation

dominates at weaker naphthalene-metal binding energies. Additionally, kinetics-assisted design was carried out using the mechanistic model to specify the naphthalene-metal interaction yielding the optimal catalytic result. Several materials were placed on the half life versus adsorption enthalpy curve and Mo and Pd were predicted to be the most active catalytic materials.

## REFERENCES

- Ades. H.F., Companion, A.L., Subbaswamy, K.R. (1991) "A Comparative Study of Semiempirical Bond Dissociation Energy Calculations." *J. Phys. Chem.*, **95**, 6502.
- Ades. H.F., Companion, A.L., Subbaswamy, K.R. (1994) "Molecular Orbital Calculations for Iron Catalysts," *Energy & Fuels*, **8**, 71.
- Anderson, A.B. (1972) "Theoretical Approach to Potential Energy Functions for Linear  $AB_2$  and ABC and Bent  $AB_2$  Triatomic Molecules," *J. Chem. Phys.*, **57**, 4143.
- Anderson, A.B. (1975a) "Derivation of the Extended Hückel Method with Corrections: One Electron Molecular Orbital Theory for Energy Level and Structure Determinations." *J. Chem. Phys.*, **62**, 1187.
- Anderson, A.B. (1975b) "Vibrational Potentials and Structures in Molecular and Solid Carbon, Silicon, Germanium, and Tin," *J. Chem. Phys.*, **63**, 4430.
- Anderson, A.B., (1976) "Ethylene and Acetylene on Ni (111) Surfaces," *J. Chem. Phys.*, **65**, 1729.
- Anderson, A.B. (1981) "Atom Superposition and Electron Delocalization (ASED) Theory for Catalysis. Dissociative Properties of Acetylene on Fe and Ni (100) with Coadsorbed O, S, Se, and Implications of Te," *J. Catal.*, **67**, 129.
- Anderson, A.B., Maloney, J.J. (1988a) "Activation of Methane on Iron, Nickel, and Platinum Surfaces. A Molecular Orbital Study," *J. Chem. Phys.*, **92**, 809.
- Anderson, A.B., Maloney, J.J., Yu, J. (1988b) "Methane Activation over  $MoS_2$  and  $CH_4$  Stabilities: Molecular Orbital Theory," *J. Catal.*, **112**, 392.
- Anderson, A.B., Choe, S.J. (1989a) "Ethylene Hydrogenation Mechanism on the Pt (111) Surface. Theoretical Determination," *J. Chem. Phys.*, **93**, 6145.
- Anderson, A.B., Yu, J. (1989b) "Methane Conversion and Fischer-Tropsch Catalysis over  $MoS_2$ : Predictions and Interpretations from Molecular Orbital Theory," *J. Catal.*, **119**, 135.
- Anderson, A.B. (1990) "Structure and Electronic Factors in Heterogeneous Catalysis:  $C\equiv C$ ,  $C\equiv O$ , and C-H Activation Processes on Metals and Oxides." (in *Theoretical Aspects of Heterogeneous Catalysis*, J.B. Moffat, ed., Van Nostrand Reinhold, New York.)
- Bragg, L., Claringbull, G.F. (1965) *Crystal Structures of Minerals*. (Ed. Sir Lawrence Bragg, Cornell University Press, Ithaca, New York.)

- Dewar, M.J.S., Thiel, W. (1977a) "Ground States of Molecules. 38. The MNDO Method Approximations and Parameters," *J. Am. Chem. Soc.*, **99**, 4899.
- Dewar, M.J.S., Thiel, W. (1977b) "Ground States of Molecules. 39. MNDO Method Results for Molecules Containing Hydrogen, Carbon, Nitrogen and Oxygen," *J. Am. Chem. Soc.*, **99**, 4907.
- Dewar, M.J.S., Ford, G.P., McKee, M.L., Rzepa, H.S., Thiel, W., Yamaguchi, Y. (1978a) "Semiempirical Calculations of Molecular Vibrational Frequencies: The MNDO Method." *J. Molec. Struct.*, **43**, 135.
- Dewar, M.J.S., Rzepa, H.S. (1978b) "Calculations of Electron Affinities Using the MNDO Semiempirical SCF-MO Method." *J. Am. Chem. Soc.*, **100**, 784.
- Dumesic, J., Milligan, B.A., Greppi, L.A., Balse, V.R., Sarnowski, K.T., Beall, C.E., Kataoka, T., Rudd, D.E., Trevino, A.A. (1987) "A Kinetic Modeling Approach to the Design of Catalysts: Formulation of a Catalyst Design Advisory Program," *Ind. Eng. Chem.*, **26**, 1399.
- Dunn, I.J. (1968) "Linear Free Energy Relations in Modeling Heterogeneous Catalytic Reactions." *J. Catal.*, **12**, 335.
- Ewald, V.P.P., Hermann, C. (1931) *Strukturbericht*. (Covering 1913-1928, Johnson Preprint Corporation, New York.)
- Glazer, A.M. (1987) *The Structures of Crystals*. (IOP Publishing Limited, Bristol, England.)
- Guin, J., Zhan, X., Singh, R. (1993) "Activity and Selectivity of Dispersed Iron Catalysts in Coal Liquefaction and Model Compound Reactions," *Prepr. Paper: Am. Chem. Soc., Div. Fuel Chem.*, **38**, 86.
- Hoffmann, R. (1963) "An Extended Hückel Theory. I. Hydrocarbons," *J. Chem. Phys.*, **39**, 1397.
- Koerts, T., van Santen, R.A. (1991) "The Reaction Path for Recombination of Surface  $\text{CH}_x$  Species." *J. Mol. Catal.*, **70**, 119.
- Landau, R.N., Korré, S.C., Neurock, M., Klein, M.T., Quann, R.J. (1992) "Hydrocracking of Heavy Oils: Development of Structure/Reactivity Correlations for Kinetics," *Prepr. Paper: Am. Chem. Soc., Div. Fuel Chem.*, **37**, 1871.
- LaMarca, C. (1992) *Kinetic Coupling in Multicomponent Pyrolysis Systems*. (Ph.D. Dissertation, University of Delaware.)
- Linehan, J.C., Darab, J.G., Matson, D.W. (1993) "Results of Catalyst Testing Using Iron-based Catalysts," *Prepr. Paper: Am. Chem. Soc., Div. Fuel Chem.*, **38**, 66.
- Matsumoto, H., Take, J., Yoneda, Y. (1968) "Linear Free Energy Relationships in Heterogeneous Catalysis VIII. Isomerization of Alkylbenzenes over Solid Acid Catalysts," *J. Catal.*, **11**, 211.



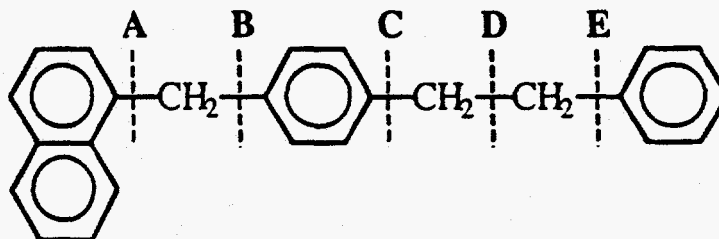
- McMillen, D.F., Malhotra, R. (1990) "A Mechanistic Numerical Model for Coal Liquefaction Involving Hydrogenolysis of Strong Bonds. Rationalization of Interactive Effects of Solvent Aromaticity and Hydrogen Pressure," *Energy & Fuels*, **4**, 184.
- Mochida, I., Yoneda, Y. (1967) "Linear Free Energy Relationships in Heterogeneous Catalysis. V. An Application of Quantum Chemical Reactivity Indexes to Heterogeneous Catalysis," *J. Catal.*, **9**, 57.
- Neurock, M. (1992) *A Computational Chemical Reaction Engineering Analysis of Complex Heavy Hydrocarbon Reaction Systems*. (Ph.D. Dissertation, University of Delaware.)
- Neurock, M., Klein, M.T. (1993) "When You Can't Measure - Model," *Chemtech*, September, 26.
- Saillard, J.-Y., Hoffmann, R. (1984) "C-H and H-H Activation in Transition Metal Complexes and on Surfaces," *J. Am. Chem. Soc.*, **106**, 2006.
- Semenov, N.N. (1958) *Some Problems in Chemical Kinetics and Reactivity* Volume II. (Princeton University Press, Princeton, NJ.)
- Stark, S.M. (1993) *An Investigation of the Applicability of Parallel Computation to Demanding Chemical Engineering Problems*. (Ph.D. Dissertation, University of Delaware.)
- Stewart, J.J.P. (1989) "Semiempirical Molecular Orbital Methods," in *Reviews in Computational Chemistry*. (K.B. Lipkowitz and D.B. Boyd, eds., VCH Publishers Inc.)
- Wyckoff, R.W.G. (1931) *The Structures of Crystals*. (Second Edition, The Chemical Catalog Company, Inc., New York.)
- Wyckoff, R.W.G. (1935) *The Structures of Crystals. Second Edition*. (Supplement for 1930-1934 to the Second Edition, Reinhold Publishing Corporation, New York.)
- Yoneda, Y. (1967) "Linear Free Energy Relationships in Heterogeneous Catalysis. IV. Regional Analysis for Solid Acid Catalysis," *J. Catal.*, **9**, 51.

## Chapter 6

### SUMMARY AND CONCLUSIONS

#### 6.1 Summary

A contribution to the understanding of and data base for the thermal and catalytic upgrading of complex mixtures such as coals and petroleum resids was attempted. The reaction family concept laid the foundation for a molecule-based modeling approach, which facilitated the construction of and rate parameter specification for mechanistic kinetic models. Specifically, the modeling approach was applied to thermal and catalytic reaction of the coal model compound 4-(1-naphthylmethyl)bibenzyl (NBBM), shown in Figure 6.1, in order to probe its salient reaction paths and mechanisms and to obtain quantitative linear free energy relationships which allow rate constant specification from molecular structure. The fundamental nature of the catalytic NBBM reaction model allowed application of the kinetics-assisted design formalism for specifying the properties of an optimal catalyst.



**Figure 6.1** The structure of the coal model compound 4-(1-naphthylmethyl)-bibenzyl (NBBM). The scissile bonds are labeled A through E.

### 6.1.1 Pyrolysis of NBBM

The thermal chemistry of NBBM at 420 °C under hydrogen and nitrogen atmospheres was examined. The observed product spectra was summarized by the bonds which were broken. The products observed from bond A scission were naphthalene, tetralin, naphthylphenylmethane, methylbibenzyl and p-xylene. Similarly, bond B scission yielded methylnaphthalene and bibenzyl, bond C scission yielded ethylbenzene and bond D scission yielded naphthyltolylmethane and toluene, and bond E scission yielded benzene. The results were consistent with a free radical reaction scheme based upon bond thermolysis and radical ipso-substitution steps. A sequence of bond fission, followed by hydrogen abstraction and radical ipso-substitution, in turn followed by  $\beta$ -scission, explains the formation of the major products well. However, reaction in a hydrogen atmosphere was consistent with ipso-substitution by benzyl and H• radicals effecting both bond A and bond B scission. Hydrogenation of naphthyl containing compounds was also observed. Reaction in a nitrogen atmosphere, however, yielded ipso-substitution reactions by benzyl radicals effecting bond A scission only.

Lower severity (400 °C) NBBM hydrolysis was qualitatively similar to the higher temperature reaction. "Bond A", "Bond B" and "Bond D" products were observed at a rate approximately half as fast as that observed for reaction at 420 °C. This data proved useful as a thermal background for catalytic reaction of NBBM.

### 6.1.2 Mechanistic Modeling of NBBM

Ten NBBM hydropyrolysis reaction families were summarized in the form of reaction matrices, each with a set of associated rules. A mechanistic model for NBBM hydropyrolysis was constructed through the exhaustive application of these ten matrices and rules to the components (original reactant and products) of the reacting system.

LFER parameters were optimized to allow the best fit between the model predictions and the experimental product yields for NBBM hydropyrolysis at 420 °C. The model was validated by the close agreement between experimental findings and model predictions. The mechanistic model was then used to probe the controlling mechanisms of NBBM pyrolysis. This identified a reaction cycle that effected the transformation of alkyl radicals into H• radicals through a series of hydrogen abstraction,  $\beta$ -scission and hydrogenation steps. In addition, the major reaction families contributing to NBBM consumption were found to be bond fission, radical ipso substitution by H• and benzyl radicals, with subsequent elimination and  $\beta$ -scission.

### 6.1.3 Catalytic Reaction of NBBM

The catalytic chemistry of NBBM in the presence of various transition metal-based catalysts and catalyst precursors was examined. Reaction in the presence of  $\text{Fe}(\text{CO})_3(\text{PPh}_3)_2$  under hydrogen and nitrogen at 420 °C demonstrated that the presence of hydrogen is necessary for catalytic activity.  $\text{Fe}(\text{CO})_4\text{PPh}_3$ ,  $\text{Fe}(\text{CO})_3(\text{PPh}_3)_2$ ,  $\text{Fe}(\text{CO})_2(\text{PPh}_3)_2\text{CS}_2$ ,  $\text{Fe}(\text{CO})_5$ ,  $\text{Mo}(\text{CO})_6$ ,  $\text{Fe}_2\text{O}_3$  and  $\text{MoS}_2$  all showed significant activity for the disappearance of NBBM above the thermal baseline at 400 °C;  $\text{Mn}_2(\text{CO})_{10}$  was inactive. All of the active catalytic material showed high selectivities toward bond A scission and NBBM hydrogenation. A simple reaction network employed to summarize the kinetics of the reaction systems indicated that, for  $\text{Fe}(\text{CO})_4\text{PPh}_3$ ,  $\text{Fe}(\text{CO})_3(\text{PPh}_3)_2$  and  $\text{Fe}(\text{CO})_2(\text{PPh}_3)_2\text{CS}_2$ : bond D scission was purely thermal and unaffected by the presence of the catalyst precursors; bond A rate constants were similar for reaction in the presence

of all three catalyst precursors and different from that for thermal reaction; and the hydrogenation rate constant was higher for  $\text{Fe}(\text{CO})_4\text{PPh}_3$  than for the other two catalyst precursors.

A consistent reaction mechanism involves catalytic dissociation of  $\text{H}_2$  into hydrogen atoms by the reduced metal, which are, in turn, inserted into the naphthalene system of NBBM; the naphthalene site at which the hydrogen atom is inserted determines the outcome of bond A scission or hydrogenation. The slower rate of bond A scission observed by the hydrogenated NBBM species can be qualitatively explained with decreased catalyst interaction and removal of ipso-substitution electronic topology. Similar activities were observed for  $\text{Fe}(\text{CO})_5$ ,  $\text{Mo}(\text{CO})_6$ ,  $\text{Fe}_2\text{O}_3$ , and  $\text{MoS}_2$ . The main reactivities of the active catalysts were bond A scission and naphthyl hydrogenation with an interesting feature that as the activity for bond A scission increased, its activity for naphthyl hydrogenation decreased. This suggests that: 1.) there is a site competition between naphthalene and H; and 2) high NBBM hydrogenation rates also destroy possible sites for hydrogen ipso substitution, resulting in lower bond scission rates.

#### 6.1.4 Mechanistic Modeling of NBBM Catalysis

NBBM catalytic reaction families were summarized in the form of reaction matrices which, when applied to the NBBM catalytic system, constructed a mechanistic model for NBBM catalysis under hydrogen. Essentially, the pyrolysis model was extended by addition of the catalytic steps to establish an overall NBBM reaction model.

LFER parameters were regressed to provide an optimal fit between the model predictions and the observed experimental yields for NBBM catalysis at 400 °C under hydrogen in the presence of each of the five catalytic materials  $\text{Fe}(\text{CO})_5$ ,  $\text{Mo}(\text{CO})_6$ ,  $\text{Mn}_2(\text{CO})_{10}$ ,  $\text{Fe}_2\text{O}_3$ , and  $\text{MoS}_2$ . The LFER parameters are general, but their use in application has the single restraint that the metal-hydrocarbon energetics must be estimated with the ASED-MO method. The model was validated by its ability to describe the formation of the major products observed experimentally.

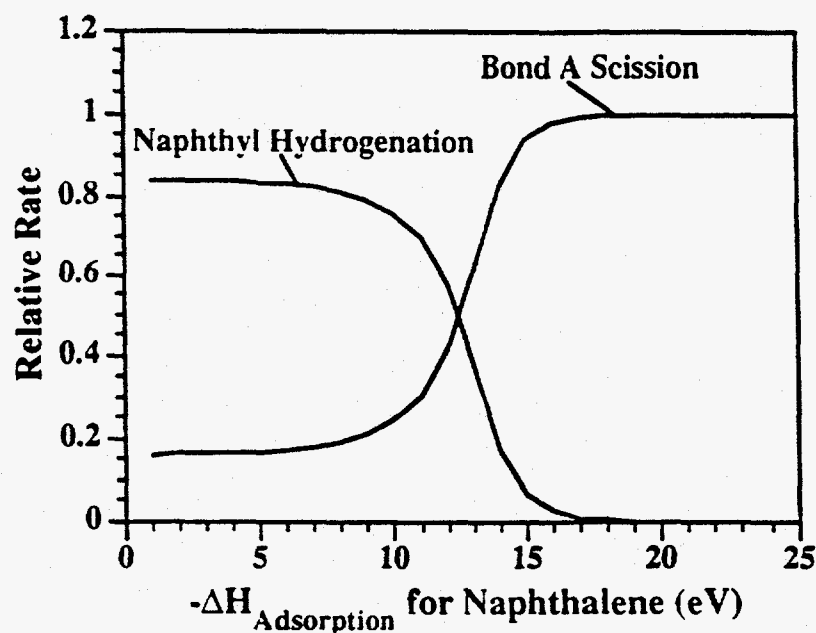
The model was also used to probe the controlling mechanisms of NBBM catalysis. It was found that the naphthalene-metal adsorption interaction controlled the rates and selectivities for NBBM reaction. At the limit of extremely strong naphthalene-metal adsorption, hydrogen was completely displaced from the catalytic surface, preventing NBBM consumption. Similarly, at the limit of extremely weak naphthalene-metal adsorption, naphthalene-containing compounds (NBBM) were displaced from the catalytic surface by hydrogen, also preventing catalytic consumption of NBBM. Intermediate naphthalene-metal adsorption energies provide both bond scission and naphthyl hydrogenation activities. Due to the higher sensitivity of the hydrogenation rate to surface hydrogen concentration, bond scission dominated at stronger naphthalene-metal binding energies and hydrogenation dominated at weaker naphthalene-metal binding energies.

Kinetics-assisted design was carried out using the NBBM mechanistic model to specify the optimal naphthalene-metal interaction, as predicted with the ASED-MO

method. A naphthalene enthalpy of adsorption of 10.5 eV gave the maximum rate of NBBM disappearance. The molecular-level detail provided by the model also allows the elucidation of the catalyst-dependent behavior for individual reaction families. For example, Figure 6.2 shows the relative contribution of the naphthyl hydrogenation and bond A scission reaction families to the overall NBBM consumption. Therefore, mechanistic insight into the reaction of the complex mixture suggesting that bond scission is more important than hydrogenation allows the structure-function relationship to effectively guide specification of an optimal catalyst.

## 6.2 Conclusions

This work demonstrated the feasibility of the construction of molecular-based kinetics models using the reaction family concept. The ability of such models to match experimental data and provide insight into the important reaction pathways and mechanisms of relevant chemical moieties was made apparent. The work also elucidated thermal and catalytic reaction pathways and provided fundamental kinetic parameters, which allow, through the use of linear free energy relationships (LFERs), rate constant specification for pyrolysis and catalysis reaction families in models of the real complex mixtures.



**Figure 6.2** Structure-function relationship for the relative contribution of the hydrogenation and bond scission reaction families to the reaction of NBBM at 400 °C in a hydrogen atmosphere.

NBBM pyrolysis at 420 °C is controlled by bond fission of the weak bibenzyl link and by ipso radical insertion of benzyl or H• radicals at NBBM's aromatic moieties. Subsequent molecular modeling provided additional insight into the formation paths of the product spectra and elucidated a reaction cycle involving  $\beta$ -scission of NBBM-derived radicals on the bibenzyl link to release H•, with subsequent hydrogenation of the olefin to reform NBBM. This reaction cycle effected the transformation of alkyl radicals to the highly reactive H• radicals.

NBBM catalysis at 400 °C revealed a high selectivity to bond A scission products and NBBM naphthyl hydrogenation. For reaction with the catalyst precursors  $\text{Fe}(\text{CO})_4\text{PPh}_3$ ,  $\text{Fe}(\text{CO})_3(\text{PPh}_3)_2$  and  $\text{Fe}(\text{CO})_3(\text{PPh}_3)_2\text{CS}_2$ , the results are inconsistent with a scenario where reduced iron is the active catalytic site, which is able to dissociatively adsorb hydrogen and insert the catalytically bound H atoms in adsorbed naphthalene rings. H addition at the ipso position leads to bond A scission, while continued H



addition leads to hydrogenation. A similar chemistry is proposed on the metal surfaces provided by the transition metal-based catalytic materials  $\text{Fe}(\text{CO})_5$ ,  $\text{Mo}(\text{CO})_6$ ,  $\text{Mn}_2(\text{CO})_{10}$ ,  $\text{Fe}_2\text{O}_3$  and  $\text{MoS}_2$ . Mechanistic modeling of the transition-metal based materials suggests that the naphthalene adsorption energetics on the metal surfaces determines the relative concentrations of catalytically bound H atoms and naphthyl moieties, which ultimately determine the activity and selectivity of the catalytic materials.

The structure-reactivity relationship defined by the catalytic NBBM reaction model through the LFERs provided the opportunity to specify the property of an optimal catalytic material using kinetics-assisted design. The minimum in the reaction half life versus ASED-MO predicted adsorption enthalpy specified 10.5 eV as the optimal naphthyl-metal interaction for NBBM consumption. The three metals, Mo, Pd and Fe were the most active of several materials screened with the computer-aided kinetics-assisted design method. As a result, these three materials provide good starting points for specification of an optimal coal liquefaction catalyst. Even though Fe showed a lightly lower activity for NBBM consumption than the other two, due to its low cost and relative ease of disposal it becomes the most attractive catalyst candidate for coal liquefaction. Now that the intrinsic reactivity of an optimal catalyst material has been determined, the mass transfer effects of solid catalysts in the coal macromolecules require investigation. Specifically, methods for synthesis and characterization of fine particle iron materials is imperative.

The method for investigation and modeling of catalytic reactions systems which has been demonstrated in this work may also be applied to examination of different chemistries important during coal liquefaction such as ring opening, denitrogenation and desulfurization reactions. The method is general and may be applied any other catalytic reaction system to gain insight into reaction pathways and mechanisms and allow estimation of fundamental kinetic parameters for the controlling reaction families.

**Appendix A**

**REACTIONS FOR THE MECHANISTIC MODEL DESCRIBING NBBM  
HYDROLYSIS**

**Table A.1** Reaction listing for the mechanistic model describing NBBM thermal chemistry.

<b>Bond Fission Reactions</b>	
NBBM	$\rightarrow$ Naph-CH <sub>2</sub> -Phen-CH <sub>2</sub> • + Phen-CH <sub>2</sub> •
Phen-CH <sub>2</sub> -CH <sub>2</sub> -Phen-CH <sub>3</sub>	$\rightarrow$ Phen-CH <sub>2</sub> • + CH <sub>3</sub> -Phen-CH <sub>2</sub> •
Phen-CH <sub>2</sub> -CH <sub>2</sub> -Phen	$\rightarrow$ Phen-CH <sub>2</sub> • + Phen-CH <sub>2</sub> •
Phen-CH <sub>2</sub> -CH <sub>2</sub> -Phen-CH <sub>2</sub> -Mu2	$\rightarrow$ Phen-CH <sub>2</sub> -CH <sub>2</sub> -Phen-CH <sub>2</sub> • + Mu2
Phen-CH <sub>2</sub> -CH <sub>2</sub> -Phen-CH <sub>2</sub> -Mu3	$\rightarrow$ Phen-CH <sub>2</sub> -CH <sub>2</sub> -Phen-CH <sub>2</sub> • + Mu3
Naph-CH <sub>2</sub> -Mu2	$\rightarrow$ Naph-CH <sub>2</sub> • + Mu2
Naph-CH <sub>2</sub> -Mu3	$\rightarrow$ Naph-CH <sub>2</sub> • + Mu3
Naph-CH <sub>2</sub> -Phen-CH <sub>2</sub> -Mu2	$\rightarrow$ Naph-CH <sub>2</sub> -Phen-CH <sub>2</sub> • + Mu2
Naph-CH <sub>2</sub> -Phen-CH <sub>2</sub> -Mu3	$\rightarrow$ Naph-CH <sub>2</sub> -Phen-CH <sub>2</sub> • + Mu3
Phen-CH <sub>2</sub> -Mu2	$\rightarrow$ Phen-CH <sub>2</sub> • + Mu2
Phen-CH <sub>2</sub> -Mu3	$\rightarrow$ Phen-CH <sub>2</sub> • + Mu3
CH <sub>3</sub> -Phen-CH <sub>2</sub> -Mu2	$\rightarrow$ CH <sub>3</sub> -Phen-CH <sub>2</sub> • + Mu2
CH <sub>3</sub> -Phen-CH <sub>2</sub> -Mu3	$\rightarrow$ CH <sub>3</sub> -Phen-CH <sub>2</sub> • + Mu3
Mu2-Mu2	$\rightarrow$ Mu2 + Mu2
Mu2-Mu3	$\rightarrow$ Mu2 + Mu3
Mu3-Mu3	$\rightarrow$ Mu3 + Mu3
Tet-NBBM	$\rightarrow$ Tet• + Phen-CH <sub>2</sub> -CH <sub>2</sub> -Phen-CH <sub>2</sub> •
Tet-NBBM	$\rightarrow$ Tet-CH <sub>2</sub> -Phen-CH <sub>2</sub> • + Phen-CH <sub>2</sub> •
Tet-CH <sub>2</sub> -Phen-CH <sub>3</sub>	$\rightarrow$ Tet• + CH <sub>3</sub> -Phen-CH <sub>2</sub> •
Tet-CH <sub>2</sub> -Phen	$\rightarrow$ Tet• + Phen-CH <sub>2</sub> •
Tet-CH <sub>2</sub> -Phen-CH <sub>2</sub> -CH <sub>3</sub>	$\rightarrow$ Tet• + CH <sub>3</sub> -Phen-CH <sub>2</sub> -CH <sub>2</sub> •
<b>Hydrogen Abstraction Reactions</b>	
Phen-CH <sub>2</sub> -CH <sub>2</sub> -Phen-CH <sub>2</sub> • + NBBM	$\rightarrow$ Phen-CH <sub>2</sub> -CH <sub>2</sub> -Phen-CH <sub>3</sub> + Mu2
Phen-CH <sub>2</sub> -CH <sub>2</sub> -Phen-CH <sub>2</sub> • + NBBM	$\rightarrow$ Phen-CH <sub>2</sub> -CH <sub>2</sub> -Phen-CH <sub>3</sub> + Mu3
Phen-CH <sub>2</sub> -CH <sub>2</sub> -Phen-CH <sub>2</sub> • + Tet-NBBM	$\rightarrow$ Phen-CH <sub>2</sub> -CH <sub>2</sub> -Phen-CH <sub>3</sub> + Tet-Mu2
Phen-CH <sub>2</sub> -CH <sub>2</sub> -Phen-CH <sub>2</sub> • + Tet-NBBM	$\rightarrow$ Phen-CH <sub>2</sub> -CH <sub>2</sub> -Phen-CH <sub>3</sub> + Tet-Mu3
Phen-CH <sub>2</sub> -CH <sub>2</sub> -Phen-CH <sub>2</sub> • + Phen-CH <sub>3</sub>	$\rightarrow$ Phen-CH <sub>2</sub> -CH <sub>2</sub> -Phen-CH <sub>3</sub> + Phen-CH <sub>2</sub> •
Phen-CH <sub>2</sub> -CH <sub>2</sub> -Phen-CH <sub>2</sub> • + CH <sub>3</sub> -Phen-CH <sub>3</sub>	$\rightarrow$ Phen-CH <sub>2</sub> -CH <sub>2</sub> -Phen-CH <sub>3</sub> + CH <sub>3</sub> -Phen-CH <sub>2</sub> •
Phen-CH <sub>2</sub> -CH <sub>2</sub> -Phen-CH <sub>2</sub> • + Phen-CH <sub>2</sub> -CH <sub>2</sub> -Phen	$\rightarrow$ Phen-CH <sub>2</sub> -CH <sub>2</sub> -Phen-CH <sub>3</sub> + Phen-CH•-CH <sub>2</sub> -Phen
Phen-CH <sub>2</sub> -CH <sub>2</sub> -Phen-CH <sub>2</sub> • + Phen-CH <sub>2</sub> -CH <sub>2</sub> -Phen-CH <sub>3</sub>	$\rightarrow$ Phen-CH <sub>2</sub> -CH <sub>2</sub> -Phen-CH <sub>3</sub> + Phen-CH•-CH <sub>2</sub> -Phen-CH <sub>3</sub>
Phen-CH <sub>2</sub> -CH <sub>2</sub> -Phen-CH <sub>2</sub> • + Phen-CH <sub>2</sub> -CH <sub>2</sub> -Phen-CH <sub>3</sub>	$\rightarrow$ Phen-CH <sub>2</sub> -CH <sub>2</sub> -Phen-CH <sub>3</sub> + Phen-CH <sub>2</sub> -CH•-Phen-CH <sub>3</sub>
Phen-CH <sub>2</sub> -CH <sub>2</sub> -Phen-CH <sub>2</sub> • + Naph-CH <sub>2</sub> -Phen-CH <sub>2</sub> -CH <sub>3</sub>	$\rightarrow$ Phen-CH <sub>2</sub> -CH <sub>2</sub> -Phen-CH <sub>3</sub> + Naph-CH <sub>2</sub> -Phen-CH <sub>2</sub> -CH <sub>2</sub> •
Phen-CH <sub>2</sub> -CH <sub>2</sub> -Phen-CH <sub>2</sub> • + Tet-CH <sub>2</sub> -Phen-CH <sub>2</sub> -CH <sub>3</sub>	$\rightarrow$ Phen-CH <sub>2</sub> -CH <sub>2</sub> -Phen-CH <sub>3</sub> + Tet-CH <sub>2</sub> -Phen-CH <sub>2</sub> -CH <sub>2</sub> •
Phen-CH <sub>2</sub> -CH <sub>2</sub> -Phen-CH <sub>2</sub> • + H <sub>2</sub>	$\rightarrow$ Phen-CH <sub>2</sub> -CH <sub>2</sub> -Phen-CH <sub>3</sub> + H•
Naph-CH <sub>2</sub> • + NBBM	$\rightarrow$ Naph-CH <sub>3</sub> + Mu2
Naph-CH <sub>2</sub> • + NBBM	$\rightarrow$ Naph-CH <sub>3</sub> + Mu3
Naph-CH <sub>2</sub> • + Tet-NBBM	$\rightarrow$ Naph-CH <sub>3</sub> + Tet-Mu2
Naph-CH <sub>2</sub> • + Tet-NBBM	$\rightarrow$ Naph-CH <sub>3</sub> + Tet-Mu3
Naph-CH <sub>2</sub> • + Phen-CH <sub>3</sub>	$\rightarrow$ Naph-CH <sub>3</sub> + Phen-CH <sub>2</sub> •
Naph-CH <sub>2</sub> • + CH <sub>3</sub> -Phen-CH <sub>3</sub>	$\rightarrow$ Naph-CH <sub>3</sub> + CH <sub>3</sub> -Phen-CH <sub>2</sub> •
Naph-CH <sub>2</sub> • + Phen-CH <sub>2</sub> -CH <sub>2</sub> -Phen	$\rightarrow$ Naph-CH <sub>3</sub> + Phen-CH•-CH <sub>2</sub> -Phen
Naph-CH <sub>2</sub> • + Phen-CH <sub>2</sub> -CH <sub>2</sub> -Phen-CH <sub>3</sub>	$\rightarrow$ Naph-CH <sub>3</sub> + Phen-CH•-CH <sub>2</sub> -Phen-CH <sub>3</sub>
Naph-CH <sub>2</sub> • + Phen-CH <sub>2</sub> -CH <sub>2</sub> -Phen-CH <sub>3</sub>	$\rightarrow$ Naph-CH <sub>3</sub> + Phen-CH <sub>2</sub> -CH•-Phen-CH <sub>3</sub>
Naph-CH <sub>2</sub> • + Phen-CH <sub>2</sub> -CH <sub>2</sub> -Phen-CH <sub>3</sub>	$\rightarrow$ Naph-CH <sub>3</sub> + Phen-CH <sub>2</sub> -CH <sub>2</sub> -Phen-CH <sub>2</sub> •
Naph-CH <sub>2</sub> • + Naph-CH <sub>2</sub> -Phen-CH <sub>2</sub> -CH <sub>3</sub>	$\rightarrow$ Naph-CH <sub>3</sub> + Naph-CH•-Phen-CH <sub>2</sub> -CH <sub>3</sub>

























Table A.1 continued

<b>Radical Hydrogen Transfer Reactions</b>	
Tet-NBBM + NBBM	$\rightarrow \text{Tet}\cdot\text{-NBBM} + \text{Naph(H)CH}_2\text{-Phen-CH}_2\text{-CH}_2\text{-Phen}$
Tet-CH <sub>2</sub> -Phen-CH <sub>2</sub> -CH <sub>3</sub> + NBBM	$\rightarrow \text{Tet}\cdot\text{-CH}_2\text{-Phen-CH}_2\text{-CH}_3 + \text{Naph(H)CH}_2\text{-Phen-CH}_2\text{-CH}_2\text{-Phen}$
Tet-CH <sub>2</sub> -Phen-CH=CH <sub>2</sub> + NBBM	$\rightarrow \text{Tet}\cdot\text{-CH}_2\text{-Phen-CH=CH}_2 + \text{Naph(H)CH}_2\text{-Phen-CH}_2\text{-CH}_2\text{-Phen}$
Tet-CH <sub>2</sub> -Phen-CH <sub>3</sub> + NBBM	$\rightarrow \text{Tet}\cdot\text{-CH}_2\text{-Phen-CH}_3 + \text{Naph(H)CH}_2\text{-Phen-CH}_2\text{-CH}_2\text{-Phen}$
Tet-CH <sub>2</sub> -Phen + NBBM	$\rightarrow \text{Tet}\cdot\text{-CH}_2\text{-Phen} + \text{Naph(H)CH}_2\text{-Phen-CH}_2\text{-CH}_2\text{-Phen}$
Tet-CH <sub>3</sub> + NBBM	$\rightarrow \text{Tet}\cdot\text{-CH}_3 + \text{Naph(H)CH}_2\text{-Phen-CH}_2\text{-CH}_2\text{-Phen}$
Tetralin + NBBM	$\rightarrow \text{Tet}\cdot + \text{Naph(H)CH}_2\text{-Phen-CH}_2\text{-CH}_2\text{-Phen}$
Tet-NBBM + Naph-CH <sub>2</sub> -Phen-CH <sub>2</sub> -CH <sub>3</sub>	$\rightarrow \text{Tet}\cdot\text{-NBBM} + \text{Naph(H)CH}_2\text{-Phen-CH}_2\text{-CH}_3$
Tet-CH <sub>2</sub> -Phen-CH <sub>2</sub> -CH <sub>3</sub> + Naph-CH <sub>2</sub> -Phen-CH <sub>2</sub> -CH <sub>3</sub>	$\rightarrow$
Tet-CH <sub>2</sub> -Phen-CH <sub>2</sub> -CH <sub>3</sub> + Naph(H)CH <sub>2</sub> -Phen-CH <sub>2</sub> -CH <sub>3</sub>	$\rightarrow$
Tet-CH <sub>2</sub> -Phen-CH=CH <sub>2</sub> + Naph-CH <sub>2</sub> -Phen-CH <sub>2</sub> -CH <sub>3</sub>	$\rightarrow$
Tet-CH <sub>2</sub> -Phen-CH=CH <sub>2</sub> + Naph(H)CH <sub>2</sub> -Phen-CH <sub>2</sub> -CH <sub>3</sub>	$\rightarrow$
Tet-CH <sub>2</sub> -Phen-CH <sub>3</sub> + Naph-CH <sub>2</sub> -Phen-CH <sub>2</sub> -CH <sub>3</sub>	$\rightarrow \text{Tet}\cdot\text{-CH}_2\text{-Phen-CH}_3 + \text{Naph(H)CH}_2\text{-Phen-CH}_2\text{-CH}_3$
Tet-CH <sub>2</sub> -Phen + Naph-CH <sub>2</sub> -Phen-CH <sub>2</sub> -CH <sub>3</sub>	$\rightarrow \text{Tet}\cdot\text{-CH}_2\text{-Phen} + \text{Naph(H)CH}_2\text{-Phen-CH}_2\text{-CH}_3$
Tet-CH <sub>3</sub> + Naph-CH <sub>2</sub> -Phen-CH <sub>2</sub> -CH <sub>3</sub>	$\rightarrow \text{Tet}\cdot\text{-CH}_3 + \text{Naph(H)CH}_2\text{-Phen-CH}_2\text{-CH}_3$
Tetralin + Naph-CH <sub>2</sub> -Phen-CH <sub>2</sub> -CH <sub>3</sub>	$\rightarrow \text{Tet}\cdot + \text{Naph(H)CH}_2\text{-Phen-CH}_2\text{-CH}_3$
Tet-NBBM + Naph-CH <sub>2</sub> -Phen-CH=CH <sub>2</sub>	$\rightarrow \text{Tet}\cdot\text{-NBBM} + \text{Naph(H)CH}_2\text{-Phen-CH=CH}_2$
Tet-CH <sub>2</sub> -Phen-CH <sub>2</sub> -CH <sub>3</sub> + Naph-CH <sub>2</sub> -Phen-CH=CH <sub>2</sub>	$\rightarrow$
Tet-CH <sub>2</sub> -Phen-CH <sub>2</sub> -CH <sub>3</sub> + Naph(H)CH <sub>2</sub> -Phen-CH=CH <sub>2</sub>	$\rightarrow$
Tet-CH <sub>2</sub> -Phen-CH=CH <sub>2</sub> + Naph-CH <sub>2</sub> -Phen-CH=CH <sub>2</sub>	$\rightarrow$
Tet-CH <sub>2</sub> -Phen-CH=CH <sub>2</sub> + Naph(H)CH <sub>2</sub> -Phen-CH=CH <sub>2</sub>	$\rightarrow$
Tet-CH <sub>2</sub> -Phen-CH <sub>3</sub> + Naph-CH <sub>2</sub> -Phen-CH=CH <sub>2</sub>	$\rightarrow \text{Tet}\cdot\text{-CH}_2\text{-Phen-CH}_3 + \text{Naph(H)CH}_2\text{-Phen-CH=CH}_2$
Tet-CH <sub>2</sub> -Phen + Naph-CH <sub>2</sub> -Phen-CH=CH <sub>2</sub>	$\rightarrow \text{Tet}\cdot\text{-CH}_2\text{-Phen} + \text{Naph(H)CH}_2\text{-Phen-CH=CH}_2$
Tet-CH <sub>3</sub> + Naph-CH <sub>2</sub> -Phen-CH=CH <sub>2</sub>	$\rightarrow \text{Tet}\cdot\text{-CH}_3 + \text{Naph(H)CH}_2\text{-Phen-CH=CH}_2$
Tetralin + Naph-CH <sub>2</sub> -Phen-CH=CH <sub>2</sub>	$\rightarrow \text{Tet}\cdot + \text{Naph(H)CH}_2\text{-Phen-CH=CH}_2$
Tet-NBBM + Naph-CH <sub>2</sub> -Phen-CH <sub>3</sub>	$\rightarrow \text{Tet}\cdot\text{-NBBM} + \text{Naph(H)CH}_2\text{-Phen-CH}_3$
Tet-CH <sub>2</sub> -Phen-CH <sub>2</sub> -CH <sub>3</sub> + Naph-CH <sub>2</sub> -Phen-CH <sub>3</sub>	$\rightarrow \text{Tet}\cdot\text{-CH}_2\text{-Phen-CH}_2\text{-CH}_3 + \text{Naph(H)CH}_2\text{-Phen-CH}_3$
Tet-CH <sub>2</sub> -Phen-CH=CH <sub>2</sub> + Naph-CH <sub>2</sub> -Phen-CH <sub>3</sub>	$\rightarrow \text{Tet}\cdot\text{-CH}_2\text{-Phen-CH=CH}_2 + \text{Naph(H)CH}_2\text{-Phen-CH}_3$
Tet-CH <sub>2</sub> -Phen-CH <sub>3</sub> + Naph-CH <sub>2</sub> -Phen-CH <sub>3</sub>	$\rightarrow \text{Tet}\cdot\text{-CH}_2\text{-Phen-CH}_3 + \text{Naph(H)CH}_2\text{-Phen-CH}_3$
Tet-CH <sub>2</sub> -Phen + Naph-CH <sub>2</sub> -Phen-CH <sub>3</sub>	$\rightarrow \text{Tet}\cdot\text{-CH}_2\text{-Phen} + \text{Naph(H)CH}_2\text{-Phen-CH}_3$
Tet-CH <sub>3</sub> + Naph-CH <sub>2</sub> -Phen-CH <sub>3</sub>	$\rightarrow \text{Tet}\cdot\text{-CH}_3 + \text{Naph(H)CH}_2\text{-Phen-CH}_3$
Tetralin + Naph-CH <sub>2</sub> -Phen-CH <sub>3</sub>	$\rightarrow \text{Tet}\cdot + \text{Naph(H)CH}_2\text{-Phen-CH}_3$
Tet-NBBM + Naph-CH <sub>2</sub> -Phen	$\rightarrow \text{Tet}\cdot\text{-NBBM} + \text{Naph(H)CH}_2\text{-Phen}$
Tet-CH <sub>2</sub> -Phen-CH <sub>2</sub> -CH <sub>3</sub> + Naph-CH <sub>2</sub> -Phen	$\rightarrow \text{Tet}\cdot\text{-CH}_2\text{-Phen-CH}_2\text{-CH}_3 + \text{Naph(H)CH}_2\text{-Phen}$
Tet-CH <sub>2</sub> -Phen-CH=CH <sub>2</sub> + Naph-CH <sub>2</sub> -Phen	$\rightarrow \text{Tet}\cdot\text{-CH}_2\text{-Phen-CH=CH}_2 + \text{Naph(H)CH}_2\text{-Phen}$
Tet-CH <sub>2</sub> -Phen-CH <sub>3</sub> + Naph-CH <sub>2</sub> -Phen	$\rightarrow \text{Tet}\cdot\text{-CH}_2\text{-Phen-CH}_3 + \text{Naph(H)CH}_2\text{-Phen}$
Tet-CH <sub>2</sub> -Phen + Naph-CH <sub>2</sub> -Phen	$\rightarrow \text{Tet}\cdot\text{-CH}_2\text{-Phen} + \text{Naph(H)CH}_2\text{-Phen}$
Tet-CH <sub>3</sub> + Naph-CH <sub>2</sub> -Phen	$\rightarrow \text{Tet}\cdot\text{-CH}_3 + \text{Naph(H)CH}_2\text{-Phen}$
Tetralin + Naph-CH <sub>2</sub> -Phen	$\rightarrow \text{Tet}\cdot + \text{Naph(H)CH}_2\text{-Phen}$
<b>Radical Elimination Reactions</b>	
Naph(H)CH <sub>2</sub> -Phen-CH <sub>2</sub> -CH <sub>2</sub> -Phen	$\rightarrow \text{Naph} + \text{Phen-CH}_2\text{-CH}_2\text{-Phen-CH}_2\cdot$
Naph(CH <sub>2</sub> -Phen)CH <sub>2</sub> -Phen-CH <sub>2</sub> -CH <sub>2</sub> -Phen	$\rightarrow \text{Naph-CH}_2\text{-Phen} + \text{Phen-CH}_2\text{-CH}_2\text{-Phen-CH}_2\cdot$
Naph(CH <sub>2</sub> -Phen)CH <sub>2</sub> -Phen-CH <sub>2</sub> -CH <sub>2</sub> -Phen	$\rightarrow \text{NBBM} + \text{Phen-CH}_2\cdot$
Naph(CH <sub>2</sub> -Phen-CH <sub>3</sub> )CH <sub>2</sub> -Phen-CH <sub>2</sub> -CH <sub>2</sub> -Phen	$\rightarrow \text{Naph-CH}_2\text{-Phen-CH}_3 + \text{Phen-CH}_2\text{-CH}_2\text{-Phen-CH}_2\cdot$
Naph(CH <sub>2</sub> -Phen-CH <sub>3</sub> )CH <sub>2</sub> -Phen-CH <sub>2</sub> -CH <sub>2</sub> -Phen	$\rightarrow \text{NBBM} + \text{CH}_3\text{-Phen-CH}_2\cdot$
Naph(CH <sub>2</sub> -Phen-CH=CH <sub>2</sub> )CH <sub>2</sub> -Phen-CH <sub>2</sub> -CH <sub>2</sub> -Phen	$\rightarrow$
Naph-CH <sub>2</sub> -Phen-CH=CH <sub>2</sub> + Phen-CH <sub>2</sub> -CH <sub>2</sub> -Phen-CH <sub>2</sub> ·	$\rightarrow$
Naph(CH <sub>2</sub> -Phen-CH=CH <sub>2</sub> )CH <sub>2</sub> -Phen-CH <sub>2</sub> -CH <sub>2</sub> -Phen	$\rightarrow \text{CH}_2\cdot\text{-Phen-CH=CH}_2 + \text{NBBM}$































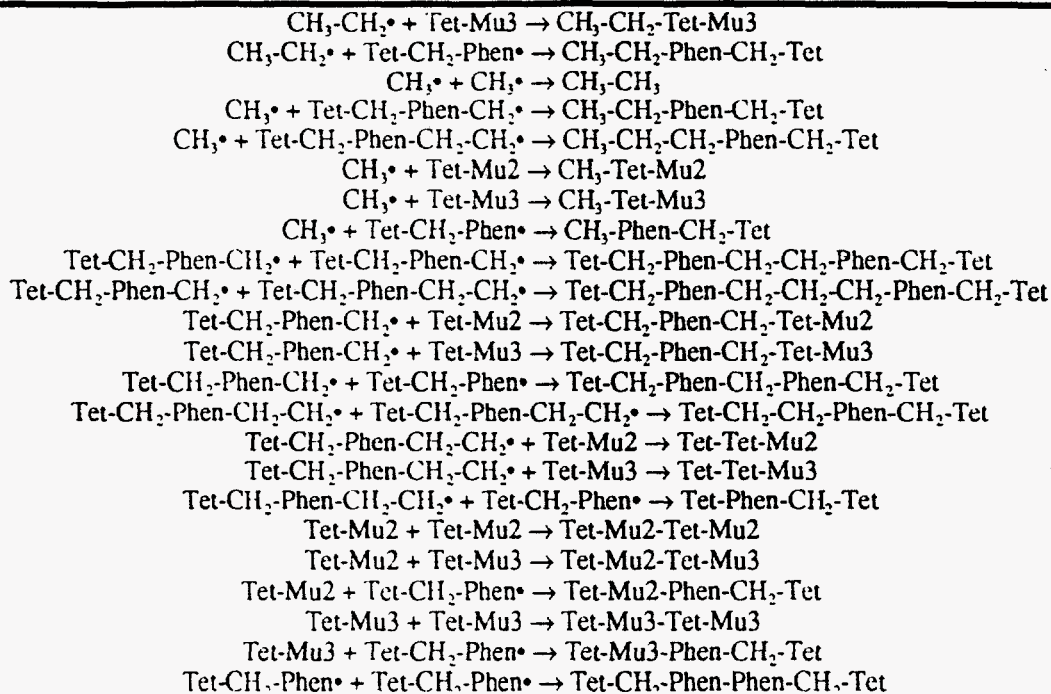








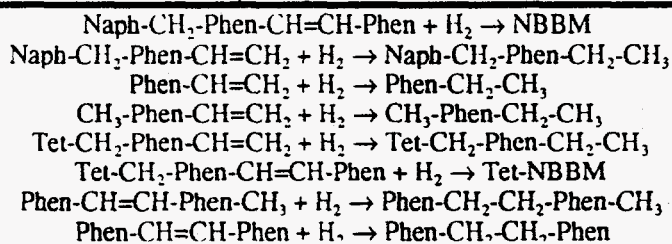
Table A.1 continued




---

**Olefin Hydrogenation Reactions**

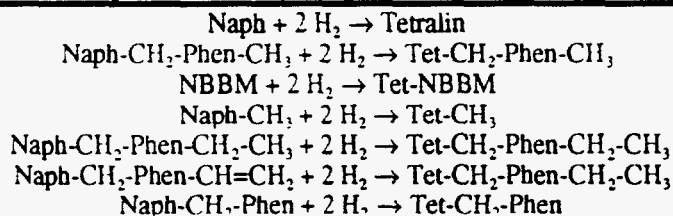

---




---

**Naphthalene Hydrogenation Reactions**


---



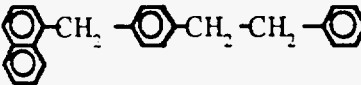
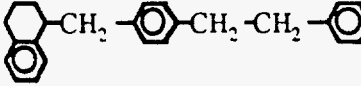

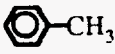
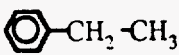
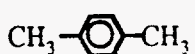
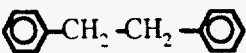
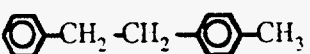


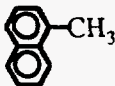
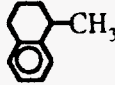
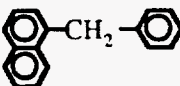
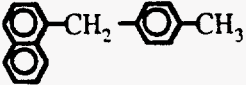
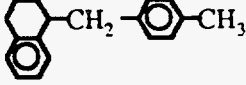
## **Appendix B**

### **EXPERIMENTAL DATA FOR NBBM REACTIONS**

This appendix contains the experimental data for NBBM pyrolysis and catalysis which was reported on in this document. Table B.1 contains the product codes used in Tables B.2-B.15 which list the reaction conditions and measured product yields.



**Table B.1** Product Codes for the NBBM reactions' observed product spectra.

Product Name	Product Structure	Product Code
NBBM		1
Tetrahydro-NBBM		2
Benzene		3
Toluene		4
Ethylbenzene		5
p-Xylene		6
Bibenzyl		7
Methylbibenzyl		8
Naphthalene		9
Tetralin		10
Methylnaphthalene		11
Methyltetralin		12
Naphthylphenylmethane		13
Naphthyltolylmethane		14
Tetrahydronaphthyltolylmethane		15

**Table B.2** NBBM pyrolysis results at 420 °C under a nitrogen atmosphere.

T = 420 °C, 0.05 g NBBM, 1000 psig N <sub>2</sub> (cold)					
Molar Yields of Products					
Product Code	Reaction Time (Minutes)				
	30	60	90	120	150
1	0.924	0.797	0.645	0.505	0.406
2	0.000	0.000	0.000	0.000	0.000
3	0.022	0.021	0.006	0.028	0.020
4	0.019	0.035	0.069	0.067	0.108
5	0.000	0.000	0.000	0.000	0.000
6	0.000	0.000	0.004	0.005	0.011
7	0.000	0.000	0.000	0.001	0.003
8	0.005	0.010	0.018	0.022	0.029
9	0.000	0.001	0.005	0.006	0.011
10	0.000	0.000	0.000	0.000	0.000
11	0.000	0.000	0.005	0.006	0.010
12	0.000	0.000	0.000	0.000	0.000
13	0.002	0.008	0.015	0.024	0.034
14	0.031	0.057	0.091	0.108	0.131
15	0.000	0.000	0.000	0.000	0.000

**Table B.3** NBBM pyrolysis results at 420 °C under a hydrogen atmosphere.

T = 420 °C, 0.05 g NBBM, 1000 psig H <sub>2</sub> (cold)					
Molar Yields of Products					
Product Code	Reaction Time (Minutes)				
	30	60	90	120	150
1	0.941	0.839	0.741	0.671	0.599
2	0.005	0.010	0.014	0.016	0.018
3	0.015	0.015	0.000	0.009	0.000
4	0.020	0.051	0.069	0.096	0.110
5	0.000	0.000	0.000	0.000	0.000
6	0.003	0.011	0.019	0.028	0.039
7	0.002	0.006	0.008	0.009	0.012
8	0.016	0.032	0.042	0.048	0.057
9	0.014	0.031	0.045	0.059	0.078
10	0.000	0.002	0.002	0.004	0.008
11	0.003	0.006	0.009	0.010	0.012
12	0.000	0.000	0.000	0.000	0.000
13	0.006	0.006	0.015	0.020	0.018
14	0.027	0.059	0.085	0.098	0.104
15	0.000	0.000	0.000	0.000	0.000

**Table B.4** NBBM pyrolysis results at 420 °C under a hydrogen atmosphere.

T = 420 °C, 0.10 g NBBM, 1000 psig H <sub>2</sub> (cold)												
Molar Yields of Products												
Product Code	Reaction Time (Minutes)											
	30	60	90	120	150	180	210	240	270	300	330	370
1	0.936	0.835	0.774	0.714	0.639	0.572	0.533	0.493	0.421	0.360	0.347	0.265
2	0.004	0.012	0.016	0.021	0.020	0.026	0.026	0.027	0.027	0.026	0.027	0.025
3	0.003	0.005	0.010	0.015	0.018	0.026	0.031	0.033	0.041	0.040	0.054	0.067
4	0.023	0.054	0.072	0.102	0.122	0.152	0.177	0.191	0.252	0.266	0.286	0.339
5	0.003	0.006	0.008	0.010	0.012	0.016	0.022	0.019	0.028	0.028	0.037	0.042
6	0.001	0.005	0.009	0.014	0.020	0.032	0.044	0.042	0.076	0.087	0.102	0.127
7	0.003	0.006	0.008	0.010	0.012	0.013	0.013	0.013	0.017	0.021	0.018	0.022
8	0.021	0.040	0.051	0.063	0.068	0.072	0.071	0.072	0.091	0.087	0.089	0.102
9	0.019	0.035	0.052	0.069	0.087	0.105	0.107	0.117	0.171	0.211	0.172	0.237
10	0.003	0.006	0.007	0.010	0.008	0.018	0.025	0.018	0.030	0.019	0.071	0.070
11	0.004	0.006	0.009	0.012	0.013	0.015	0.014	0.017	0.020	0.027	0.018	0.023
12	0.000	0.000	0.000	0.000	0.000	0.000	0.001	0.000	0.002	0.006	0.004	0.003
13	0.010	0.010	0.034	0.042	0.036	0.027	0.019	0.025	0.028	0.021	0.026	0.035
14	0.032	0.059	0.094	0.124	0.136	0.143	0.128	0.150	0.147	0.136	0.130	0.138
15	0.000	0.001	0.009	0.012	0.013	0.005	0.002	0.003	0.005	0.002	0.008	0.013

**Table B.5** NBBM pyrolysis results at 400 °C under a hydrogen atmosphere.

<b>T = 400 °C, 0.10 g NBBM, 1000 psig H<sub>2</sub> (cold)</b>					
<b>Molar Yields of Products</b>					
<b>Product Code</b>	<b>Reaction Time (Minutes)</b>				
	<b>30</b>	<b>45</b>	<b>60</b>	<b>75</b>	<b>90</b>
1	0.986	0.977	0.954	0.950	0.933
2	0.009	0.004	0.007	0.005	0.006
3	0.000	0.001	0.002	0.001	0.002
4	0.007	0.012	0.013	0.013	0.019
5	0.002	0.002	0.002	0.002	0.003
6	0.001	0.001	0.001	0.001	0.002
7	0.005	0.003	0.005	0.004	0.008
8	0.023	0.016	0.019	0.026	0.031
9	0.017	0.015	0.020	0.020	0.037
10	0.007	0.003	0.004	0.008	0.005
11	0.002	0.002	0.003	0.002	0.005
12	0.001	0.000	0.001	0.001	0.002
13	0.002	0.003	0.003	0.006	0.004
14	0.008	0.013	0.014	0.018	0.021
15	0.001	0.000	0.000	0.000	0.000

**Table B.6** NBBM catalysis results at 420 °C with  $\text{Fe}(\text{CO})_3(\text{PPh}_3)_2$  under a nitrogen atmosphere.

<b>T = 420 °C, 0.05 g NBBM, 8 mg <math>\text{Fe}(\text{CO})_3(\text{PPh}_3)_2</math>, 1000 psig <math>\text{N}_2</math> (cold)</b>					
<b>Molar Yields of Products</b>					
<b>Product Code</b>	<b>Reaction Time (Minutes)</b>				
	<b>30</b>	<b>60</b>	<b>90</b>	<b>120</b>	<b>150</b>
1	0.896	0.753	0.638	0.518	0.341
2	0.000	0.000	0.000	0.000	0.000
3	0.000	0.000	0.000	0.000	0.000
4	0.009	0.031	0.053	0.077	0.087
5	0.000	0.000	0.000	0.000	0.000
6	0.000	0.000	0.000	0.006	0.01
7	0.000	0.000	0.000	0.002	0.004
8	0.007	0.014	0.018	0.025	0.027
9	0.000	0.004	0.006	0.010	0.011
10	0.000	0.000	0.000	0.000	0.000
11	0.000	0.002	0.006	0.008	0.011
12	0.000	0.000	0.000	0.000	0.000
13	0.004	0.010	0.016	0.024	0.033
14	0.032	0.060	0.086	0.113	0.119
15	0.000	0.000	0.000	0.000	0.000

**Table B.7** NBBM catalysis results at 420 °C with  $\text{Fe}(\text{CO})_3(\text{PPh}_3)_2$  under a hydrogen atmosphere.

<b>T = 420 °C, 0.05 g NBBM, 8 mg <math>\text{Fe}(\text{CO})_3(\text{PPh}_3)_2</math>, 1000 psig <math>\text{H}_2</math> (cold)</b>					
<b>Molar Yields of Products</b>					
<b>Product Code</b>	<b>Reaction Time (Minutes)</b>				
	<b>30</b>	<b>60</b>	<b>90</b>	<b>120</b>	<b>150</b>
1	0.740	0.480	0.390	0.110	0.043
2	0.070	0.141	0.137	0.170	0.149
3	0.240	0.270	0.246	0.276	0.289
4	0.035	0.063	0.087	0.135	0.171
5	0.000	0.000	0.000	0.000	0.000
6	0.005	0.019	0.031	0.072	0.100
7	0.072	0.176	0.194	0.269	0.264
8	0.077	0.195	0.226	0.341	0.364
9	0.047	0.097	0.110	0.139	0.137
10	0.024	0.083	0.095	0.174	0.197
11	0.002	0.005	0.007	0.007	0.007
12	0.000	0.000	0.000	0.004	0.006
13	0.003	0.010	0.012	0.021	0.031
14	0.033	0.013	0.022	0.013	0.003
15	0.000	0.000	0.001	0.003	0.007

**Table B.8** NBBM catalysis results at 400 °C with Fe(CO)<sub>4</sub>PPh<sub>3</sub> under a hydrogen atmosphere.

T = 400 °C, 0.05 g NBBM, 5 mg Fe(CO) <sub>4</sub> PPh <sub>3</sub> , 1000 psig H <sub>2</sub> (cold)					
Molar Yields of Products					
Product Code	Reaction Time (Minutes)				
	30	60	90	120	150
1	0.930	0.399	0.082	0.031	0.020
2	0.046	0.383	0.526	0.477	0.423
3	0.099	0.128	0.158	0.127	0.174
4	0.009	0.020	0.036	0.051	0.052
5	0.000	0.000	0.000	0.000	0.000
6	0.000	0.005	0.016	0.031	0.037
7	0.000	0.003	0.007	0.007	0.013
8	0.019	0.090	0.158	0.201	0.209
9	0.014	0.040	0.040	0.032	0.029
10	0.004	0.049	0.117	0.177	0.185
11	0.000	0.002	0.002	0.003	0.003
12	0.000	0.000	0.005	0.010	0.012
13	0.000	0.010	0.006	0.006	0.005
14	0.006	0.022	0.007	0.005	0.005
15	0.000	0.010	0.012	0.017	0.017



**Table B.9** NBBM catalysis results at 400 °C with  $\text{Fe}(\text{CO})_3(\text{PPh}_3)_2$  under a hydrogen atmosphere.

T = 400 °C, 0.05 g NBBM, 8 mg $\text{Fe}(\text{CO})_3(\text{PPh}_3)_2$ , 1000 psig $\text{H}_2$ (cold)					
Molar Yields of Products					
Product Code	Reaction Time (Minutes)				
	30	60	90	120	150
1	0.843	0.713	0.537	0.426	0.270
2	0.054	0.131	0.227	0.253	0.309
3	0.198	0.212	0.222	0.230	0.260
4	0.012	0.022	0.028	0.036	0.052
5	0.000	0.000	0.000	0.000	0.000
6	0.000	0.000	0.009	0.013	0.026
7	0.000	0.000	0.004	0.006	0.011
8	0.027	0.065	0.128	0.163	0.216
9	0.021	0.041	0.065	0.075	0.095
10	0.007	0.021	0.060	0.084	0.128
11	0.000	0.000	0.003	0.003	0.004
12	0.000	0.000	0.001	0.001	0.002
13	0.000	0.000	0.003	0.003	0.002
14	0.006	0.013	0.017	0.020	0.016
15	0.000	0.000	0.003	0.005	0.008

**Table B.10** NBBM catalysis results at 400 °C with  $\text{Fe}(\text{CO})_2(\text{PPh}_3)_2\text{CS}_2$  under a hydrogen atmosphere.

T = 400 °C, 0.05 g NBBM, 8.3 mg $\text{Fe}(\text{CO})_2(\text{PPh}_3)_2\text{CS}_2$ , 1000 psig $\text{H}_2$ (cold)					
Molar Yields of Products					
Product Code	Reaction Time (Minutes)				
	30	60	90	120	150
1	0.903	0.838	0.555	0.151	0.098
2	0.003	0.018	0.214	0.398	0.371
3	0.011	0.024	0.163	0.161	0.196
4	0.007	0.011	0.018	0.032	0.049
5	0.000	0.000	0.000	0.000	0.000
6	0.000	0.001	0.003	0.015	0.026
7	0.000	0.000	0.004	0.004	0.012
8	0.013	0.032	0.114	0.259	0.296
9	0.010	0.026	0.082	0.122	0.127
10	0.000	0.003	0.028	0.131	0.173
11	0.000	0.000	0.004	0.005	0.005
12	0.000	0.000	0.000	0.003	0.005
13	0.000	0.001	0.006	0.007	0.006
14	0.009	0.014	0.020	0.013	0.011
15	0.000	0.000	0.008	0.009	0.012

**Table B.11** NBBM catalysis results at 400 °C with Fe(CO)<sub>5</sub> under a hydrogen atmosphere.

T = 400 °C, 0.10 g NBBM, 8.8 mg Fe(CO) <sub>5</sub> , 1000 psig H <sub>2</sub> (cold)						
Molar Yields of Products						
Product Code	Reaction Time (Minutes)					
	15	30	45	60	75	90
1	0.923	0.752	0.402	0.269	0.185	0.070
2	0.050	0.160	0.465	0.536	0.569	0.585
3	0.000	0.001	0.002	0.004	0.005	0.008
4	0.003	0.006	0.011	0.016	0.021	0.032
5	0.001	0.001	0.003	0.005	0.006	0.009
6	0.000	0.001	0.001	0.003	0.005	0.010
7	0.004	0.004	0.005	0.006	0.008	0.012
8	0.019	0.028	0.065	0.091	0.118	0.170
9	0.012	0.014	0.019	0.018	0.018	0.025
10	0.003	0.015	0.052	0.080	0.112	0.165
11	0.002	0.002	0.003	0.003	0.003	0.004
12	0.000	0.001	0.002	0.003	0.004	0.006
13	0.003	0.005	0.008	0.008	0.012	0.009
14	0.003	0.007	0.007	0.008	0.013	0.006
15	0.000	0.004	0.006	0.011	0.019	0.022

**Table B.12** NBBM catalysis results at 400 °C with Mo(CO)<sub>6</sub> under a hydrogen atmosphere.

<b>T = 400 °C, 0.10 g NBBM, 11.8 mg Mo(CO)<sub>6</sub>, 1000 psig H<sub>2</sub> (cold)</b>						
<b>Molar Yields of Products</b>						
<b>Product Code</b>	<b>Reaction Time (Minutes)</b>					
	<b>15</b>	<b>30</b>	<b>45</b>	<b>60</b>	<b>75</b>	<b>90</b>
1	0.667	0.436	0.267	0.189	0.114	0.044
2	0.059	0.158	0.209	0.2	0.181	0.147
3	0.001	0.003	0.004	0.005	0.008	0.010
4	0.003	0.009	0.017	0.021	0.03	0.039
5	0.001	0.003	0.006	0.007	0.01	0.012
6	0.001	0.003	0.007	0.009	0.013	0.017
7	0.031	0.042	0.054	0.061	0.07	0.081
8	0.128	0.22	0.29	0.334	0.354	0.396
9	0.144	0.164	0.155	0.192	0.163	0.136
10	0.036	0.106	0.192	0.204	0.261	0.34
11	0.023	0.027	0.028	0.033	0.034	0.031
12	0.006	0.01	0.016	0.018	0.024	0.032
13	0.004	0.007	0.007	0.013	0.01	0.011
14	0.001	0.006	0.006	0.012	0.008	0.005
15	0.002	0.005	0.007	0.011	0.011	0.011

**Table B.13** NBBM catalysis results at 400 °C with  $\text{Mn}_2(\text{CO})_{10}$  under a hydrogen atmosphere.

T = 400 °C, 0.10 g NBBM, 8.7 mg $\text{Mn}_2(\text{CO})_{10}$ , 1000 psig $\text{H}_2$ (cold)						
Molar Yields of Products						
Product Code	Reaction Time (Minutes)					
	15	30	45	60	75	90
1	1.004	0.932	0.968	0.982	0.914	0.922
2	0.013	0.017	0.011	0.013	0.019	0.015
3	0.000	0.002	0.000	0.000	0.002	0.002
4	0.002	0.013	0.008	0.006	0.014	0.012
5	0.000	0.002	0.001	0.001	0.002	0.002
6	0.000	0.001	0.000	0.000	0.001	0.000
7	0.003	0.005	0.005	0.002	0.000	0.003
8	0.006	0.031	0.019	0.010	0.027	0.024
9	0.005	0.027	0.018	0.009	0.022	0.020
10	0.003	0.009	0.005	0.001	0.010	0.006
11	0.000	0.003	0.003	0.002	0.003	0.003
12	0.000	0.001	0.000	0.001	0.000	0.001
13	0.000	0.008	0.011	0.003	0.019	0.004
14	0.004	0.018	0.014	0.008	0.036	0.016
15	0.000	0.002	0.000	0.000	0.004	0.001

**Table B.14** NBBM catalysis results at 400 °C with Fe<sub>2</sub>O<sub>3</sub> under a hydrogen atmosphere.

T = 400 °C, 0.10 g NBBM, 3.6 mg Fe <sub>2</sub> O <sub>3</sub> , 1000 psig H <sub>2</sub> (cold)						
Molar Yields of Products						
Product Code	Reaction Time (Minutes)					
	15	30	45	60	75	90
1	0.905	0.819	0.711	0.559	0.464	0.287
2	0.080	0.122	0.184	0.277	0.314	0.365
3	0.000	0.000	0.002	0.002	0.003	0.005
4	0.003	0.006	0.009	0.014	0.018	0.025
5	0.001	0.001	0.002	0.003	0.004	0.006
6	0.000	0.000	0.001	0.002	0.003	0.008
7	0.002	0.003	0.006	0.007	0.007	0.013
8	0.016	0.030	0.054	0.090	0.102	0.158
9	0.010	0.019	0.031	0.045	0.042	0.053
10	0.005	0.014	0.027	0.051	0.068	0.123
11	0.001	0.002	0.003	0.004	0.005	0.009
12	0.000	0.001	0.001	0.002	0.002	0.005
13	0.006	0.014	0.009	0.017	0.008	0.011
14	0.006	0.010	0.011	0.022	0.015	0.018
15	0.002	0.006	0.004	0.020	0.009	0.017

**Table B.15** NBBM catalysis results at 400 °C with MoS<sub>2</sub> under a hydrogen atmosphere.

<b>T = 400 °C, 0.10 g NBBM, 7.2 mg MoS<sub>2</sub>, 1000 psig H<sub>2</sub> (cold)</b>					
<b>Molar Yields of Products</b>					
<b>Product Code</b>	<b>Reaction Time (Minutes)</b>				
	<b>15</b>	<b>30</b>	<b>45</b>	<b>60</b>	<b>75</b>
1	0.798	0.686	0.505	0.489	0.441
2	0.006	0.008	0.005	0.006	0.006
3	0.000	0.001	0.001	0.003	0.003
4	0.002	0.008	0.012	0.020	0.023
5	0.000	0.001	0.002	0.003	0.004
6	0.000	0.002	0.004	0.007	0.009
7	0.008	0.032	0.048	0.051	0.056
8	0.053	0.163	0.231	0.266	0.285
9	0.062	0.220	0.310	0.348	0.362
10	0.004	0.005	0.006	0.011	0.015
11	0.006	0.024	0.036	0.038	0.039
12	0.001	0.002	0.003	0.004	0.005
13	0.001	0.002	0.002	0.004	0.003
14	0.000	0.006	0.006	0.011	0.010
15	0.000	0.000	0.000	0.000	0.000